Dissertation
submitted to the
Combined Faculty of Mathematics, Engineering and Natural Sciences
of Heidelberg University, Germany
for the degree of
Doctor of Natural Sciences

Put forward by
Ing. Alena Gromada
born in: Přerov, Czech Republic
Oral examination: 22.11.2021

Inclusive J$/\psi$ production
in Pb–Pb collisions at $\sqrt{s_{\mathrm{NN}}} = 5.02$ TeV
with ALICE

Referees: Prof. Dr. Silvia Masciocchi

Prof. Dr. Ulrich Uwer

Messung der inklusiven Produktion von J$/\psi$ Mesonen bei mittlerer Rapidität in Pb–Pb Kollisionen bei $\sqrt{s_{\mathrm{NN}}} = 5.02$ TeV mit ALICE

Das J$/\psi$ Meson ist ein Hadron bestehend aus einem Charm Quark und einem Charm Antiquark (c$\bar{\mathrm{c}}$). Die Produktion von J$/\psi$ Mesonen dient als wichtige Sonde für das Quark-Gluon Plasma, das in Schwerionenkollisionen erzeugt wird. Die Anwesenheit des stark wechselwirkenden Mediums, in dem der Farbeinschluss aufgehoben ist, resultiert in der Abschirmung des Farbladungspotential zwischen Charmquarks und -antiquarks, die als Paare in harten Streuprozessen gebildet werden. Bei ausreichend hohen Strahlenergien, wie z.B. am LHC, führt die große Anzahl produzierter Charmquarks zur (Re)Generierung von J$/\psi$ Mesonen während der QGP Phase und/oder an der Phasengrenze.

Diese Arbeit beschreibt die Messung von J$/\psi$ Mesonen in Kollisionen von Bleiatomkernen, die mit ALICE bei $\sqrt{s_{\mathrm{NN}}} = 5.02$ TeV aufgenommen wurden. Über den Zerfallkanal J$/\psi \rightarrow$ e$^+$e$^-$ wurde die J$/\psi$ Multiplizität bei zentraler Rapidität in Abhängigkeit von der Zentralität der Kollisionen und als Funktion des Transversalimpulses gemessen. In den zentralsten Kollisionen und solchen von mittlerer Zentralität wurde die Messung bis zu einem minimalen p_{T} von 0.15 GeV/c durchgeführt. Der nukleare Modifikationsfaktor R_{AA} von J$/\psi$ Mesonen nimmt leicht von Kollisionen mittlerer Zentralität zu den zentralsten Kollisionen ab. In Abhängigkeit von p_{T} zeigt die Messung von R_{AA} eine starke Unterdrückung der J$/\psi$ Ausbeute bei hohem p_{T} an. Mit abnehmendem p_{T} steigt R_{AA}. Diese Messung wird mit anderen experimentellen Resultaten und mit Modellrechnungen verglichen. Die hier präsentierten Ergebnisse unterstützen die Vorstellung, dass (Re)Generierung einen wichtigen Produktionsmechanismus für J$/\psi$ Mesonen am LHC darstellt, insbesondere bei niedrigem Transversalimpuls und bei zentraler Rapidität.

Inclusive J$/\psi$ production in Pb–Pb collisions at $\sqrt{s_{\mathrm{NN}}} = 5.02$ TeV with ALICE

The J$/\psi$ mesons is a bound state of a charm quark and its anti-quark. The production of J$/\psi$ mesons serves as an important probe of the quark-gluon plasma (QGP) formed in heavy-ion collisions. The presence of the deconfined strongly interacting medium results in the color screening of the potential between charm quarks and anti-quarks created during hard scattering processes. At sufficiently high collision energies such as the LHC energy, the large abundance of produced charm quarks leads to the (re)generation of J$/\psi$ mesons during the QGP evolution and/or at the phase boundary.

In this work, the J$/\psi$ production yield in Pb–Pb collisions at $\sqrt{s_{\mathrm{NN}}} = 5.02$ TeV recorded by ALICE is measured at midrapidity via the dielectron decay channel J$/\psi \rightarrow$ e$^+$e$^-$ as a function of centrality and as a function of transverse momentum down to $p_{\mathrm{T}} = 0.15$ GeV/c in the most central and semi-central collisions. The J$/\psi$ nuclear modification factor R_{AA} increases slightly from semi-central to the most central collisions. The p_{T}-differential J$/\psi$ R_{AA} shows a large suppression of the J$/\psi$ yield at high p_{T} and the J$/\psi$ R_{AA} increases with decreasing p_{T}. The measurement is compared to other experimental results and to model calculations. The presented results strongly support picture of (re)generation as an important J$/\psi$ production mechanism at the LHC especially significant at low p_{T} and at midrapidity.

Contents

Introduction

In this work, the measurement of the inclusive J/ψ meson production in Pb–Pb collisions at the center-of-mass energy $\sqrt{s_{NN}} = 5.02$ TeV collected by A Large Ion Collider Experiment (ALICE) will be presented. This chapter provides a basis for the discussion of this topic. Firstly, elementary particles and interactions between them will be briefly introduced in Section 1.1. Afterwards, the phase of strongly interacting, deconfined matter called the quark-gluon plasma (QGP) will be discussed in Section 1.2. The QGP is believed to exist within the first microseconds after the Big Bang [1] and nowadays is studied via ultra-relativistic heavy-ion collisions such as Pb–Pb collisions recorded by experiments at the Large Hadron Collider (LHC). At the end of this chapter, a few examples of experimental signatures of this remarkable state of matter will be discussed in Section 1.3. The J/ψ meson production, which serves as a probe of the QGP, will be discussed in the Chapter 2. The ALICE detector is described in the Chapter 3. Finally, individual steps in measurement of the inclusive J/ψ meson production and the results will be presented in Chapter 4 and Chapter 5.

1.1   Standard Model of particle physics

The Standard Model (SM) of particle physics is theory classifying elementary particles and describing three fundamental interactions: the electromagnetic, weak and strong interactions. The current form of the SM has been defined by a long series of theoretical predictions confirmed by experimental observations. Despite all its successful prediction, the SM is not a complete theory. It does not include the gravitational force. Possible new physics beyond the SM is in the center of vivid theoretical and experimental studies. For example, astrophysical observations point to the possible existence of dark matter that does not interact at all or only very weakly by the gravitational and weak interactions.

Elementary particle of the SM can be divided into two basic groups according to their spin: fermions with spin 1/2 and bosons with integer spin. They are all shown in Figure 1.1. The fermions of the first generation on the left of the figure are the basic building blocks of ordinary matter around us. Protons and neutrons consist of up and down quarks. Electrons surround atomic nuclei. Electron neutrinos are created in β^+ decays. The first generation of fermions is followed by two further known generations, which have identical properties as their lighter siblings from the first generation with exception of their mass and other differences following from it such as the magnetic moment. Higher generations decay to the lighter fermions. Bosons with spin equal to one act as mediators of interactions between fermions. Photons mediate the electromagnetic interaction, $W^{\pm}$ and Z bosons the weak interaction and gluons the strong interaction. Elementary fermions and bosons acquire their masses due to their coupling to the Higgs field.

The elementary fermions can be further classified into quarks and leptons. The lepton group includes electron, muon, tau and their respective neutrinos. All of them have corresponding antiparticles: e^+, μ^+, τ^+ and anti-neutrinos. Electrons, muons and taus interact electromagnetically and weakly. On the other hand, neutrinos do not possess electromagnetic charge. They interact only weakly, which makes their detection difficult. The masses of the neutrinos are constrained to very small values. However, they are non-zero for at least two neutrino generations, as is proven by observation of neutrino oscillations [4, 5].

1
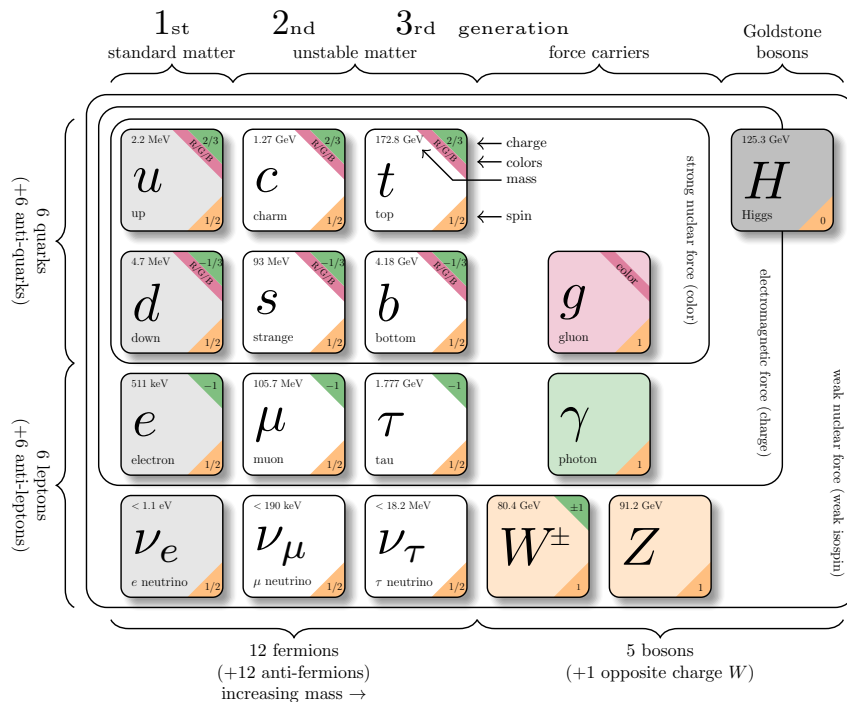
Figure 1.1: Elementary particles of the Standard Model. (The figure is taken from [2] and modified with values from [3].)

There are six quarks carrying six different flavors named after them: up (u), down (d), charm (c), strange (s), top (t), and bottom (b). The up and down quarks in the first generation with invariant masses equal to 2.2 MeV and 4.7 MeV are most abundant in the universe. Quarks obey the weak interaction, which is the only interaction that can change their flavor. Quarks from higher generations possess much larger masses, thus they decay weakly to the lighter quarks. The quarks from higher generations can be produced in high-energy collisions. Up, charm and top quarks carry electromagnetic charge equal to 2/3, and down, strange and bottom quarks equal to $-1/3$. Thus, they interact electromagnetically. Furthermore, they also carry the color charges of the strong interaction in contrast to leptons, while anti-quarks carry anti-colors. In the ordinary matter around us, quarks and anti-quarks are bound into colorless hadrons due to the strong force. Mesons contain a quark and an anti-quark, whereas baryons contain either three quarks or three anti-quarks.

The electromagnetic interaction described by the Quantum Electrodynamics (QED) is mediated via massless, electrically neutral photons. The reach of this interaction is infinite. On the other hand, the large masses of $W^{\pm}$ and Z bosons result in a limited reach of the weak interaction of approximately 10^{-2} fm. The symmetry associated to the weak interaction is the non-abelian SU(2) symmetry group. Uniquely among the fundamental SM interactions, the weak interaction can change quark flavors. The flavors are changed only by $W^{\pm}$ bosons and not by Z bosons. The theory unifying QED and the weak interaction is called the electroweak theory.

Quantum Chromodynamics (QCD) with SU(3) symmetry group is the theory of the strong interaction acting on quarks. Since the SU(3) symmetry group is non-commutative, the gluons that mediate the interaction also carry color charges. In total, there are eight independent color and anti-color combinations defining eight gluon color states. Since gluons carry the color charges, they interact with themselves and other gluons, unlike photons in the QED. This distinctive feature results in the existence of asymptotic freedom discussed in the following subsection.

1.1.1 Asymptotic freedom and quark confinement

A striking property of some of the non-abelian theories such as QCD, known as asymptotic freedom, was discovered in 1973 independently by Politzer [6] and Wilczek and Gross [7]. At large distance and low energy transfers, the coupling constant α_s reaches large values. On the other hand, the coupling strength decreases with decreasing distance and increasing energy transfer Q. Subsequently, quarks behave as free for $Q \to \infty$, since $\alpha_s \to 0$. This property has been experimentally verified by large variety of measurements of different processes. The summary of these is shown in Figure 1.2, which demonstrates clear confirmation of the predicted dependence of the strong coupling constant α_s on the energy transfer Q.

Asymptotic freedom can be explained by the behavior of the QCD vacuum. In QED, virtual electron and positron pairs are constantly produced and annihilate. The vacuum polarizes in the presence of an electromagnetic charge. This leads to screening of the charge at large distances. Quarks behave similarly in the QCD vacuum. However, virtual gluons carrying combinations of colors and anti-colors have a different effect, augment strength of the field [8]. This effect overcomes color screening caused by quarks. The effect of the vacuum ceases at low distances from the color charge.
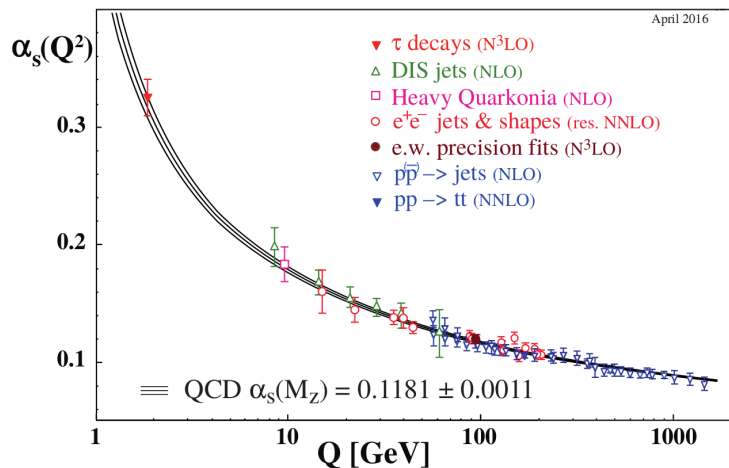
Figure 1.2: Measurements of the strong coupling constant α_s as a function of the energy scale Q. (Figure is taken from [9].)

The discovery of asymptotic freedom enabled development of perturbative QCD (pQCD) predictions for different processes with large energy transfers. However, pQCD cannot be used at low energy transfers, where the coupling constant α_s reaches values of the order of one. The perturbative series of the cross sections in powers of α_s does not converge in this region. Thus, the lattice QCD (lQCD) approach has been developed to treat the processes with low transferred energy. lQCD is based on discretization of the space-time that allows the numerical study of QCD. Quarks are placed on the sites of the lattice, with gluon fields connecting the sites.

Quarks have never been observed as free particles due to color confinement. This effect can be illustrated by the phenomenological Cornell potential between quark and anti-quark 2.1 discussed in more detail later. When quarks or anti-quarks move away from each other, the gluon field between them resembles a stretching string. At some point, it starts to be energetically favorable to create a quark-anti-quark pair that splits the string into two pieces. This process can continue also for the split strings as long as there is enough energy to create new quarks and their anti-quarks. Finally, quarks and anti-quarks build hadrons. This process is called hadronization. As a result, quarks with their color charges can never appear alone without other quarks or anti-quarks. Although numerical calculations point strongly to existence of the color confinement, there is currently no existing rigorous proof. Therefore, the phenomenon of confinement is not yet fully understood.

3

1.2 Heavy-ion collisions and quark-gluon plasma

At high temperature and/or baryon chemical potential, quarks in hadrons become deconfined due to the color screening and the strongly interacting matter enters another new phase called the quark-gluon plasma (QGP). Our universe is believed to have been filled with the QGP from about a few nanoseconds to a few microseconds after the Big Bang [1]. We are nowadays able to create and study this fascinating state of matter in laboratories with large colliders such as CERN with the LHC and BNL with RHIC. The QGP can be created in high-energy heavy-ion collisions and the products of such collisions can be studied. Heavy-ion collisions serve as a tool to explore the extreme conditions of strongly interacting matter surrounding us and a window to early stages of our universe. This section discuss basic knowledge of the phase diagram of strongly interacting matter in Subsection 1.2.1. Description of high energy heavy-ion collision evolution used to study the QGP and basic experimental concepts follows.

1.2.1 QCD phase diagram

The QCD matter has different phases, similar to how water can exist in the form of a solid, liquid, or gas depending on temperature and pressure. A schema showing a possible QCD phase diagram in temperature T and baryon chemical potential μ_B plane is shown in Figure 1.3. The baryon chemical potential is a measure of net baryon density. μ_B corresponds to the energy needed to add one baryon for the phase of atomic nuclei. The phase closest to the atomic nuclei is the hadron resonance gas. Asymptotic freedom manifests itself for larger temperature. When the temperature of the hadron resonance gas increases enough, quarks are liberated from hadrons and become relevant degrees of freedom. In other words, the QCD matter undergoes a phase transition into the QGP state. The lQCD calculations have shown that the phase transition at vanishing μ_B is of so-called crossover type [10, 11]. In other words, thermodynamic properties such as pressure and energy density change continuously unlike in the case of the first order phase transition. Recent lQCD predictions suggest that temperature of the phase transition for $\mu_B = 0$ MeV, called the critical temperature, is approximately $T_c = 156$ MeV [12]. It is expected that this serves as a good approximation for transition undergone by the QGP present shortly after the Big Bang [12]. The QCD matter in a heavy-ion collisions at the LHC is closest to the conditions present at that time from all currently running colliders.

However, lQCD calculations become more difficult for non-zero μ_B. Despite different techniques developed recently for real finite chemical potential and extensive experimental efforts, it is currently not clear whether crossover is present on the whole border of the QGP and hadron gas phases. The crossover phase transition could change to the first order phase transition at a so-called critical point. Nevertheless, some theoretical works such as [14] suggest the absence of the critical point. It is predicted that the QCD matter enters a color superconductivity phase at high baryon chemical potential, similar to the conditions present in the cores of neutron stars [15].

1.2.2 Evolution of heavy-ion collisions

The evolution of ultra-relativistic collisions consists of several stages that are discussed in this section. The illustration of the space-time evolution for heavy-ion collision with energy density sufficient for QGP formation is shown in Figure 1.4. The z-axis is longitudinal to the beam direction. A collision begins at $t = 0$ fm/c when nuclei start to traverse each other and the medium enters a pre-equilibrium state. Partons of both nuclei undergo soft and hard scatterings. The largest energy transfers reach values sufficient for creation of so-called hard probes, such as heavy quarks or high momentum partons hadronizing later into sprays of particles observed in detectors called jets. Afterwards, the QGP is formed and expected to reach local thermal equilibrium due to parton re-scatterings at proper time $\tau = \sqrt{t^2 - z^2} \leq 1$ fm/c [16]. The local thermal equilibrium allows the use of a macroscopic hydrodynamic description of the subsequent evolution. This significantly simplifies simulations of the collective dynamics, which can be controlled by several hydrodynamic transport coefficients.
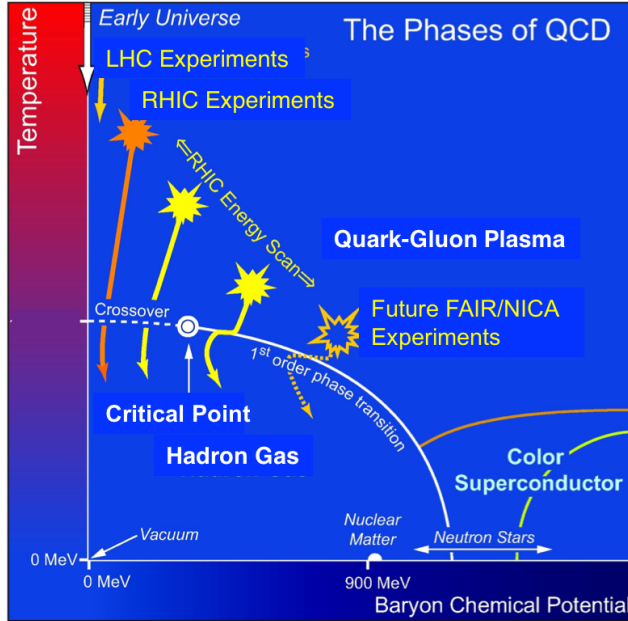
Figure 1.3: Possible QCD phase diagram in the temperature and baryon chemical potential plane. Regions probed by different hadron collider and fixed-target experiments are indicated. (Figure is taken from [13].)

However, a knowledge of the equation of state is needed. It can be taken from state-of-the-art lQCD predictions.

Since the QGP expands due to pressure gradients, it gradually cools down. After QGP life time $\tau \approx 10$ fm/c [18], the medium reaches the critical temperature T_c and undergoes hadronization. The hadronization—transition from deconfined medium to the hadron gas—could be either rapid or gradual through a mixed phase. The elastic cross section exceeds the inelastic cross section in a dilute medium, thus inelastic collisions cease first. This stage is called chemical freeze-out since the chemical composition of the hadron gas is fixed from then on. Finally, the expanding hadron gas reaches the kinetic freeze-out temperature when the hadron density is not large enough for elastic collisions. Hadrons fly away and can be detected.

1.2.3 Basic experimental concepts

Heavy-ion collisions and their products observed in detectors depend on geometry of collisions. An illustration of a heavy-ion collision is shown in Figure 1.5. The basic geometrical quantity characterizing a collision is the distance between the centers of the nuclei in the xy-plane perpendicular to the beam direction, referred to as the impact parameter b. The area of nuclear overlap is defined by this quantity. The number of participants N_{part}, nucleons interacting with nucleons of the other nucleus, is proportional to the overlapped area. Spectator nucleons continue in their previous direction almost unaffected by the collision. Head-on collisions with the impact parameter close to zero and large number of participants are named the central collisions. Collisions with the impact parameter fulfilling the condition $0 \ll b < R_{\mathrm{A}} + R_{\mathrm{B}}$, where R_{A} and R_{B} are the nuclear radii, are referred to as peripheral collisions. The properties of these collisions more closely resemble collisions of single nucleons than central heavy-ion collisions, due to the small typical number of participants. Neither the impact parameter b nor the number of participants N_{part} can be observed directly. Thus, heavy-ion collisions are often classified according to their centrality, which can be experimentally estimated using the charged-particle multiplicity, as is discussed in details in Section 3.6. The centrality of a heavy-ion collision is defined as the percentile of the total nuclear hadronic cross section of an A–A
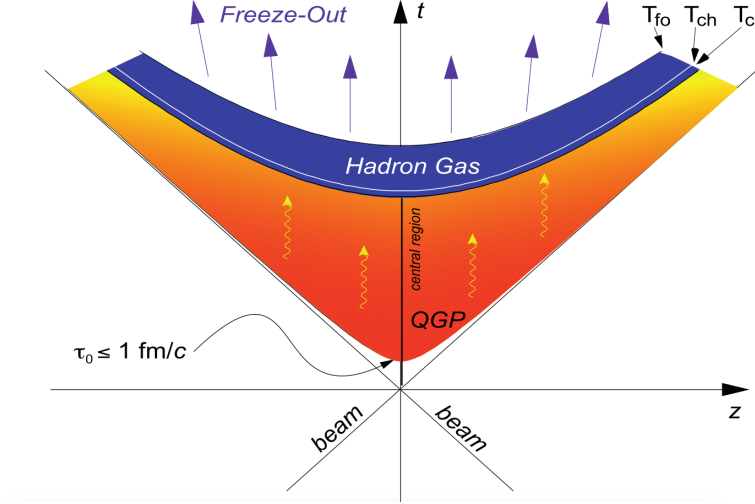
Figure 1.4: Illustration of the space-time evolution of a heavy-ion collision with sufficient energy density for the QGP formation. (Figure is taken from [17].)

collision σ_{AA} with the impact parameter b:

$$C = \frac{\int_0^b \mathrm{d}\sigma/\mathrm{d}b'\mathrm{d}b'}{\int_0^\infty \mathrm{d}\sigma/\mathrm{d}b'\mathrm{d}b'} = \frac{1}{\sigma_{\mathrm{AA}}} \int_0^b \frac{\mathrm{d}\sigma}{\mathrm{d}b'}\mathrm{d}b'. \tag{1.1}$$
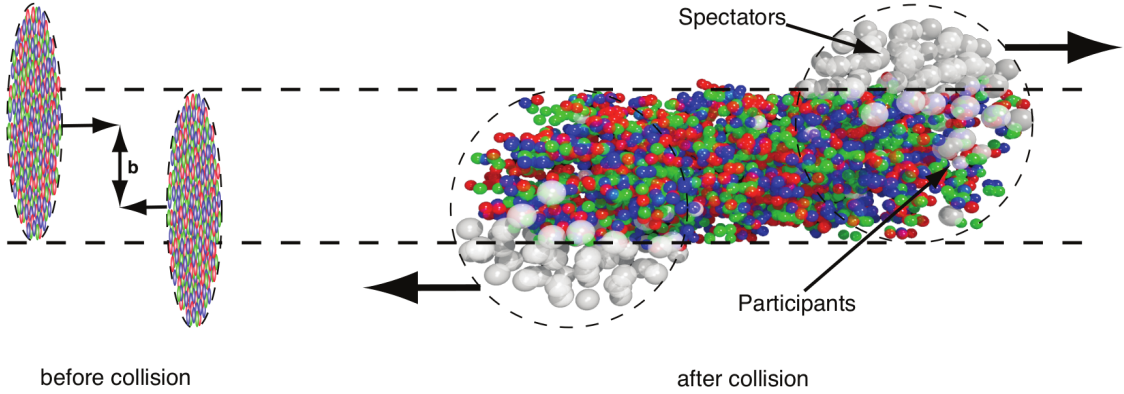
Figure 1.5: Left: Two heavy ions approaching each other before their collision with the impact parameter b. Right: An illustration of a heavy-ion collision. Participant nucleons collide with nucleons of the other nucleus, whereas spectators are almost unaffected. (Figure is taken from [19].)

Since the cross section for hard processes is proportional to the number of binary nucleon-nucleon collisions N_{coll}, it is often useful to express modification of a production with respect to the pp collisions by means of the nuclear modification factor R_{AB}:

$$R_{\mathrm{AB}}(y) = \frac{\mathrm{d}N_{\mathrm{AB}}^X/\mathrm{d}y}{\langle T_{\mathrm{AB}}\rangle\mathrm{d}\sigma_{\mathrm{pp}}^X/\mathrm{d}y} \quad \text{and} \quad R_{\mathrm{AB}}(p_{\mathrm{T}}, y) = \frac{\mathrm{d}^2 N_{\mathrm{AB}}^X/(\mathrm{d}y\mathrm{d}p_{\mathrm{T}})}{\langle T_{\mathrm{AB}}\rangle\mathrm{d}^2\sigma_{\mathrm{pp}}^X/(\mathrm{d}y\mathrm{d}p_{\mathrm{T}})}, \tag{1.2}$$

where N_{AB}^X and N_{pp}^X are the yields of probe X per rapidity window in A–B and pp collisions, σ_{pp}^X the total cross section per rapidity window in pp collisions, and $\langle T_{\mathrm{AB}}\rangle$ the average nuclear overlap

function. The nuclear overlap function T_{AB} represents the nucleon luminosity per A–B collision and is defined by

$$T_{\text{AB}} = N_{\text{coll}}/\sigma_{\text{NN}}^{inel}, \tag{1.3}$$

where $\sigma_{\text{NN}}^{inel}$ denotes nucleon-nucleon inelastic cross section. When R_{AB} is equal to unity, there is no modification of the probe X in A–B collisions compared to pp collisions. R_{AB} below unity means suppression of X in A–B collisions. The number of binary collisions N_{coll} and, therefore, also the nuclear overlap function T_{AB} are not observable. Thus, they are obtained using the Glauber Monte Carlo simulation [20] discussed in the Section 3.6. This simulation allows quantities that cannot be directly observed, such as b, N_{part} and N_{coll}, to be derived from the observable charged-particle multiplicity.

1.3   QGP signatures in heavy-ion collisions

The quark-gluon plasma cannot be observed directly. Thus, its properties are studied experimentally via various observables and probes. Probes can be divided into soft and hard probes. Production of the latter is related to large momentum transfers typical for the initial hard-parton scatterings. Conversely, the soft probes originate from processes with low momentum transfers. The yields and anisotropic flow of light-flavor hadrons are related to the soft processes and will be presented in this section. The hard probes include the energy loss of high-momentum particles, discussed in Section 1.3.3. Another example from this group are heavy quarks, which are created only during hard parton scatterings due to their large masses. The J/ψ meson—the bound state of a charm quark and its anti-quark—plays a special role among hadrons containing charm quarks, and is discussed thoroughly in Chapter 2.

1.3.1   Yields of light-flavor hadrons

Yields of different light-flavor hadrons are a basic observable studied by heavy-ion experiments. Measurement of the yields in combination with theoretical predictions provides valuable information about fundamental properties of the medium created in heavy-ion collisions. The medium can be described by thermodynamic properties under the assumption that the system behaves collectively, not as superposition of individual particles. To achieve this, the system has to include large numbers of particles on the order of at least thousands, which heavy-ion collisions at largest energies indeed satisfy. Furthermore, the system has to reach the local thermal equilibrium. This can be fulfilled when the interaction rate of particles is high enough and the lifetime of the medium is long enough to allow at least several interactions between its constituent particles [21]. Under these assumptions, the chemical freeze-out temperature T_{ch}, the baryon chemical potential μ_{B} and the volume of fireball at chemical freeze-out can be determined by fit of a statistical hadronization model to the observed light-flavor hadron yields.

The Statistical Hadronization Model (SHM) [22, 23] uses a grand canonical formalism for the description of the yields. The equation for particle density is obtained using the derivative of the grand canonical partition function:

$$n_i = \frac{N_i}{V} = -\frac{T}{V}\frac{\partial \ln Z_i}{\partial \mu_i} = \frac{g_i}{2\pi^2}\int_0^\infty \frac{p^2 \mathrm{d}p}{\exp[(E_i - \mu_i)/T] \pm 1}, \tag{1.4}$$

where i is the particle index, Z_i represents the grand canonical partition function, $g_i = 2J_i + 1$ represents the spin degeneracy factor, $E_i = \sqrt{p^2 + m_i^2}$ the total energy, V the system volume, the plus sign corresponds to fermions and the minus sign to bosons. The chemical potential $\mu_i = \mu_{\text{B}}B_i + \mu_{\text{I}_3}I_{3i} + \mu_{\text{S}}S_i + \mu_{\text{C}}C_i$ ensures conservation of the baryon, isospin, strangeness and charm quantum numbers. The fit of the model to the light-flavor hadron yields measured by ALICE in Pb–Pb collisions at center-of-mass energy per nucleon-nucleon pair $\sqrt{s_{\text{NN}}}$ equal to 2.76 TeV is shown in Figure 1.6. A contribution of resonance decays to the hadron yields has to be considered while fitting the data. The thermal yields from the model fit added with contribution from resonance decays are shown as full blue lines. Remarkably, the model fit is in a very good agreement with measured

hadron yields from non-strange and strange hadrons and nuclei over nine orders of abundance magnitude. The parameters constrained by the fit are $T_{ch} = 156 \pm 1.5$ MeV, $\mu_B = 0.7 \pm 3.8$ MeV and $V = 5280 \pm 410$ fm^3 [24]. The baryon chemical potential μ_B at high collision energies is consistent with zero due to balance between matter and anti-matter abundances. The chemical freeze-out temperature T_{ch} is in agreement with the critical temperature T_c obtained by the lQCD, as discussed in Subsection 1.2.1. This finding indicates that the chemical freeze-out is very close to the hadronization at low baryon chemical potential μ_B. The thermal fit has been has also been successfully applied to broad palette of results from the Super Proton Synchrotron (SPS) and the Relativistic Heavy Ion Collider (RHIC) [24]. This allowed to T_{ch} and μ_B to be obtained at a broad range of collision energies.
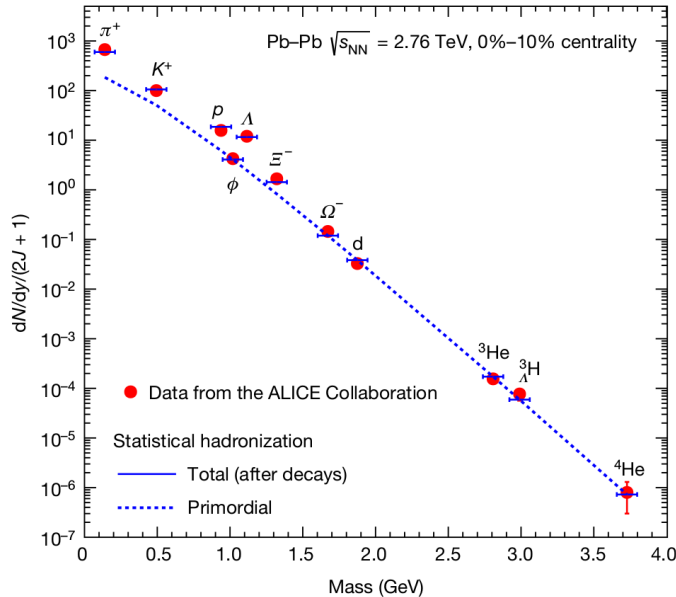
Figure 1.6: Yields of different hadron species measured by ALICE in the 10% most central Pb–Pb collisions at $\sqrt{s_{NN}} = 2.76$ TeV divided by the spin degeneracy factor. The yields are fitted by the Statistical Hadronization Model [23]. The result of the fit is shown as the dashed blue line. The total yields marked by the solid blue lines are obtained by adding contributions from the resonance decays. (Figure is taken from [24].)

An interesting question is whether also yields of hadrons containing heavy quarks can be described using similar concepts. Thus, the SHM is also applied to their production. However, heavy charm and bottom quarks, unlike lighter quarks, are produced almost exclusively during hard scatterings at the beginning of heavy-ion collisions. Their thermal production at current collider energies is strongly suppressed due to their large masses. Therefore, the statistical hadronization approach applied to describe the light-flavor hadron yields has to be modified. The SHM for hadrons containing charm quarks will be discussed later in Subsection 2.6.

1.3.2 Anisotropic flow

When two nuclei collide in a semi-central or peripheral collision, the participant zone has an anisotropic almond-like shape. This is illustrated in Figure 1.7. The beam direction and the vector of the impact parameter lie in the reaction plane, the symmetry plane of the almond-like participant zone. The initial spatial anisotropy of the participant zone develops into the hot and dense medium with anisotropic pressure gradients. Pressure gradients in the reaction plane are larger with respect to gradients pointing out of plane. Therefore, the medium close to the reaction plane is pushed away more powerfully and particles present in this region inherit on average larger momenta than

particles heading in the out-of-plane direction. Comparisons of observed the azimuthal anisotropy to hydrodynamic model predictions provide the opportunity to study properties of the QGP such as the shear viscosity to entropy density ratio η/s and the bulk viscosity to entropy density ratio ζ/s.

The medium can be characterized by studying Fourier coefficients v_n of the azimuthal yield distribution:

$$E\frac{\mathrm{d}^3 N}{\mathrm{d}p^3} = \frac{1}{2\pi}\frac{\mathrm{d}^2 N}{p_\mathrm{T}\mathrm{d}p_\mathrm{T}\mathrm{d}y}(1 + 2\sum_{n=1}^{\infty} v_n \cos[n(\varphi - \Psi_n)]), \qquad (1.5)$$

where E is the energy, p the momentum, p_T the transverse momentum, y rapidity, φ the azimuthal angle and Ψ_n the n-th harmonic symmetry plane. The angle of the reaction plane cannot be directly observed, therefore, it is experimentally estimated using the measured azimuthal anisotropy itself for each harmonic separately. The estimation of the reaction plane is often referred to as the participant plane. The Fourier coefficients can then determined using the relation

$$v_n(p_\mathrm{T}, y) = \langle\cos[n(\varphi - \Psi_n)]\rangle. \qquad (1.6)$$
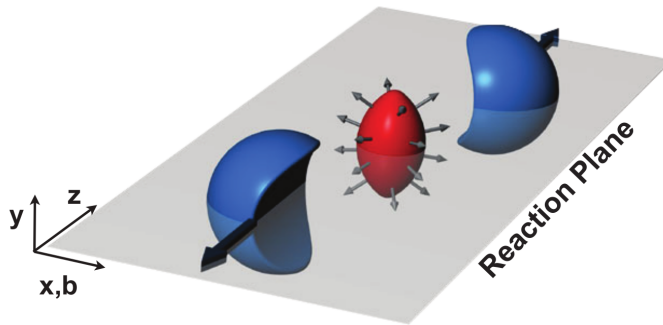
Figure 1.7: An illustration of a semi-central heavy-ion collision. The almond-shaped participant zone is shown in red color, while spectator zones in blue color. Pressure gradients are represented by arrows. The reaction plane corresponds to the xz-plane. (Figure is taken from [25].)

The analysis of the Fourier coefficients in combination with hydrodynamic predictions constrain transport coefficients of the medium and event-by-event fluctuations in the initial collision geometry. The second order Fourier coefficient v_2 is named elliptic flow. It reflects the azimuthal anisotropy of particle distribution caused by the almond-like initial geometry. The elliptic flow v_2 represents the largest contribution to the particle distribution anisotropy in non-central collisions. The third order coefficient v_3, called triangular flow, is primarily driven by initial-state fluctuations [26].

The Figure 1.8 shows the elliptic flow v_2 at midrapidity measured by ALICE in Pb–Pb collisions at 5.02 TeV [27]. Different panels correspond to different identified hadron species containing light quarks. The azimuthal distributions of all the hadron species exhibit sizable v_2 showing that the medium behaves collectively. The elliptic flow v_2 at low transverse momentum p_T reflects hydrodynamic nature of the medium. On the other hand, v_2 at $p_\mathrm{T} \gtrsim 8$ GeV/c is driven by the parton energy loss [28, 29] in the anisotropically distributed medium. The v_2 coefficient increases with centrality up to approximately 50% due to larger eccentricity of the overlap zone. The measured v_2 in more peripheral events with centrality above 50% is smaller than at lower centrality intervals (with exception of ϕ meson) suggesting shorter medium lifetime [30].

1.3.3 Parton energy loss

Hard scatterings takes place in heavy-ion collisions as well as in pp collisions. When the QGP is formed in heavy-ion collisions, high energy partons may traverse it and lose energy due to the strong interaction with the deconfined medium. A modification of the production caused by the parton energy loss in the QGP can be studied via the reconstruction of jets, collimated showers of
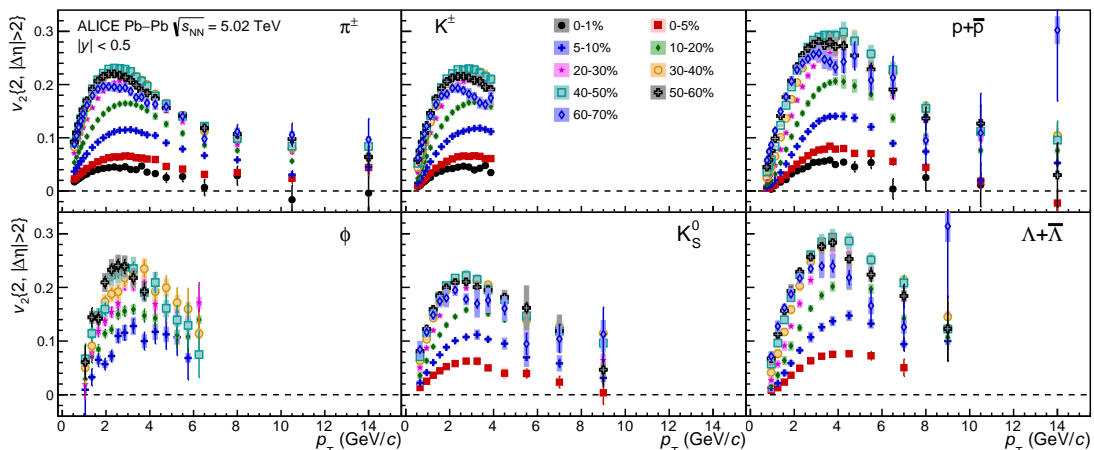
Figure 1.8: Elliptic flow coefficient v_2 as a function of transverse momentum p_T in different centrality classes for $\pi^{\pm}$, $K^{\pm}$, $p + \bar{p}$, $\Lambda + \bar{\Lambda}$, K_s^0 and the ϕ meson. (Figure is taken from [27].)

particles originating from the initial parton, or via measurement of high-momentum particles. Since production of the hard probes scales with the number of binary nucleon-nucleon collisions N_{coll}, the nuclear modification factor from Equation 1.2 represents a straightforward way to study their modification caused by the presence of the hot, deconfined medium.

Light-flavor hadrons with transverse momentum p_T above approximately 5 GeV/c are expected at the LHC to originate predominantly from the fragmentation of high momentum gluons or light quarks created during hard scatterings. The gluon fragmentation dominates up to approximately 20 GeV/c, and the light-quark fragmentation at larger [31]. The nuclear modification factor R_{PbPb} of charged-particle production, which is dominated by light-flavor hadrons, is shown in the left panel of Figure 1.9. The R_{PbPb} measured by ALICE [32] and CMS [33] in Pb–Pb collisions at 2.76 TeV shows strong suppression of the charged-particle production in the full measured range of transverse momentum p_T interval, including the high p_T region relevant for probing of the parton energy loss. At low momentum, light quarks are dominantly produced by the soft processes and the shape of R_{PbPb} as a function of p_T is driven by collective effects. The R_{PbPb} is compared to the nuclear modification factor R_{pPb} in p–Pb collisions at 5.02 TeV [34]. It is consistent with unity, which strongly indicates that the suppression of charged-particle production in Pb–Pb is not caused by cold nuclear matter effects or the initial-state effects present also in collisions without the formation of a QGP. Another measurement supporting that the suppression of charged-particle production at high p_T is caused mostly by the strong interaction with the deconfined medium is the measurement of the nuclear modification factor R_{PbPb} of direct photons [35], W [36] and Z bosons [37]. Photons as well as the leptonic decay products of W and Z bosons, which decay before the QGP is formed, do not carry a color charge.

An interesting probe of the parton energy loss induced by the strong interaction is the production of D mesons, since they contain one charm quark. Thus, charm quarks experience the full evolution of the medium since the initial hard parton scatterings. D mesons with high transverse momenta p_T originate mostly from the fragmentation of charm quarks. Therefore, the R_{PbPb} of D mesons at high p_T represents a clear probe of the charm quark energy loss. Quarks are expected to lose their energy mostly via collisional energy loss at lower momenta, whereas gluon radiation is expected to dominate at large momenta. Energy loss via gluon radiation is affected by so-called dead-cone effect, which has recently been directly observed by ALICE [40]. The radiation of gluons is suppressed in a cone of angular size proportional to m/E around the momentum direction of incident quark. Thus, it is expected that heavy-flavor quarks lose less energy due to their large mass than the light quarks. However, the effect should vanish at large momenta due to dependence of the cone size on $1/E$. The R_{PbPb} of D mesons [39] and charged particles [38] in most central Pb–Pb collisions at 5.02 TeV is
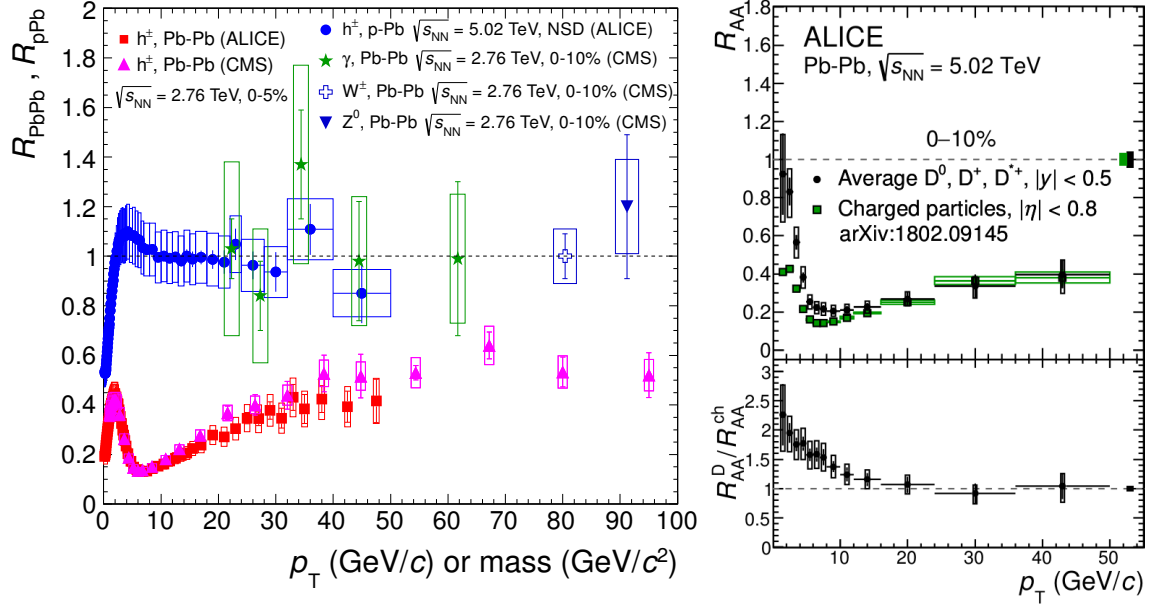
Figure 1.9: Left: Nuclear modification factors R_{pPb} in p–Pb collisions and R_{PbPb} in the most central Pb–Pb collisions as a function of transverse momentum p_{T}. The R_{PbPb} of charged particles [32, 33], direct photons [35], Z^0 bosons [37] and $W^{\pm}$ bosons [36] is measured in Pb–Pb collisions at $\sqrt{s_{\mathrm{NN}}} = 2.76$ TeV. The R_{pPb} of charged particles ($h^{\pm}$) in p–Pb collisions at 5.02 TeV [34] is compared to the R_{PbPb}. (Figure is taken from [34].) Right: Nuclear modification factors R_{PbPb} of prompt D^0, D^+ and D^{*+} mesons and R_{PbPb} of charged particles [38] as a function of p_{T} measured in Pb–Pb collisions at $\sqrt{s_{\mathrm{NN}}} = 5.02$ TeV. R_{PbPb} is shown in three centrality classes: 0–10% (left), 30–50% (middle) and 60–80% (right). (Figure is taken from [39].)

compared in the right top panel of Figure 1.9, their ratio is shown in the lower panel. The R_{PbPb} of D mesons and charged particles are consistent within 1σ for $p_{\mathrm{T}} > 12$ GeV/c. The deviation of the ratio from unity increases with decreasing p_{T}. At low p_{T}, the D-meson production can provide insight in different physics than at high p_{T}. Low momentum charm quarks are expected to inherit some of the collective motion of the medium. Measurements of D-meson production can therefore be used to constrain transport properties of the medium [41].

Charmonium J/ψ

This chapter is dedicated to the J/ψ meson. An introduction to charmonia is discussed in the first Section 2.1. The rest of this chapter is focused on the J/ψ meson in hadronic collisions. This topic is in general introduced in the Section 2.2. A discussion of J/ψ production in pp collisions follows in Section 2.3. J/ψ in pA collisions is presented in Section 2.4. Finally, special attention is dedicated to J/ψ production in A–A collisions in the sections 2.5, 2.6 and 2.7 as this work is based on the measurement of J/ψ in Pb–Pb collisions. The production in hadronic collisions is discussed both from experimental and theoretical points of view.

2.1   Charmonia

Quarkonia are bound states of a heavy quark and its anti-quark. Therefore, they are flavorless and without charge. As the names suggest, charmonia contain one charm quark and its anti-quark, whereas bottomonia one bottom quark and its anti-quark. The J/ψ meson belongs to the charmonium family. Vivid experimental studies of this particle date back to its discovery announced in November 1974. The observation of a narrow resonance with invariant mass close to 3.1 GeV/c^2 was announced simultaneously by Ting's group using pBe collisions at the Alternating Gradient Synchrotron at Brookhaven National Laboratory [42] and Richter's group in e$^+$e$^-$ annihilation at the Stanford Linear Accelerator [43]. This resonance was later interpreted as a bound state of a quark with a new fourth flavor and its anti-quark [44, 45]. Thus, the first observation of the J/ψ meson made history as the charm quark discovery, which was the so-called November Revolution. The discovery inspired the community of particle physicist and was followed by searches for other missing elementary particles.

The full width of the J/ψ resonance is today known to be $\Gamma = 92.9 \pm 2.8$ keV [9]. This translates to a long lifetime $\tau_{\mathrm{J}/\psi} \sim 10^{-20}$ s in comparison to lifetimes typical for the strong interaction $\tau \sim 10^{-23}$ s. This is caused by the fact that strong decays are either forbidden or suppressed. The J/ψ meson cannot decay to an open-charm meson pair since twice the mass of the lightest D meson is larger than the J/ψ mass. Other strong decays to hadrons are suppressed due to the OZI rule [47, 48, 49] since they have to proceed via annihilation into three gluons due to color and parity conservation. These three gluons must carry enough energy to fragment into hadrons and the strong coupling constant decreases with transferred momentum as discussed in Section 1.1. In consequence, the strong decays via three gluons are suppressed by three orders of α_s. This allows the electromagnetic decays via a virtual photon to compete with the strong decays. The J/ψ electromagnetic decays proceed via a virtual photon since it has the same total angular momentum, parity and C-parity quantum numbers as a photon.

The virtual photon can decay into hadrons or dilepton pairs resulting into J/ψ decay channels J/$\psi \to$ e$^+$e$^-$ and $\to \mu^+\mu^-$ with the branching ratios 5.971 ± 0.032 % and $5.96 + \pm 0.033$ % [9]. These decay channels provide the opportunity to reconstruct J/ψ via leptons that suffer less from challenging background conditions. An example of the dimuon continuum in pp collisions as a function of mass is shown in Figure 2.1. Reconstructed resonances and Z-boson decay are indicated in the figure. The J/ψ-meson peak is followed by its first excited state ψ' with the invariant mass around 3.69 GeV/c^2 [9]. Bottomonia $\Upsilon(1S)$, $\Upsilon(2S)$ and $\Upsilon(3S)$ correspond to one singe peak and
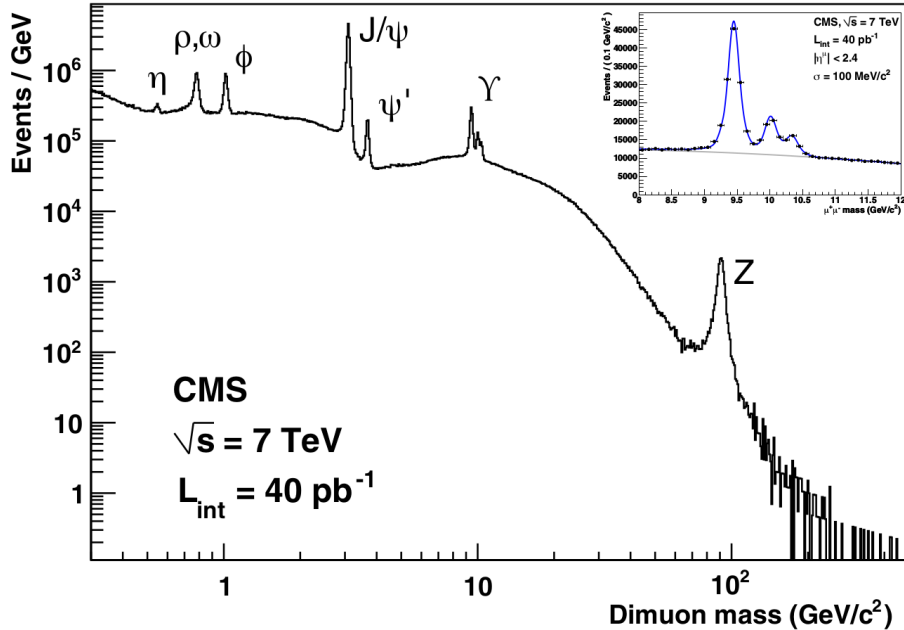
Figure 2.1: Di-muon invariant mass spectrum in pp collisions at $\sqrt{s} = 7$ TeV collected by the CMS detector in 2018. Reconstructed resonances and Z-boson decay is indicated. (Figure is taken from [46].)

two merged peaks around 10 GeV/c^2.

The charm and bottom quark have large mass, thus their velocities in the quarkonium rest frame can be considered as non-relativistic. Therefore, quarkonium invariant masses can be estimated in non-relativistic potential theory [50]. The binding of a charm quark and its anti-quark can be expressed by the Cornell potential as at first suggested in [51]:

$$V(r) = -\frac{4}{3}\frac{\alpha_s}{r} + k \cdot r, \tag{2.1}$$

where r is the radial distance between two quarks, α_s the running coupling constant and k the string tension. The string part of the potential $k \cdot r$ represents the quark confinement. It manifests itself at larger radii, whereas the Coulomb-like part dominates at small radii. Theory calculations based on the Cornell potential reproduce well the measured charmonium invariant masses below the open-charm decay thresholds [52]. The experimentally established charmonium states are shown in Figure 2.2. The states below all thresholds for open-charm production are considered to be stable with respect to the strong interaction. The hadronic transitions of charmonium states are represented by arrows, whereas the single photon transitions are listed below the figure.

2.2 J/ψ production in hadronic collisions

The J/ψ meson has been an important tool to study hadronic collisions. The charm quarks are created almost exclusively during hard partonic scattering processes due to the large charm mass. On the other hand, an evolution of a c$\bar{c}$ pair into a bound state is non-perturbative. Thus, charmonium production reveals the nature of QCD at different scales. Proton-proton (pp) collisions are widely used to study this. In heavy-ion (A–A) collisions, charm quarks are created as well as in pp collisions in initial hard scatterings due to the large charm quark mass and are present in the medium during its evolution. Thus, charmonium production carries information about properties of the QGP and the phase boundary. Proton-nucleus (pA) collisions serve for the investigation of cold nuclear matter

Figure 2.2: The level scheme of experimentally established charmonium states. Only observed hadronic transitions are shown. The single photon transitions $\psi(\text{nS}) \rightarrow \gamma\eta_c(\text{mS})$, $\psi(\text{nS}) \rightarrow \gamma\chi_{cJ}(\text{mP})$, $\chi_{cJ}(1\text{P}) \rightarrow \gamma\text{J}/\psi$ are omitted for clarity. (Figure is taken from [9].)

and initial state effects that have to be disentangled from effects caused by the presence of the hot deconfined medium.

pp, pA and A–A collision systems are discussed in more details later in this chapter. However, it is worth noting already here that inclusive J/ψ production in hadronic systems has several components before starting the journey through theoretical predictions and experimental results. The sum of J/ψ production is referred to as inclusive J/ψ production here. The inclusive J/ψ production can be sub-divided into three categories:

- Direct production: direct production originates from c$\bar{\text{c}}$ pairs produced during hard scatterings directly evolving into J/ψ mesons.

- Production from feed-down from charmonium states: c$\bar{\text{c}}$ pairs can evolve into heavier charmonium states χ_c and $\psi(2\text{S})$ that undergo transitions into J/ψ mesons. χ_c states decay into J/ψ and a single photon. Their contribution to the J/ψ production was studied at TeV energies by the LHCb Collaboration in pp collisions [53] and the CDF Collaboration at Tevatron in p$\bar{\text{p}}$ collisions [54].The fraction of J/ψ from χ_c at midrapidity measured by CDF and at forward rapidity examined by LHCb is approximately between 10 and 35% for $2 < p_T < 15$ GeV/c. The fraction of J/ψ originating from $\psi(2\text{S})$ decays can be estimated from ratios of $\psi(2\text{S})$ and J/ψ cross sections measured by the ALICE Collaboration in pp collisions [55] and the branching ratio of hadronic $\psi(2\text{S})$ transition to J/ψ equal to $(61.4 \pm 0.6)\%$ [9]. The estimate of the fraction is around 5% for momenta close to zero and 25% for p_T around 12 GeV/c. The sum of direct production and feed-down from decays of higher charmonium states is referred to as prompt production.

- Non-prompt J/ψ production: A further contribution to the J/ψ production comes from decays of hadrons containing b quarks. Since these decays proceed via the weak interaction, the

14

long lifetime of b hadrons allows to experimentally access the non-prompt fraction via the reconstruction of displaced vertices of b-hadron decays. The non-prompt fraction of the J/ψ production as a function of J/ψ p_T measured by different experiments at midrapidity and TeV center-of-mass energies is depicted in Figure 2.3. The non-prompt fraction is approximately 10% up to $p_T \approx 3$ GeV/c. It increases with rising momentum up to 0.7 around $p_T \approx 100$ GeV/c. The measurements in different collision systems from pp to Pb–Pb manifest the same trend as a function of p_T. Moreover, values of all shown measurements are very similar.
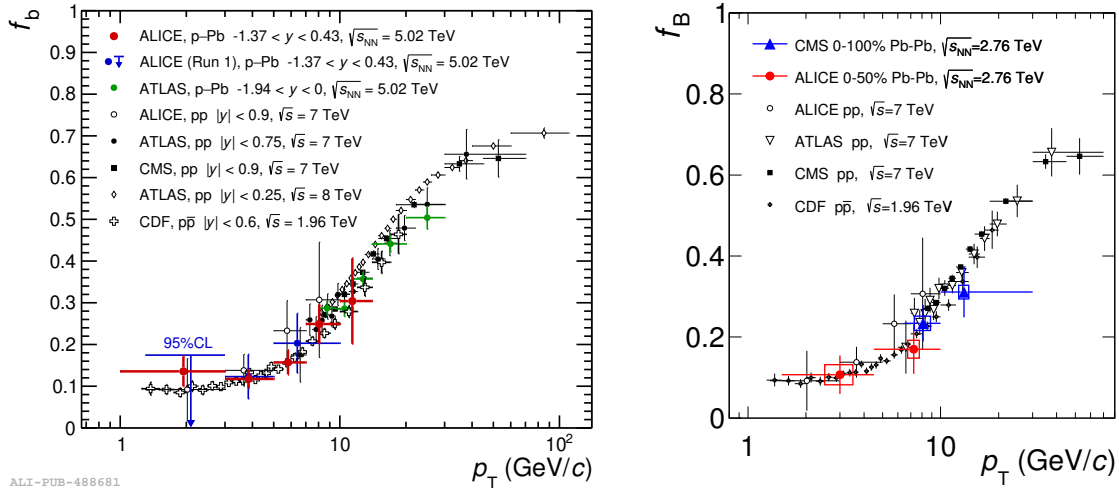
Figure 2.3: Fraction of J/ψ from b-hadron decays as function of J/ψ p_T in pp, $p\bar{p}$, p$\bar{p}$, and p–Pb collisions at TeV energies [56] (left) and in pp and Pb–Pb collisions [57] (right).

This work is based on the measurement of inclusive J/ψ production in Pb–Pb collisions. Inclusive J/ψ production consists of prompt and non-prompt fractions as discussed above that probe very different physics. Non-prompt J/ψ production reflects energy loss of b quarks propagating through the medium. The motivation for prompt J/ψ measurements is described in the sections 2.5, 2.6 and 2.7. This thesis presents a measurement of J/ψ at low p_T, where the fraction of J/ψ from b-hadron decays is small. Therefore, the motivation for the presented measurement is identical to the motivation of prompt J/ψ measurement. Considering experimental and theory uncertainties and the non-prompt J/ψ fraction value in the probed p_T interval, conclusions from comparison of the inclusive J/ψ measurement to theory predictions are not affected.

2.3 J/ψ production in pp collisions

According to the factorization theorem, charmonium production in pp collisions can be expressed as a convolution of three components: parton distribution functions (PDF), hard scattering cross-section into a $c\bar{c}$ pair and hadronization of the $c\bar{c}$ pair into a charmonium state. The parton distribution function characterizes the probability of finding a parton within a proton carrying a fraction x of the proton momentum. The parton distribution functions for quarks and gluons as a function of x measured at HERA are shown in the left panel of Figure 2.4. As can be seen, valence quark PDFs dominate at Bjorken x close to unity, whereas gluon and sea quark PDFs at low x. Regions of x and momentum transfer Q^2 studied with different collider and fixed-target experiments can be found in the right panel of Figure 2.4. The $x_{1,2}$ of incoming partons corresponding to the different probes shown in blue letters can be estimated from the formula $x_{1,2} = M/\sqrt{s} \cdot e^{\pm y}$ [9], where M is the mass of a state and $\sqrt{s}$ the center-of-mass energy. Bjorken x values relevant for J/ψ at the LHC are 10^{-2}–10^{-5}. In this region, the gluon PDFs have larger values than the quark PDFs. Therefore, $c\bar{c}$ production is dominated by gluon fusion processes. The production of heavy $c\bar{c}$ pairs requires

large Q^2, thus it can be calculated using perturbative QCD. On the other hand, the hadronization of $c\bar{c}$ into J/ψ has to be treated non-perturbatively. Differences between models of J/ψ production essentially are in the latter. An overview of charmonium production mechanisms can be found in [58]. In the following paragraphs, three models for charmonium production will be discussed: the Color Evaporation Model (CEM), the Color Singlet Model (CSM), and the Color Octet Model (COM). The latter two are implemented in the Non-Relativistic QCD (NRQCD) approach.
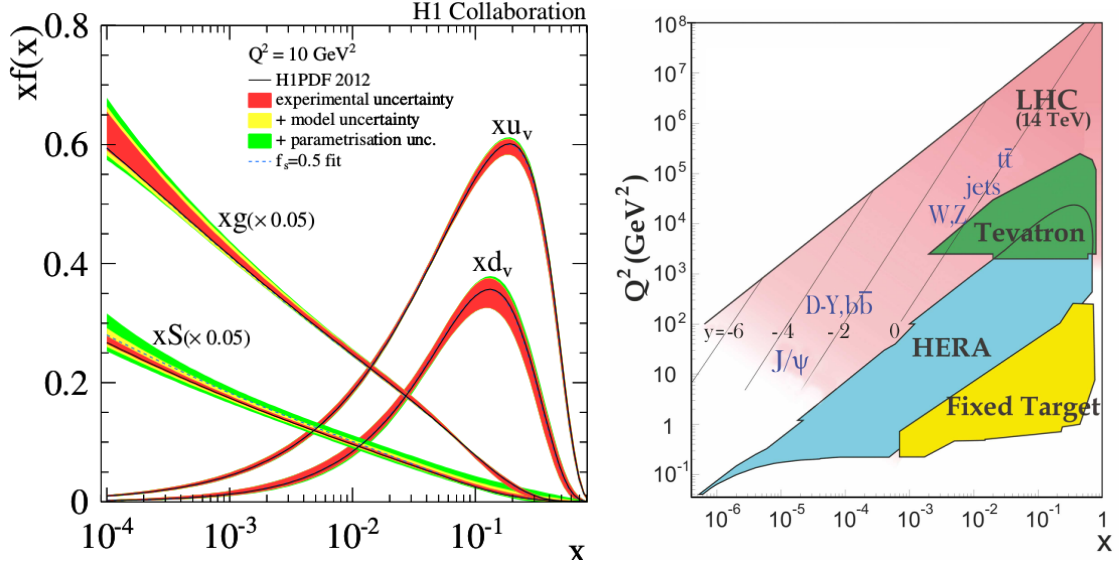
Figure 2.4: Left: Parton distribution functions for $Q^2 = 10$ GeV^2 relevant for J/ψ-meson production at the LHC. (Figure is taken from [59].) Right: Regions of x and Q^2 studied by different collider and fixed-target experiments. (Figure is taken from [60].)

2.3.1 Charmonium production mechanisms

The Color Evaporation Model (CEM) [61, 62] assumes that every $c\bar{c}$ pair can evolve into a given charmonium state in the case that the invariant mass of the pair is between the mass of two charm quarks and the lightest open-charm hadron pair. Quantum numbers of the $c\bar{c}$ pair are adjusted by soft gluon emission and exchange before the pair evolves into the final state. The probability of $c\bar{c}$ hadronizing into a specific charmonium state is a phenomenological constant independent of collision energy. The original CEM model also assumed that the momentum of the final state is very close to the momentum of the produced $c\bar{c}$ pair. This leads to the fact that ratios of p_T-differential cross sections of different charmonium states are independent of p_T within this approach in contradiction to experimental findings [55, 53]. This issue is addressed in the Improved CEM Model (ICEM) [63] that considers a momentum shift between the produced $c\bar{c}$ pair and the quarkonium caused by soft gluon emission and exchange. However, models based on color evaporation cannot predict charmonium polarization.

The Color Singlet Model (CSM) [64] builds its predictions on very different assumptions in comparison to the CEM. Only the $c\bar{c}$ pairs with the same quantum numbers such as angular momentum or spin as a to-be produced charmonium state and relative velocity v equal to zero can evolve into that state. Gluon emission is suppressed in the CSM. Thus, only $c\bar{c}$ in color-singlet states are considered in this model.

The Color Octet Model (COM) is implemented in the framework of Non-Relativistic QCD (NRQCD) [65]—an effective QCD theory approach using expansion not only in powers of α_s but also in powers of the heavy-quark velocity in a $c\bar{c}$ pair. As the name of the COM suggests, the model considers an evolution of color-octet states into a charmonium. The probability of an evolution of

a color-octet state into a given charmonium state is expressed via long-distance matrix elements (LDME). The first order of this model corresponds to the color-singlet contribution. The LDMEs for higher states have to be obtained by fits to measured cross sections. Therefore, predictions of the NRQCD model depend on the choice of measurements that are used to calculate the LDMEs.

2.3.2 Measurements of J/ψ production in pp collisions

A brief overview of experimental results with focus on recent ALICE measurements is given in this subsection. The ALICE Collaboration measures uniquely at the LHC J/ψ production at midrapidity down to $p_T = 0$ GeV/c. The p_T-differential inclusive J/ψ cross section $\mathrm{d}^2\sigma/\mathrm{d}p_T\mathrm{d}y$ at midrapidity in pp collisions at a center-of-mass energy $\sqrt{s} = 5.02$ GeV/c is shown in the left panel of Figure 2.5. The ALICE measurement [66] is compared with ATLAS [67] and CMS [68] measurements at midrapidity available for $p_T > 8$ GeV/c and $p_T > 6.5$ GeV/c, respectively. The cross sections are in a good agreement where the measurements of different experiments overlap. The ALICE measurement is used in this work as pp reference for the inclusive J/ψ production in Pb–Pb.
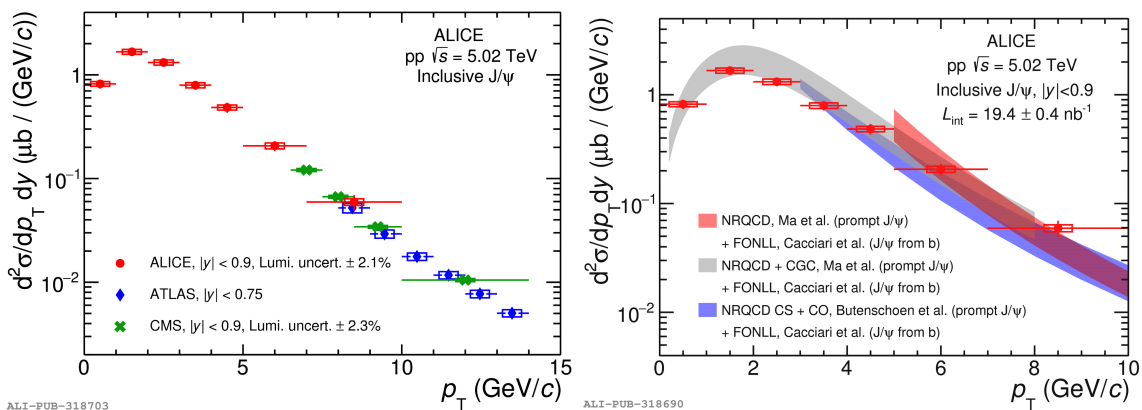
Figure 2.5: Left: p_T-differential inclusive J/ψ cross section in pp collisions at 5.02 TeV measured by ALICE [66] compared with ATLAS [67] and CMS [68] measurements at midrapidity. Right: p_T-differential inclusive J/ψ cross section [66] compared with NLO NRQCD [69, 70] and LO NRQCD+CGC [71] prompt J/ψ calculations summed with FONLL calculations for non-prompt J/ψ contribution [72].

The p_T-differential inclusive J/ψ cross section discussed above is compared to model predictions in the right panel of Figure 2.5. The measurement is superimposed with predictions for the prompt component summed with the FONLL prediction [72] for the non-prompt J/ψ component. There are two NLO NRQCD calculations considered: one by Ma et al. [69] and a second one by Butenschön et al. [70]. The latter does not consider the contribution of feed-down from heavier charmonium states, contrary to the former. The calculations of Ma et al. for the Leading Order (LO) NRQCD are performed with and without using the Color Glass Condensate (CGC) description of the gluon distributions in the proton [73]. A soft-gluon resummation in this model allows to extend the model calculation down to $p_T = 0$ GeV/c. All model predictions mentioned are consistent within error bars with the measurement.

The prediction of NRQCD using the CGC description summed with the non-prompt fraction is also in a good agreement with the J/ψ cross section as a function of rapidity as shown in the left panel of Figure 2.6 and as a function of collision energy from RHIC to LHC energies as shown in the right panel of the same figure. NRQCD predictions are successful also when comparing to many other measurements of charmonium cross sections. One example is a recent ALICE measurement of inclusive J/ψ and $\psi(2S)$ p_T-differential cross sections and their ratios at collision energies 5.02 TeV, 2.76 TeV and 13 TeV [74]. However, measurements of J/ψ polarization still challenge model predictions including different versions of the NRQCD models. An example is a recent measurement of the J/ψ polarization at forward rapidity by ALICE [75].

17
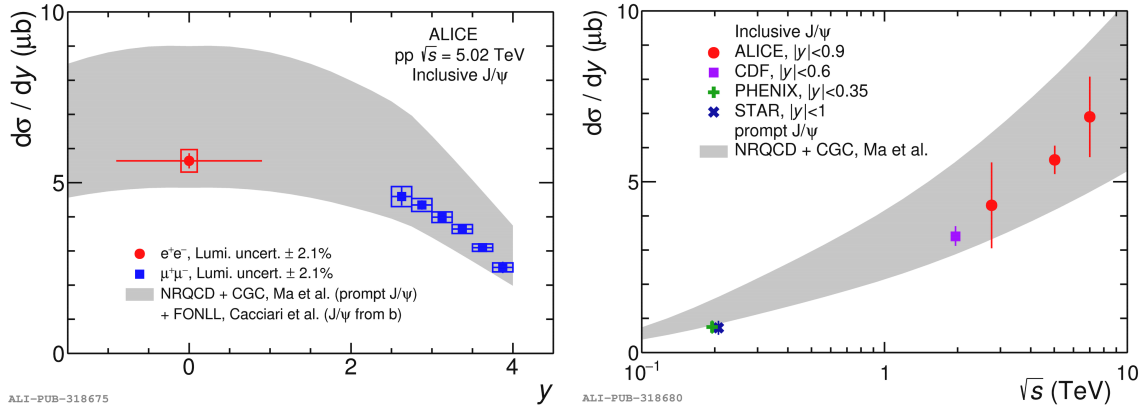
Figure 2.6: Left: Inclusive J/ψ cross section in pp collisions at 5.02 TeV as a function of rapidity measured by ALICE [55, 66]. Right: Inclusive J/ψ cross sections measured by ALICE [66, 76, 77], CDF [78], PHENIX [79] and prompt J/ψ cross section measured by STAR [80] at midrapidity as a function of collision energy. The measurements are compared to the LO NRQCD+CGC [71] prompt J/ψ calculations summed with FONLL predictions [72] for non-prompt J/ψ contribution. The figures are taken from [66].

2.4   J/ψ production in p–A collisions

p–A collisions are widely used to probe effects due to the presence of nuclear matter in the collision. QGP formation is not expected in minimum-bias p–A collisions. Therefore, measurements in p–A collisions provide key information for distinguishing effects of a hot, dense deconfined medium and effects originating from the presence of cold nuclear matter. In this section, we discuss gluon shadowing, which belongs to the initial state effects that are effective already before nuclei collide. Afterwards, cold nuclear matter effects (CNM) such as coherent energy loss, p_T-broadening and nuclear absorption are presented.

2.4.1   Gluon shadowing

PDFs $f_i(x, Q^2)$ in a nucleus are modified with respect to free nucleons due to presence of nuclear matter surrounding them. x is the fraction of momentum of a nucleon carried by a parton of a type i at the energy scale Q^2. The PDFs of partons in a free nucleon are discussed in Section 2.3. The modification depends on the x that is carried by a parton and Q^2.

The modification of nuclear PDFs (nPDFs) $f_i^A(x, Q^2)$ with respect to nuclen PDFs can be quantified by the nuclear modification function

$$R_i^A(x, Q^2) = \frac{f_i^A(x, Q^2)}{f_i(x, Q^2)}. \tag{2.2}$$

$R_i^A(x, Q^2) = 1$ in the case of no modification.

The nuclear modification function $R_i^A(x, Q^2)$ can be obtained by a global fit to sets of experimental results. An example of the EPPS16 fit function [81] is shown in the left panel of Figure 2.7. The lead nuclear modification function for gluons at the energy scale $Q^2 = 10$ GeV^2 relevant for J/ψ production at the LHC can be seen in the right panel of the same figure.

For $x \lesssim 10^{-2}$, R_i^A is smaller than unity. This modification is called shadowing. One possible explanation for this effect is provided by the theory of the Color-glass condensate (CGC) [82]. A very high density of gluons with low x in Lorentz contracted nuclei causes that their interactions prevent higher occupation of the phase-space. Saturation of gluon density forces the gluons to recombine and carry higher fractions of the nucleon's momentum. The increase of R_i^A above unity for $10^{-2} \lesssim x \lesssim 10^{-1}$ called anti-shadowing is a consequence of shadowing at lower x.

18

With increasing x, R_i^A decreases below unity next to the anti-shadowing region. This effect is named according to its discoverer the European Muon Collaboration: the EMC effect. Its origin is still under discussion. According to [83], a possible explanation could be that a small fraction of nucleons within the nucleus forms short-range correlated pairs resulting in their substantial modification. At the same time, the rest of nucleons remains unmodified.

At x close to unity, R_i^A steeply increases due to the Fermi motion. Momenta of partons are modified with respect to those of free nucleons due to Heisenberg's uncertainty principle. Nucleons can be localized wherever in the nucleus which has a larger radius than the radius of the free nucleon. Therefore, partons in bound nucleons are more probable to carry very large x.
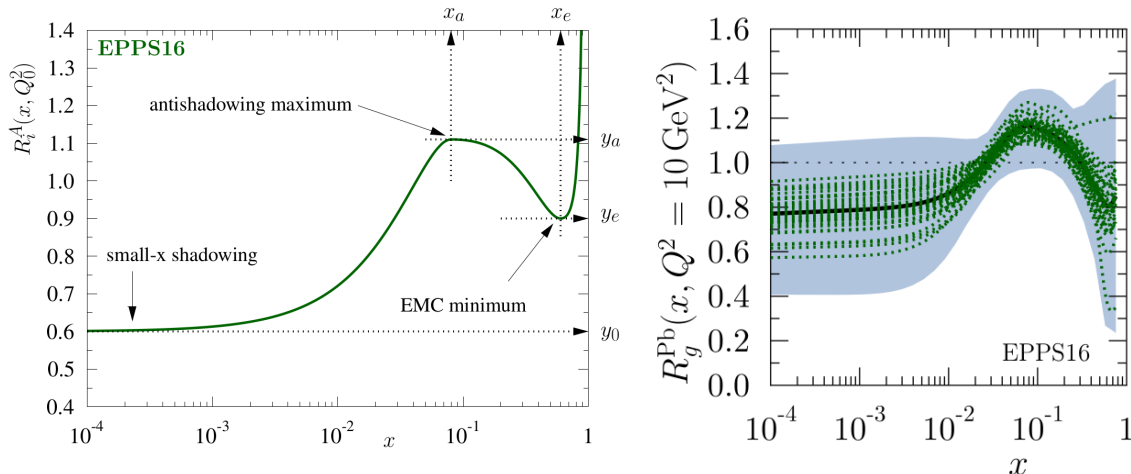
Figure 2.7: Left: Illustration of the fit function of $R_i^A(x, Q^2)$ used in the extraction of nPDFs. Right: Gluon nuclear modification function $R_g^{Pb}(x, Q^2 = 10 \text{ GeV}^2)$ for lead nuclei. The figures are taken from [81].

2.4.2 Coherent energy loss and p_T-broadening

Partons in hadrons may undergo multiple scattering already prior to the hard scattering taking place when hadrons traverse through each other. The multiple scattering can cause a shift of $\langle p_T \rangle$ towards higher values. This leads according to [84] to the so-called p_T-broadening, i. e. the suppression of J/ψ production in p–A collisions with respect to pp at low momentum and a simultaneous enhancement at p_T around a few GeV.

c$\bar{c}$ pairs are created during hard parton scattering. Pre-resonance pairs in a color-octet state traversing through nuclear matter undergo multiple scattering before they evolve into J/ψ mesons. This can induce radiation of coherent gluon. The coherent energy loss is responsible for the modification of J/ψ production as a function of x and therefore also as a function of rapidity according to [84].

2.4.3 Nuclear absorption

c$\bar{c}$ pairs can break up due to interactions with nuclear matter before they form the bound J/ψ state [85]. The probability of the nuclear absorption depends on the thickness of the nucleus affected by Lorentz contraction. Thus, nuclear absorption plays an important role at low collision energies. On the other hand, the formation time of c$\bar{c}$ pairs is comparable to the thickness of Lorentz contracted nuclei at LHC energies. Therefore, the nuclear absorption is expected to have negligible effect on J/ψ production at the LHC.

2.4.4 Measurement of J/ψ production in p–A collisions

Comparisons of measurements of J/ψ production in p–A and pp collisions can help to constrain the initial state effects and cold nuclear matter effects. J/ψ production cross sections in pp and pA collisions are usually compared using the nuclear modification factor R_{pA}

$$R_{pA} = \frac{1}{A} \frac{d^2\sigma_{pA}/dydp_T}{d^2\sigma_{pp}/dydp_T}, \tag{2.3}$$

where A is the atomic number. R_{pA} quantifies the difference between the cross section measured in p–A collisions and our expectation based on the measurement in pp collisions. R_{pA} is equal to unity in the case of no modification.

The nuclear modification factor in p–Pb collisions at $\sqrt{s_{NN}} = 5.02$ TeV at midrapidity R_{pPb} was recently measured by the ALICE Collaboration. R_{pPb} of inclusive and prompt J/ψ as a function of p_T is shown in Figure 2.8. The inclusive J/ψ production in p–Pb collisions is suppressed compared to the one in pp up to $p_T = 2$ GeV/c. R_{pPb} is consistent with unity above 2 GeV/c. The prompt J/ψ R_{pPb} measured in larger intervals starting from 1 GeV/c is consistent with the inclusive J/ψ R_{pPb}. The prompt J/ψ R_{pPb} measured by the ATLAS Collaboration above 8 GeV/c [86] is shown together with the ALICE measurement. It is consistent with unity in the full explored kinematic region and it is in good agreement with the ALICE measurement.
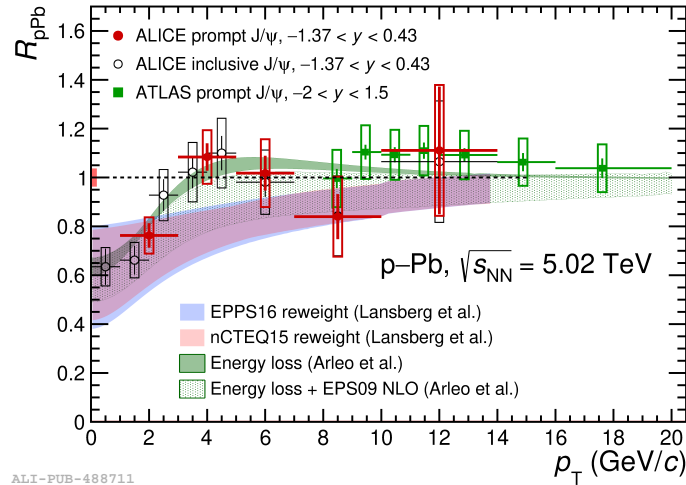
Figure 2.8: R_{pPb} of prompt and inclusive J/ψ as a function of transverse momentum measured by ALICE compared to the ATLAS measurement of prompt J/ψ [86]. The experimental results are compared to theoretical predictions [84, 87] which are shown as shaded areas. The figure is taken from [56].

R_{pPb} as a function of p_T is compared to theoretical predictions. The approach by Lansberg et al. [87] is based on Bayesian reweighting of the EPPS16 [81] and the nCTEQ15 [88] nPDF sets using data for inclusive open and hidden heavy-flavor production in p–Pb collisions at the LHC. The model from Arleo et al. [84] includes the effects of coherent energy loss and p_T-broadening. One version of this approach includes the cold nuclear matter effects mentioned above, whereas the second one also considers EPS09 nPDFs. Both versions are in good agreement with the presented measurements. The model predictions based solely on the modification of nPDFs with respect to PDFs in a free nucleon are consistent with the presented measurements. The models are consistent also with R_{pPb} as a function of rapidity at 5.02 TeV [56]. A reduction of model and/or measurement uncertainties is needed for the discrimination between different models.

2.4.5 J/ψ photoproduction in ultra-peripheral A–A collisions

Vector mesons such as the J/ψ can be created even in interactions when the impact parameter exceeds the sum of the nuclei radii. Such collisions are called ultra-peripheral collisions (UPCs). Although hadronic interactions are strongly suppressed in UPCs, the field strength of the nucleus electric field increases due to the Lorentz contraction. The field can interact with nucleons of the other nucleus. The interaction can be either coherent in the case the photon interacts with all nucleons consistently as a whole or incoherent when the photon interacts with a single nucleon. In the latter case, nuclei are typically dissociated and ejected neutrons can be detected by the ZDC detector. In the first case, the only detected signals from UPCs are usually vector meson decay products. The J/ψ production mechanism at the leading order is shown in the left panel of Figure 2.9. A photon produces a $c\bar{c}$ pair that interacts strongly with the second nucleus while producing a J/ψ meson.

Incoherent and coherent photoproduction can be distinguished by their typical transverse momentum of the produced vector mesons. The mean transverse momentum $\langle p_T \rangle$ is inversely proportional to the size of the nucleon or nucleus the photon interacts with. Values around 60 MeV/c are typical for coherent photoproduction, whereas 500 MeV/c is a typical $\langle p_T \rangle$ for the incoherent case [89]. Contributions of these two processes can be deduced from a Monte Carlo template fit of the measured p_T distribution as shown in the right panel of Figure 2.9.
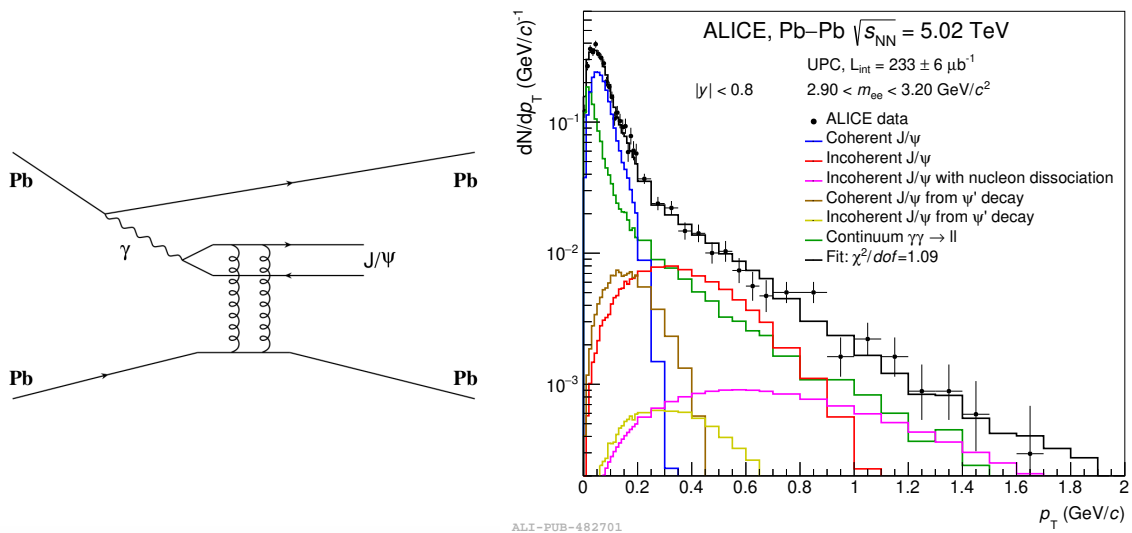
Figure 2.9: Left: J/ψ production mechanism in UPCs at the leading order. (Figure is taken from [90].) Right: Number of coherent photoproduction J/ψ candidates as a function of transverse momentum. The distribution is fitted with Monte Carlo templates corresponding to different production mechanisms. (Figure is taken from [89].)

Coherent J/ψ photoproduction is in the focus of experimental interest since it can be used to probe the modification of gluon PDFs in a nucleus at low x where uncertainties are large. The gluon shadowing factor can be obtained using measured cross sections of coherent J/ψ photoproduction in Pb–Pb UPCs together with approximations of the same cross section without modifications of PDFs based on $\gamma p \to V p$ measurements, such as discussed in [91]. The coherent J/ψ cross section in Pb–Pb collisions at 5.02 TeV was recently measured by ALICE at forward rapidity [92] and midrapidity [89]. The measurement at forward rapidity is the sum of production processes related to $x \approx 10^{-5}$ and $x \approx 10^{-2}$ because the relevant x depends on which nucleus is being probed

$$x_{1,2} = (M_{\mathrm{J}/\psi}/\sqrt{s_{\mathrm{NN}}})e^{\pm y}. \tag{2.4}$$

Since the production at $x \approx 10^{-5}$ can be neglected, it is concluded that the measurement of coherent photoproduction is consistent with a moderate gluon shadowing factor around 0.8 at $x \approx 10^{-2}$ and

scale of charm quark mass for $-4 < y < -2.5$. Using the measurement at midrapidity, a smaller gluon shadowing factor around 0.65 is found for $x \in (0.3, 1.4) \times 10^{-3}$.

J/ψ is not photoproduced only in UPCs, but also in more central collisions with hadronic interactions. Due to the very different physics origin, the J/ψ from photoproduction is background for measurements performed using hadronic collisions and should be removed. This is also case for this work.

2.5 Early measurements and ideas on J/ψ production in A–A collisions

The J/ψ has been subject to vivid experimental and theoretical studies since 1986 when Matsui and Satz suggested J/ψ suppression in heavy-ion collisions as an unambiguous signature of the QGP presence [93]. According to the initial idea presented in this publication, the c$\bar{c}$ potential is screened in the deconfined medium by color charges in analogy to the Debye screening of electric charge. In this picture, the Cornell potential in Equation 2.1 is modified in a hot and deconfined medium to

$$V(r) = -\frac{\alpha_{\text{eff}}}{r} \cdot e^{-r/r_{\text{D}}(T)}, \qquad (2.5)$$

where α_{eff} is the effective coupling and r_{D} is the screening radius. The confinement term from 2.1 is screened and the Coulomb term is attenuated by the exponential. When r_{D} decreases below the binding radius, quark and anti-quark do not form a bound state. The screening of c$\bar{c}$ potential results in the suppression of J/ψ production in A–A collisions with respect to the pp collisions where no QGP is expected.

This simple idea presented in [93] has been further developed. Whereas most of the mass of hadrons containing light quarks is determined by the interactions between the quarks, most of quarkonium masses originate from the mass of heavy quarks. Therefore, the radii of quarkonia are smaller than those of light-flavor hadrons. Consequently, quarkonia do not dissociate at the critical temperature T_c. The temperature of dissociation onset for different quarkonia species depends on their binding energy. Quarkonia with higher binding energy are more tightly bound and dissociate at higher temperatures. There are two main modern approaches to calculate these temperatures beside other quarkonium properties—potential models and lattice QCD [94]. Sequential dissociation of different quarkonia species has been suggested as tool to determine the QGP temperature.

The suppression of J/ψ and ψ(2S) production in A–A collisions beyond expectations from p–Pb collisions was for the first time observed at the Super Proton Synchrotron (SPS) in Pb–Pb collisions [95]. It was referred to as anomalous suppression. At that time, it was already known that charmonia are suppressed with respect to the production in pp collisions also in p–A collisions, where no QGP is expected. Therefore, the conclusions were drawn after considering expected values for the nuclear absorption.

Since RHIC began its operation, the modification of J/ψ production in A–A collisions is commonly expressed in form of a nuclear modification factor R_{AA}

$$R_{\text{AA}} = \frac{\mathrm{d}N_{\text{AA}}^{\text{J}/\psi}/\mathrm{d}y}{\langle N_{\text{coll}}\rangle \mathrm{d}N_{\text{pp}}^{\text{J}/\psi}/\mathrm{d}y} = \frac{\mathrm{d}N_{\text{AA}}^{\text{J}/\psi}/\mathrm{d}y}{\langle T_{\text{AA}}\rangle \mathrm{d}\sigma_{\text{pp}}^{\text{J}/\psi}/\mathrm{d}y}, \qquad (2.6)$$

where $\mathrm{d}N^{\text{J}/\psi}/\mathrm{d}y$ is the J/ψ yield per unit of rapidity, $\langle N_{\text{coll}}\rangle$ is the average number of binary nucleon-nucleon collisions in an A–A collision, and $\langle T_{\text{AA}}\rangle$ is the average nuclear overlap function. When R_{AA} is equal to unity, there is no modification of J/ψ production in A–A collisions compared to pp collisions. R_{AA} below unity indicates a J/ψ suppression in A–A collisions.

RHIC operation started in 2000 and brought a number of measurements of J/ψ production at higher energies than available at the SPS and, together with them, new exciting questions about J/ψ production. PHENIX measurements of the inclusive J/ψ R_{AA} in Au–Au and Cu–Cu collisions at $\sqrt{s_{\text{NN}}} = 200$ GeV at midrapidity are shown together with SPS results at midrapidity in the left panel Figure 2.10. Anomalous J/ψ suppression was reported in Pb–Pb collisions at $\sqrt{s_{\text{NN}}} = 17.3$ GeV

22

based on the shown SPS results. The RHIC collision energy is approximately ten times larger than the SPS energy. Therefore, also the energy density in collisions at RHIC is larger and should lead to a stronger J/ψ suppression. However, the PHENIX results in Au–Au collisions are consistent with the SPS measurements, which was not understood at the time when the RHIC results were published. A peculiar picture arose as well with the measurement of J/ψ R_{AA} at forward rapidity at RHIC. The inclusive J/ψ R_{AA} at forward rapidity [96] in Au–Au collisions is compared to the same measurement at midrapidity [97] in the right panel of Figure 2.10. J/ψ production is less suppressed at midrapidity than at forward rapidity although the energy density is larger at midrapidity.

Since the suppression at larger energy density did not increase, an additional production mechanism relevant at large energy density was suggested. The missing piece of the puzzle is J/ψ (re)generation. An uncorrelated charm quark and anti-quark can meet during the QGP evolution or at the phase boundary and form a J/ψ meson. Probability of J/ψ (re)generation increases with energy due to the general rise of the charm production cross section with $\sqrt{s}$. Thus, (re)generation plays a key role especially at the LHC energies with larger charm densities.
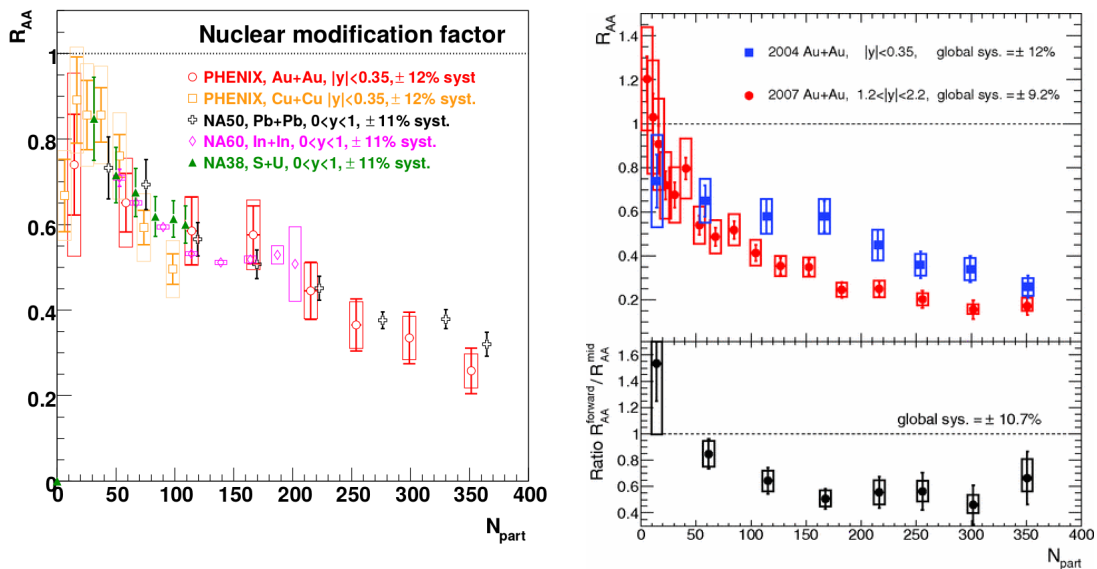
Figure 2.10: Left: Inclusive J/ψ nuclear modification factor R_{AA} measured by the SPS experiments NA38, NA50 and NA60 in In–In, S–U, and Pb–Pb collision and the RHIC experiment PHENIX in Au–Au and Cu–Cu collisions as a function of the participant number. (Figure is taken from [98].) Right: Inclusive J/ψ nuclear modification factor R_{AA} at forward rapidity [96] and at midrapidity [97] and their ratio measured by the PHENIX experiment in Au–Au collisions [96].

2.6 Models of prompt J/ψ production in heavy-ion collisions

2.6.1 Statistical Hadronization Model

The statistical hadronization model (SHM) presented in Section 1.3.1 has been extended to also describe charm production [99, 100, 21, 101]. Similarly as in the case of hadrons formed from light quarks, J/ψ mesons are generated within this model at the phase boundary. The charm quarks are assumed to be thermalized.

Thermal production of heavy charm quarks, unlike in the case of light and strange quarks, is negligible at the LHC energies. It is suppressed with respect to the the total charm production approximately by a factor of thirty. Charm quarks and anti-quarks are produced almost exclusively during initial hard scatterings and their numbers are conserved during the system evolution as

expressed by the balance equation:

$$N_{c\bar{c}} = \frac{1}{2} g_c V \left(\sum_i n^{\mathrm{th}}_{D_i} + \sum_i n^{\mathrm{th}}_{\Lambda_i} + \dots \right) + g_c^2 V \left(\sum_i n^{\mathrm{th}}_{\psi_i} + \sum_i n^{\mathrm{th}}_{\chi_i} + \dots \right), \qquad (2.7)$$

where n^{th} is the grand-canonical density of a hadron species and $N_{c\bar{c}}$ the number of $c\bar{c}$ pairs. The fugacity factor g_c represents charm enhancement with respect to the thermal production. Resonances built from lighter, thermally produced quarks of a similar mass have almost three orders lower yields than the J/ψ meson. In other words g_c^2 is approximately 1000.

$N_{c\bar{c}}$ is the total charm yield in Pb–Pb collisions. It is estimated based on measurements of the charm cross section in pp collisions, shadowing and the nuclear overlap function T_{AA}. The yields of charm hadrons of different species are obtained using the thermal grand-canonical densities, the volume of the fireball from the thermal fit and the fugacity factor. For example, the J/ψ yield is determined by

$$N_{\mathrm{J}/\psi} = g_c^2 V n^{\mathrm{th}}_{\mathrm{J}/\psi}. \qquad (2.8)$$

An illustration of charm production at LHC and RHIC energies is shown in the left panel of Figure 2.11. At lower energies, the mean number of $c\bar{c}$ pairs created during hard scatterings is lower than at higher energy. Charm quarks and anti-quarks produced together in the same hard scattering process usually do not form charmonium due to color screening and drift apart from each other. The probability that the charm quark meets at the hadronization phase a charm anti-quark is low due to low charm density. Open charm mesons form at the phase boundary. At high LHC energies, the number of $c\bar{c}$ pairs can reach numbers around 200 [21] giving charm quarks and their anti-quarks larger chance to generate charmonium at the phase boundary. Thus, (re)generation is especially important for the description of J/ψ production in A–A collisions at the LHC.
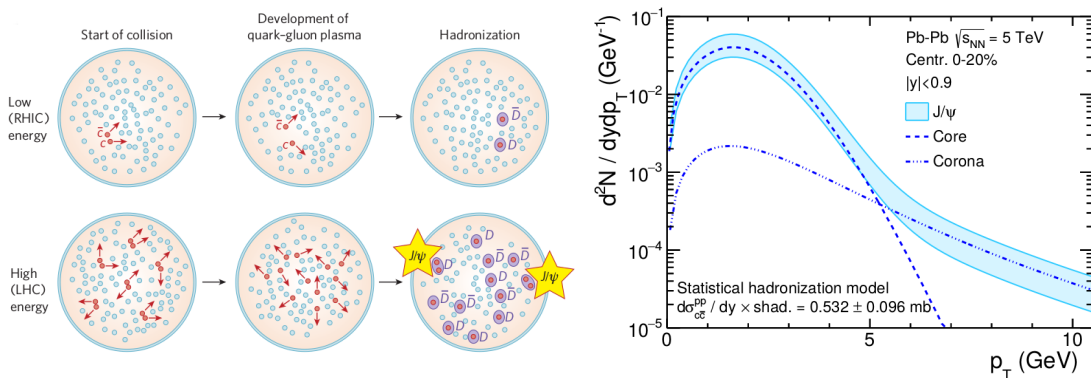
Figure 2.11: Left: Illustration of charm production in A–A collisions at low energies (RHIC) and high energies (LHC). The blue small circles represent light quarks and anti-quarks, red circles charm quarks and anti-quarks. The beginning of the collision is depicted on the left. It is followed by QGP and hadronization phases. (Figure is taken from [21].) Right: Transverse-momentum spectrum at midrapidity ($|y| < 0.9$) of J/ψ in Pb–Pb collisions at $\sqrt{s_{\mathrm{NN}}} = 5$ TeV with centrality 0–20% as predicted by [101]. Contributions for thermal core and corona parts are shown as dashed and dash-dotted lines. (Figure is taken from [101].)

The state-of-the-art approach of the SHM does not only consider the J/ψ production in a core of a heavy-ion collision, where the QGP is formed and charm quarks are assumed to be thermalized. The corona that represents outer regions of the heavy-ion collision with nucleons undergoing one or only a few nucleon-nucleon collisions is included. This is not sufficient to create the QGP.

In the SHM for charm hadrons (SHMC) [101], the p_{T} distribution is obtained using the core-corona approach. In the core, the velocity of charm quarks is obtained as the sum of random thermal motion and collective velocity of the expanding QGP. The J/ψ mesons inherit the momenta of their

constituents. In the corona part, the p_T shape is obtained by a fit to the p_T spectra in pp collisions. The resulting transverse momentum spectrum can be seen in the right panel of Figure 2.11. The J/ψ yield from the core part dominates at low momentum, whereas J/ψ production in the corona dominates at high transverse momentum.

2.6.2 Transport models

In the transport models, charm quarks do not have to be thermalized as in the case of the SHM. Charmonia are transported through the expanding fireball, and they dissociate and form again. The formation can only occur when the QGP has a temperature below the dissociation temperature specific for every charmonium state or, alternatively, at the phase boundary.

A cartoon illustrating a time evolution of a correlated charm-anti-charm quark pair in a heavy-ion collision is shown in Figure 2.12. The initial phase of heavy-ion collisions is treated within transport approaches in a very similar way as in the case of the SHM. c$\bar{c}$ pairs are created during hard scatterings at the beginning of a collision. The number of c$\bar{c}$ pairs is based on charm cross section measurements in pp collisions. Modifications of nPDFs with respect to the proton PDFs and cold nuclear matter effects such as p_T-broadening or nuclear absorption are usually considered. The nuclear absorption is neglected at LHC energies for reasons discussed in Subsection 2.4.3.

Figure 2.12: Schematic time evolution of a correlated charm-anti-charm quark pair in an expanding fireball in an ultra-relativistic heavy-ion collision. (Figure is taken from [102].)

Correlated c$\bar{c}$ pairs dissociate in the QGP and single charm quarks and their anti-quarks move through the medium. Charm quarks are in the model of Rapp et al. [103, 104, 105] incompletely thermalized. On the other hand, the model of Zhou et al. [106, 107] assumes thermalized charm quark distribution.

When the temperature of the medium decreases below the charmonium dissociation temperature, charmonia can be continuously formed and broken up. Dissociation reactions are specific to different models. The model of Rapp et al. considers scattering with surrounding light partons p of the heat bath $\psi + p \rightarrow c + \bar{c} + p$. The model of Zhou et al. assumes gluon dissociation $\psi + g \rightarrow c + \bar{c}$ that is expected to be the dominant process in the QGP. Charmonia are regenerated by reverse processes.

Charmonia are transported through the expanding fireball using hydrodynamics approaches. The charmonium dissociation and (re)generation is controlled via the Boltzmann equation using different assumptions. For example, the approach of Rapp et al. assumes that the dissociation and (re)generation do not depend on the momenta of charmonia. After the integration of the Boltzmann equation over momentum and space, one obtains the time evolution of charmonium yields by solving

of the kinetic rate equation [104]:

$$\frac{\mathrm{d}N_\psi}{\mathrm{d}\tau} = -\Gamma_\psi(T(\tau))[N_\psi(\tau) - N_\psi^{eq}(T(\tau))], \tag{2.9}$$

where Γ_ψ is the dissociation and formation rate, N_ψ^{eq} is the number of charmonium states in the equilibrium limit, and N_ψ is the number of charmonium states. In addition, charmonia are formed also at the phase boundary.

2.6.3 Comovers

In addition to the transport approaches and the SHM, there is also a model prediction for J/ψ production in A–A collisions considering the break up of J/ψ mesons by comovers [108]. This model was originally developed to describe J/ψ production at much lower SPS energies. The original version has been updated to describe the larger LHC energies by adding J/ψ (re)generation similar to the transport models. At lower energies, comovers are interpreted as hadrons, whereas they are considered as hot partonic medium at high energies.

The break up of J/ψ mesons is proportional to the J/ψ-meson density, the density of comovers and the dissociation cross section. The dissociation cross section is obtained by fits to low energy data. The (re)generation term is proportional to the squared charm density and a (re)generation cross section that is assumed to be identical to the dissociation cross section. From the nuclear effects, shadowing is considered by modifying the densities mentioned above using measurements in pp collisions.

2.7 Recent LHC measurements of J/ψ production in Pb–Pb collisions

First heavy-ion results from the LHC are from Pb–Pb collisions at $\sqrt{s_{\mathrm{NN}}} = 2.76$ TeV collected in November 2010. Measurements of inclusive J/ψ belong to the first harvest of the LHC physics results using data samples at this center-of-mass energy per nucleon-nucleon pair. The inclusive J/ψ R_{AA} at forward rapidity as a function of midrapidity charged-particle density $\mathrm{d}N_{\mathrm{ch}}/\mathrm{d}\eta|_{\eta=0}$ measured by ALICE in Pb–Pb collisions is shown in the left panel of Figure 2.13. $\mathrm{d}N_{\mathrm{ch}}/\mathrm{d}\eta|_{\eta=0}$ reflects the energy density of the medium. R_{AA} does not exhibit a strong dependence on $\mathrm{d}N_{\mathrm{ch}}/\mathrm{d}\eta|_{\eta=0}$. In a pure color screening scenario, suppression should increase with $\mathrm{d}N_{\mathrm{ch}}/\mathrm{d}\eta|_{\eta=0}$. The measurement is compared to the PHENIX results at forward rapidity and midrapidity presented in Section 2.5. The ALICE R_{AA} exceeds the PHENIX results in most central events at forward rapidity approximately by a factor of three above $\mathrm{d}N_{\mathrm{ch}}/\mathrm{d}\eta|_{\eta=0} = 600$. This fact supports the (re)generation scenario since (re)generation should be stronger in collisions with higher center-of-mass energy.

The inclusive J/ψ R_{AA} at midrapidity as a function of transverse momentum p_{T} is shown in the right panel of Figure 2.13. The ALICE measurement [109] is obtained using events with centrality 0–40% for first two p_{T} intervals and 0–50% for the highest p_{T} interval. The J/ψ R_{AA} measured by ALICE decreases with increasing p_{T}. The PHENIX results [111] at 0.2 TeV for centrality 0–40% manifest in contrast to the ALICE measurement a stronger suppression up to $p_{\mathrm{T}} = 4$ GeV/c. A CMS measurement at high p_{T} [112] in a broader rapidity range is consistent with the ALICE measurement at the same energy. The measurements are compared to two predictions from transport models for the LHC energy. Whereas the J/ψ R_{AA} measured by ALICE exceeds the prediction of Zhou et al. [106], it is in good agreement with the model of Rapp et al. [104, 113]. Both models as well as the data at the LHC energy exhibit the same trend as a function of p_{T} typical for J/ψ production enhanced by (re)generation.

In Run 2, the ALICE Collaboration collected a sample of Pb–Pb collisions at even higher center-of-mass energy $\sqrt{s_{\mathrm{NN}}} = 5.02$ TeV. The second Fourier coefficient of the inclusive J/ψ azimuthal distribution at forward rapidity using this data sample [114] is shown in Figure 2.14. A sizable elliptic flow suggests that J/ψ mesons inherit some of the medium's anisotropic flow. This is expected only when J/ψ constituents, i.e. the charm quark and its anti-quark, are unbound at least for part of
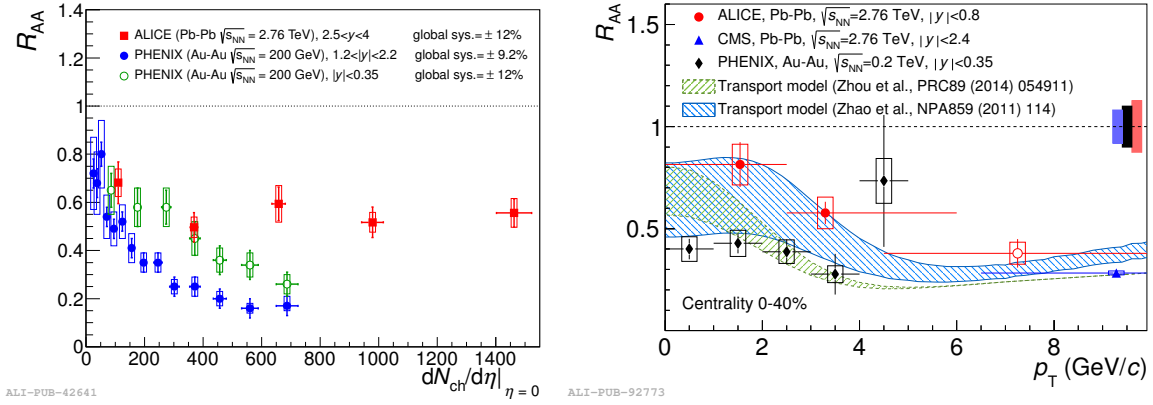
Figure 2.13: Left: Inclusive J/ψ R_{AA} at forward rapidity as a function of midrapidity charged-particle density measured by ALICE in Pb–Pb collisions at $\sqrt{s_{NN}} = 2.76$ TeV [109] compared to the PHENIX results in Au–Au collisions at 0.2 GeV at forward rapidity and midrapidity [96]. (Figure is taken from [109].) Right: Inclusive J/ψ R_{AA} at midrapidity in Pb–Pb collisions at $\sqrt{s_{NN}} = 2.76$ TeV as a function of transverse momentum p_T measured by ALICE [110] compared to PHENIX results for Au–Au collisions at 0.2 TeV [111], CMS results for Pb–Pb collisions at $\sqrt{s_{NN}} = 2.76$ TeV [112], and model predictions of Zhou et al. [106] and Rapp et al. [104, 113] (referred to as Zhao et al. in the figure). (Figure is taken from [110].)

the QGP stage to have a chance to thermalize. Since surviving primordial J/ψ mesons experience the whole evolution of a heavy-ion collision in a colorless stage, they are expected to have only very limited elliptic flow attributed to path-length dependent energy-loss effects. Model predictions of Rapp et al. [105] for primordial J/ψ only and for the sum of primordial, (re)generation and non-prompt contributions are shown together with the measurement. The measured J/ψ elliptic flow highly exceeds the prediction for pure primordial J/ψ as expected, and it is consistent with the sum of contributions up to $p_T = 4$ GeV/c. However, the model undershoots the measurement between 4 and 10 GeV/c.

It is generally accepted nowadays that (re)generation plays a crucial role in inclusive J/ψ production at low transverse momentum and high collision energies thanks to abundant experimental evidence provided by experiments at the LHC. However, the question whether (re)generation takes place during the QGP evolution and at the phase boundary or exclusively at the phase boundary remains open. An answer may arise when more precise measurements and theoretical predictions become available. The analysis of inclusive J/ψ yields in Pb–Pb collisions at $\sqrt{s_{NN}} = 5.02$ TeV, as presented in this work, is part of this effort.
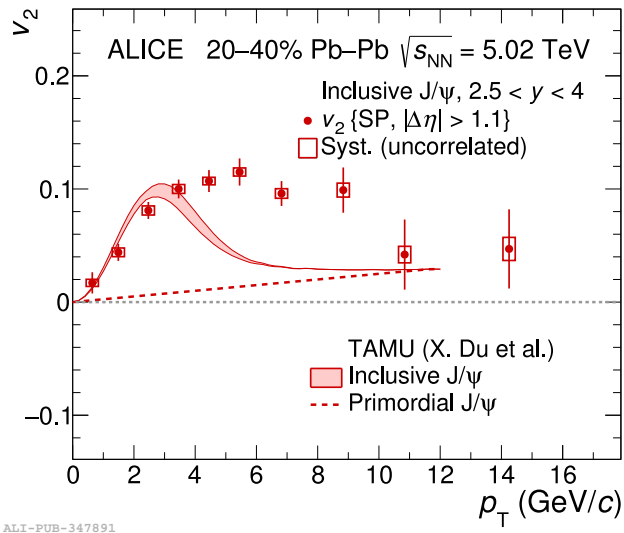
Figure 2.14: Inclusive J/ψ elliptic flow coefficient v_2 as a function of transverse momentum at forward rapidity measured by ALICE in Pb–Pb collisions at $\sqrt{s_{NN}} = 5.02$ TeV with centrality 20–40% [114] compared to the predictions from the transport model of Rapp et al. [105] (referred to as X. Du et al. in the figure). (Figure is taken from [114].)

28

A Large Ion Collider Experiment (ALICE) at the LHC

3.1 The Large Hadron Collider

The Large Hadron Collider (LHC) is the largest and most powerful hadron collider ever built in terms of collision energy and luminosity. The LHC with its circumference of 26.7 km is located underground in Switzerland and France close to Geneva. It uniquely provided so far lead-lead (Pb-Pb) collisions up to the center-of-mass energy per nucleon-nucleon pair of $\sqrt{s_{NN}} = 5.02$ TeV, xenon-xenon (Xe-Xe) collisions at $\sqrt{s_{NN}} = 5.44$ TeV, proton-lead (p-Pb) collisions up to $\sqrt{s_{NN}} = 8.16$ TeV and proton-proton (pp) collisions up to the center-of-mass energy $\sqrt{s} = 13$ TeV.
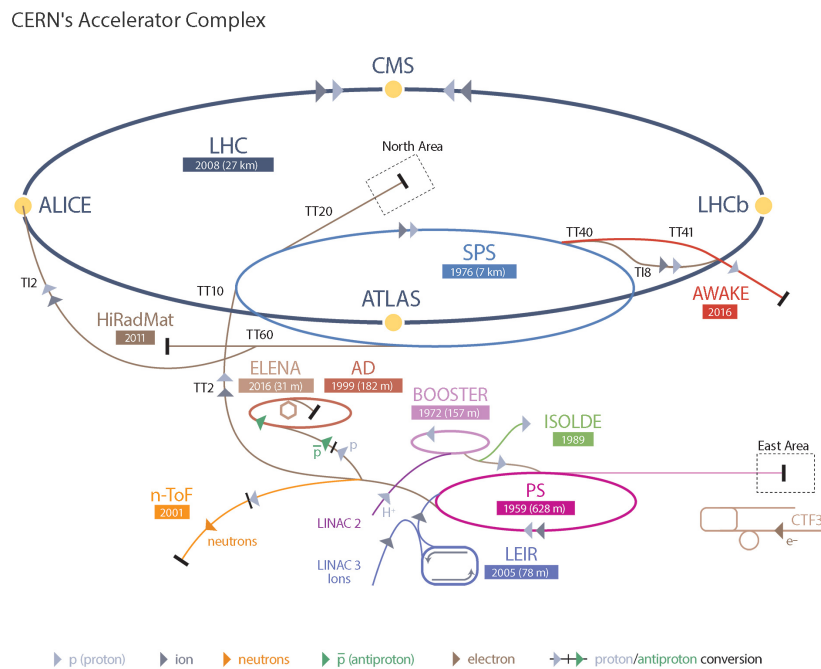
Figure 3.1: CERN's accelerator complex. The path of protons starting in LINAC 2 is marked by light gray arrows and the path of ions starting in LINAC 3 by dark gray arrows. Protons and ions travel on same trajectories since they get to the PS. (Figure is taken from [115].)

The LHC is part of CERN's accelerator complex as shown in Figure 3.1. Hydrogen, lead and xenon atoms are stripped of their electrons and pre-accelerated starting in LINAC 2 in case of protons and in LINAC 3 in case of heavier ions and ending at the Super Proton Synchrotron (SPS).

The whole acceleration process reaches its final phase in the two LHC rings. Two beams of hadrons travel there in bunches in opposite directions while being bent by powerful superconducting dipole magnets able to generate magnetic field up to 8.3 T. The beams intersect at four points where the large LHC experiments are placed: A Toroidal LHC Apparatus (ATLAS) [116], Compact Muon Solenoid (CMS) [117], Large Hadron Collider beauty (LHCb) [118, 119] and ALICE [120]. More details about LHC can be found in [121].

ATLAS and CMS are general-purpose particle physics detectors studying physics within and beyond the Standard Model. These two collaboration are known particularly for their discovery of a new particle compatible with the Standard Model Higgs boson hypothesis in 2012 [122, 123] and later detailed measurements of its properties. The LHCb detector was designed to study various aspects of heavy-flavor physics including CP violation in decays of heavy flavor hadrons. One of the well known measurements of LHCb collaboration is for example the discovery of pentaquarks [124]. ALICE is the only experiment at the LHC specifically build to study heavy-ion physics. Its design is driven by its physics goals—to study strongly interacting matter at extreme temperature and density.

In this thesis, the analysis of inclusive J/ψ production using data sets collected by ALICE is presented. Therefore, the ALICE detector and its sub-systems will be described in detail in this chapter with a special focus on the detector systems crucial for the J/ψ measurement at midrapidity. Since the data presented in this thesis were collected during Run 2, the ALICE Run 2 setup will be described. The upgrade of ALICE for Run 3is then discussed in Section 3.7 of this chapter.

3.2 ALICE coordinate system

The ALICE coordinate system is a right-handed orthogonal Cartesian system with an origin at the beams interaction point [125]. The x-axis is perpendicular to the beam direction and points to the center of the accelerator. The y-axis is perpendicular to the beam direction and x-axis and pointing upward from the origin. The z-axis parallel to the local beam direction is than defined by position of x- and y-axis and the right-hand rule. The Cartesian coordinates can be converted to a spherical coordinate system by

$$x = r \sin\theta \cos\phi, \quad y = r sin\theta \sin\phi, \quad z = r \cos\vartheta. \quad (3.1)$$
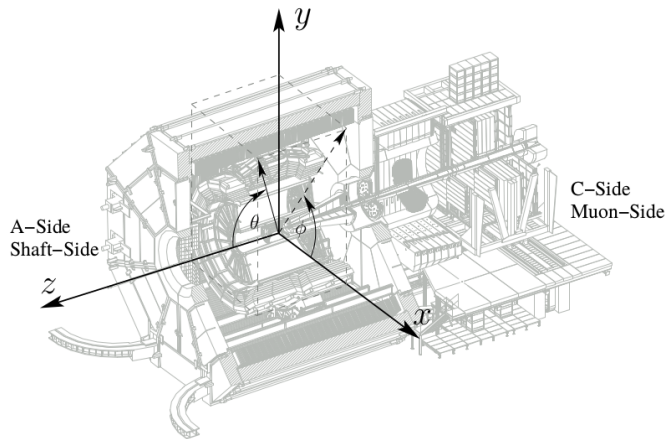
Figure 3.2: The ALICE detector and its coordinate system. (Figure is taken from [126].)

3.3 Overview of the ALICE detector

The ALICE detector is designed to study events with the extremely large multiplicity densities typical for central Pb–Pb collisions. Excellent particle identification (PID) and tracking capabilities are ensured up to $\frac{\mathrm{d}N}{\mathrm{d}\eta}\big|_{\eta\approx0} = 8000$ [120], where η is track pseudorapidity. ALICE can be subdivided into two systems according to their pseudorapidity acceptance: the central-barrel detectors at midrapidity ($|\eta| < 0.9$) and the Muon Spectrometer at forward rapidity. The ALICE detector layout is shown in Figure 3.3.

THE ALICE DETECTOR

a. ITS SPD (Pixel)
b. ITS SDD (Drift)
c. ITS SSD (Strip)
d. V0 and T0
e. FMD

1. ITS
2. FMD, T0, V0
3. TPC
4. TRD
5. TOF
6. HMPID
7. EMCal
8. DCal
9. PHOS, CPV
10. L3 Magnet
11. Absorber
12. Muon Tracker
13. Muon Wall
14. Muon Trigger
15. Dipole Magnet
16. PMD
17. AD
18. ZDC
19. ACORDE
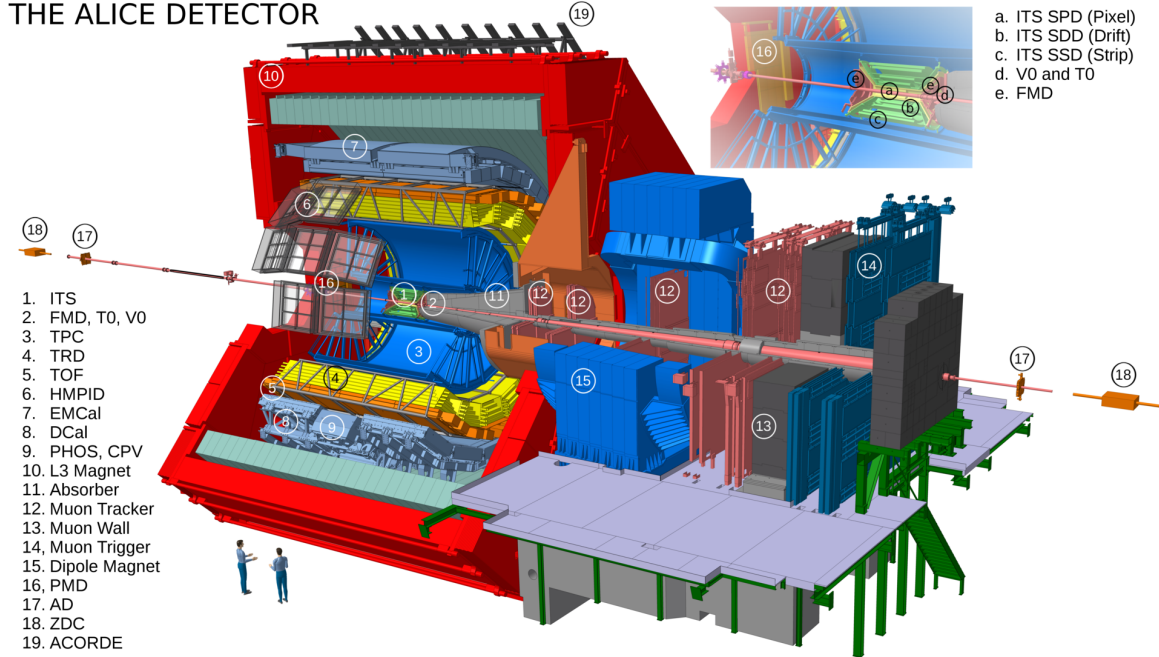
Figure 3.3: Sketch of the ALICE setup and its detector subsystems. Different detectors are indicated by numbers. (Figure is taken from [127].)

The innermost detectors of the Central Barrel providing tracking and PID, i.e. ITS, TPC, TRD and TOF, are introduced in more details in this chapter. In addition to them, there are multiple detectors improving and broadening PID capabilities of the ALICE detector. The electromagnetic calorimeters Photon Spectrometer (PHOS), EMCal and Di-jet Calorimeter (DCal) measure energy deposited by photons and electrons. EMCal and DCal covering opposite radial regions allow to trigger on and measure energy deposited by jets and di-jets—single or double collimated sprays of particles originating from high energy partons. The High Momentum Particle Identification Detector (HMPID) enhances hadron PID capabilities at high momentum. The Central Barrel detectors are surrounded by a solenoid magnet generating a magnetic field of 0.5 T. This field bends charged-particle trajectories. Therefore, it enables ALICE to determine their momenta and distinguish between particles with opposite charge.

The Muon Spectrometer provides muon identification, reconstruction of their trajectories and triggering on single muons or muon pairs at rapidity $-4 < \eta < -2.5$. Hadrons at this rapidity are stopped by a front absorber. Five tracking chambers are placed behind the absorber with respect to the interaction point, one of them in a dipole magnet bending muon trajectories. After passing the tracking chambers, muons reach the Muon Trigger. Due to excellent separation of muons from hadrons stopped by the front absorber, broad palette of rare quarkonium states ($J/\psi, \psi(2S), \Upsilon(1S), \Upsilon(2S), \Upsilon(3S)$) is studied at forward rapidity via the dimuon decay channel.

The two forward-rapidity detectors Vertex 0 (VZERO) provide triggering for both, the Central Barrel and the Muon Spectrometer, and give access to event properties such us centrality. The

31

two Zero Degree Calorimeters (ZDC) located 114 m from the interaction point on both sides with respect to it are designed for event characterization via measurement of energy of spectator protons and neutrons. Since ALICE research is focused on hadronic Pb–Pb interactions, the ZDC serves for rejection of electromagnetic Pb–Pb interactions.

3.3.1 Inner Tracking System (ITS)

The Inner Tracking System [128] is a semiconductor detector system located at radii between 3.9 cm and 43.0 cm around the z-axis. This detector has a cylindrical shape and covers the pseudorapidity range $|\eta| < 0.9$. It consists of six layers employing three different silicon detector technologies. The two inner layers belong to the Silicon Pixel Detector (SPD), the two middle layers to the Silicon Drift Detector (SDD) and the two outer ones to the Silicon Strip Detector (SSD).

As the innermost central-barrel detector, the ITS plays a crucial role for finding primary vertices of collisions and secondary vertices due to particle decays, photon conversions and secondary reactions in detector material (e.g. spallation). The ITS improves the momentum resolution of tracks reconstructed by the central-barrel detectors and also serves as stand-alone tracking detector for particles with low transverse momenta not reaching the TPC (e.g. below 200 MeV/c in the case of pions). PID of these low-momentum particles is based on the energy loss dE/dx in the four ITS layers of the SDD and the SSD.

3.3.2 Time Projection Chamber (TPC)

The Time Projection Chamber [129] is the main ALICE tracking device in the Central Barrel with excellent PID capabilities. The TPC with its cylindrical shape surrounds the ITS detector in the radial direction and covers pseudorapidity region $|\eta| < 0.9$ for particles exiting the TPC at its outer radius. The active volume is filled with a gas mixture of Ar and CO_2. 88 m^3 active TPC volume are encapsulated in the field cage with an inner diameter of 84.8 cm, an outer diameter of 246.6 cm and a length of the cylindrical shell of 499.4 cm in the beam direction. The central electrode perpendicular to the beam direction divides the active volume into two halves, the A and C side. The homogeneous electric field is generated by applying a voltage of -100 kV to the central electrode while the readout planes are set to 0 V. The readout chambers, equipped with Multi-Wire Proportional Chambers (MWPC) and readout pad planes, are located at the A and C sides of the active volume.

The working principle of the TPC detector is illustrated in Figure 3.4. When a charged particle traverses the active volume, it ionizes gas atoms in its vicinity. Consequently, the particle leaves a track of ionized gas behind it. Liberated electrons travel in the opposite direction to the electric field $\vec{E}$ towards the readout chambers. Their drift velocity saturates due to collisions with the gas atoms to a constant value $v_D = \mu E$, where μ is the mobility of electrons. Thus, the z distance between a point passed by a charged particle and a readout chamber is proportional to the drift time. After traversing the active volume of the TPC, ionization electrons drift through open gating grid, which later after closing prevents ions to travel to the active TPC volume. Electrons are multiplied in the electric field in the vicinity of anode wires. Their voltage is set such that the number of amplification electrons and, therefore, also ionized gas atoms is proportional to the original amount of primary electrons liberated by the charged particle. Electrons are quickly collected by anode wires, whereas ions with smaller mobility than that of electrons induce mirror charges on pads in their vicinity. Afterwards, ions are collected by cathode wires. Charge signals on the pads serve for later reconstruction of the trajectory projection to the xy-plane and the energy loss calculation, which is crucial for PID. The first is introduced in more details in Section **??**, whereas the latter in Subsection 3.5. The gating grid is closed approximately 90 μs after the trigger, when all primary electrons have reached the readout chambers. This prevents ions from readout chambers to travel into the active volume and cause space-charge distortions of the electric field.
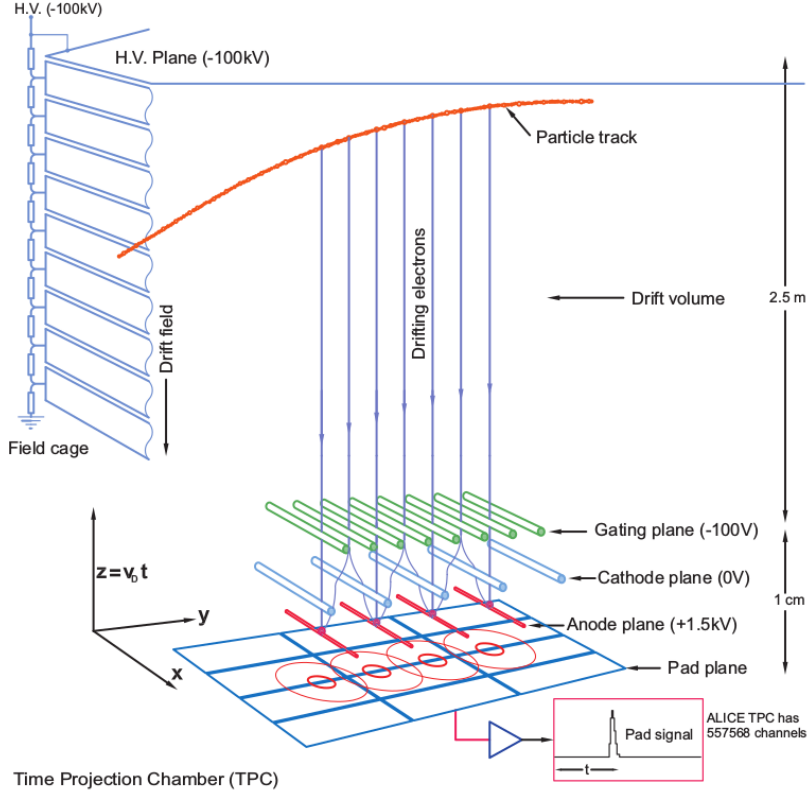
Figure 3.4: Illustration of the TPC working principle. (Figure is taken from [130].)

3.3.3 Transition Radiation Detector (TRD)

The Transition Radiation Detector [131] placed around the TPC consists of 540 modules containing 4.3 cm of a radiator and an MWPC each. It serves for triggering of high-p_T electrons and jets and the identification of electrons via the specific energy loss and, in particular, emitted transition radiation. Transition radiation photons are emitted when relativistic charged particle with $\gamma \gtrsim 1000$ crosses boundary of media with different dielectric constants. The threshold for emission of transition radiation is for electrons already at the momenta around 0.5 GeV/c, whereas it is much higher for all heavier particles such as pions. The transition radiation photons are absorbed by gas at the beginning of MWPC while atomic electrons are emitted. Thus, electrons with momentum in region of interest can be distinguished from other charged particle species by presence of additional signal caused by transition radiation.

3.3.4 Time-Of-Flight Detector (TOF)

The Time-Of-Flight [132] detector surrounding the TRD is the central-barrel detector most distant from the interaction point with full azimuthal acceptance. It consists of 90 modules with Multigap Resistive Plate Chambers. The TOF provides PID at intermediate momentum by measuring the arrival time of passing charged particles. The starting time for a TOF measurement is provided by the Cherenkov counters of the T0 detector [133]. When the time of flight and the momentum of a particle are know, the velocity can be determined. An example of the distribution of particle velocity as a function of momentum is shown in Figure 3.5. Bands correspond to different particle species. Background is caused by incorrect matching of some tracks with TOF hits due to large multiplicity in Pb–Pb collisions. Due to the excellent timing resolution of 80 ps, pions and kaons can be separated by TOF up to 2.5 GeV/c, and protons are identified up to 4 GeV/c [134].
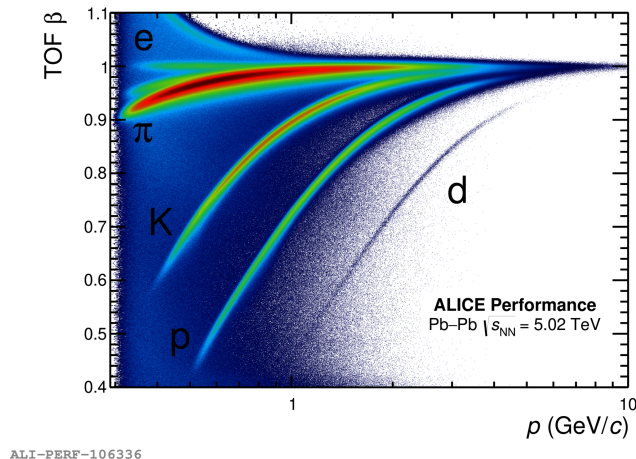
Figure 3.5: Distribution of particle velocity β as a function of momentum. (Figure is taken from [135].)

3.3.5 Vertex 0 (V0) Detector

The V0 detector is composed of two circular arrays, the V0A and the V0C, consisting of 32 plastic scintillator counters. The V0C is located 90 cm from the interaction point on the C side of AL-ICE, whereas the V0A at the distance 340 cm on the opposite site of the interaction point. The pseudorapidity ranges $2.8 < \eta < 5.1$ and $-3.7 < \eta < -1.7$ are covered by the V0A and the V0C, respectively.

The V0 detector is designed to measure the charged-particle multiplicity and to provide information about the time of the signal arrival with the resolution better than 1 ns. This allows to use the coincidence of the signals in both V0 counters as the Minimum-Bias (MB) trigger of physics events and to reduce the contamination of beam-gas interactions characteristic by their different timing of the deposited signals. Since the V0 signal amplitude is proportional to the event multiplicity and consequently also the overlap of two colliding nuclei, the centrality trigger is provided by setting a threshold on the energy deposited in the V0. The centrality definition based on the V0 amplitude will be described in Section 3.10.

3.4 Central barrel tracking

The Central Barrel event reconstruction [134] consists of several steps shown in Figure 3.6 that are briefly described in this section. The event reconstruction starts with merging signals in detectors to find space points. They serve for later reconstruction of tracks. This procedure is called clusterization. For example, a TPC cluster is defined as a peak in deposited charge found within five bins in the pad direction and five bins in the time direction.

A primary vertex is reconstructed using so-called SPD tracklets—pairs of clusters in two different innermost ITS layers. A preliminary primary vertex is defined as the space point to which the largest number of them points.

Helix trajectories of charged particles are build using clusters found in the detectors. They are described with five parameters $(y, z, \sin(\varphi), \tan(\varphi), 1/p_\mathrm{T})$. Since the parameters change along the path due to energy loss, the Kalman filter approach [136] allowing their variation along the path is used for the reconstruction. Track finding begins with constructing seeds of tracks from clusters at the outer radius of the TPC while using the primary vertex as a constraint. Tracks are later propagated inward to the inner radius of the TPC with higher occupancy. The maximum number of TPC clusters used for one TPC track is the number of tangential rows in the TPC readout chambers,
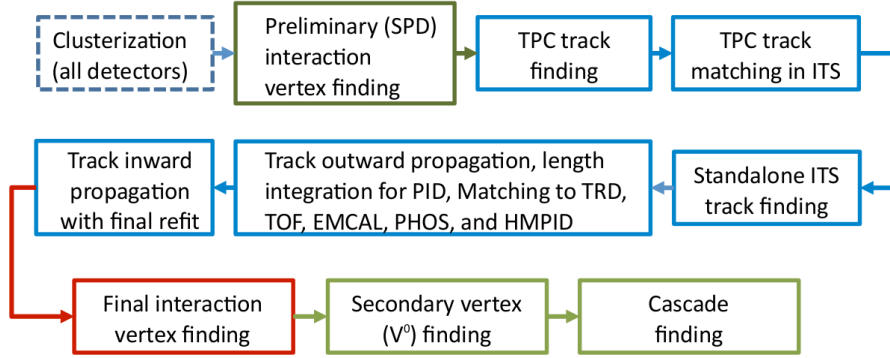
Figure 3.6: Flow of Central Barrel event reconstruction. (Figure is taken from [134].)

equal to 159. These tracks are further propagated inward through ITS.

Found tracks are refitted in the outward direction. Subsequently, an attempt to match tracks with TRD track segments and TOF clusters is made. Matching signals in EMCal, PHOS, and HMPID are assigned to tracks as well at that point. Finally, the tracks are propagated inward again using already found clusters while updating track information such as position or curvature. Resulting tracks are referred to as global tracks and used to determine the final primary vertex position. If a track is propagated to the inner radius of the TPC in the final inward propagation, it is referred to as a track with TPC refit. A track has the ITS refit if at least two ITS clusters are assigned to the track. Since the momentum of a track changes as the incident particle looses energy in detectors along its path, the momentum in the inner wall of the TPC p_{IN} differs from the momentum of a track in a point with the closest distance to the primary vertex. The momentum in the inner wall of the TPC p_{IN} associated to a track with the TPC refit is useful for the TPC related studies, since the energy loss in the TPC depends on the particle momentum in the TPC detector. More information related to TPC tracking can be found in [137].

After tracks and the primary interaction vertex are reconstructed, a search for secondary vertices of photon conversions and particle decays, so-called V^0 candidates, is performed. The reconstruction of an event is completed by a search for cascade decays such as $\Xi^- \rightarrow \Lambda^0 \pi^- \rightarrow p^+ \pi^- \pi^-$.

3.4.1 TPC space charge distortions, their correction and mitigation

Unexpectedly large space-time distortions [138] have been observed in the large interaction rate Pb–Pb data sets of Run 2 used for the data analysis presented in this thesis. They emerged at some of the TPC chamber boundaries and caused a deflection of ionization electrons up to several centimeters in the radial direction during the 2015 data taking. Places and amplitudes of distortions are depicted in Figure 3.7 as a function of the radius and the TPC sector coordinate. There are no or small space-charge distortions in most of the TPC volume. However, the distortions close to some of the readout chamber boundaries reach up to 6 cm, which would complicate track reconstruction. Thus, it was necessary to develop a correction procedure. Correction maps in 3D ($\mathrm{d}r, \mathrm{d}\varphi, \mathrm{d}z$) were created based on signals from unaffected external detectors. An interpolation of ITS, TRD and TOF track segments provided a reference that was compared to the positions of distorted clusters in order to create the correction maps. This method was used already in the reconstruction of 2015 Pb–Pb data.

In addition to the correction procedure, the distortions were mitigated during 2018 Pb–Pb data taking [139]. The distortions in one of the outer readout chambers were caused by two floating gating grid wires. Thus, the amount of ions escaping to the TPC active volume could be attenuated by increasing the voltage applied on neighboring gating grid wires. A cover electrode on a potential of 180 V was placed at ledges of affected inner readout chambers. It helped to attract electrons and prevent them from drifting towards the gaps between chambers where they would be amplified while releasing ions. Ions in this area would freely travel to the active volume due to the absence of

a gating grid in the gaps and cause distortions. After the exchange of readout chambers during the ALICE upgrade between Run 2 and Run 3, it was found that the amplification of electrons in the gaps and the resulting distortions were in the most of cases caused by anode wire tips penetrating part of or even the full insulation layer. The ALICE upgrade is discussed in Subsection 3.7. Due to the implementations mentioned above, the distortions were reduced below 1.5 cm in the 2018 data taking.
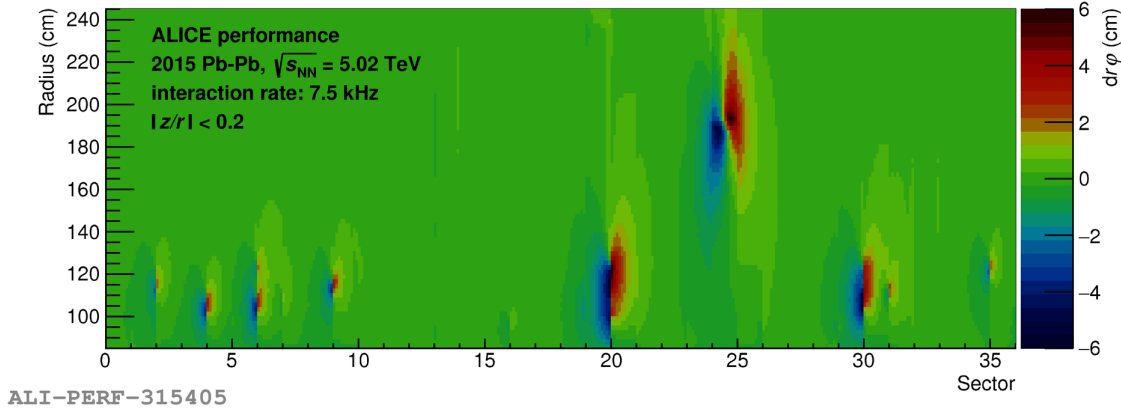
Figure 3.7: The radial space-charge distortions $\mathrm{d}r\varphi$ in 2015 Pb–Pb data as a function of the radius and the TPC sector coordinate for the largest drift distances ($|z/r| < 0.2$). (Figure is taken from [140].)

3.5 Particle identification (PID) with the TPC

The TPC PID is based on the measurement of energy loss in the active TPC volume. It can be described by the Bethe-Bloch equation discussed in Section 3.5.1 of this chapter. The energy loss signal in the ALICE TPC and PID via the number of standard deviations from a PID hypothesis as relevant for this thesis are discussed in the sections 3.5.2 and 3.5.3.

3.5.1 Bethe-Bloch Equation

The measurement of ionization energy loss of a particle traversing through a detector plays a crucial role in PID since the deposited energy is a function of only charge and invariant mass for a given momentum. Therefore, the particle can be identified when measuring simultaneously the momentum and energy loss. During the passage of charged particle through matter, it looses energy by inelastic collisions with atomic electrons, which causes ionization. An example of the TPC energy loss signal and expected $\langle \mathrm{d}E/\mathrm{d}x \rangle$ for different particle species is shown in Figure 3.8 as a function of the particle momentum. Curves of expected energy loss are different for different particle species allowing to identify particles in momentum regions, where the curves do not overlap.

The mean energy deposited per unit path length of moderately relativistic ($0.1 \lesssim \beta\gamma \lesssim 1000$) charged particles heavier than electrons due to interactions with atomic electrons is described by the Bethe-Bloch equation [141]:

$$\left\langle -\frac{\mathrm{d}E}{\mathrm{d}x} \right\rangle = 2\pi N_a r_e^2 m_e c^2 \rho \frac{Z}{A} \frac{z^2}{\beta^2} \left[\ln\left(\frac{2m_e c^2 \gamma^2 \beta^2 W_{\mathrm{max}}(\gamma\beta)}{I^2} \right) - 2\beta^2 - \delta(\gamma\beta) \right]. \qquad (3.2)$$

The factor β is the velocity of an incident particle relative to the speed of light, whereas γ is the Lorentz factor $\gamma = 1/\sqrt{1 - \beta^2}$. The other parameters of the equation are: N_a the Avogadro number, r_e the classical electron radius, I the mean excitation energy, W_{max} the maximum energy transfer in a single collision with an atomic electron, ρ the density of the material, z the charge number of

36

the incident particle, Z and A the atomic number and the atomic mass number of the material. Two effects have to be considered when obtaining the mean energy loss in addition to the case of heavier particles. Electrons are indistinguishable from the atomic electrons leading to the maximum transferable energy equal to one half of the total kinetic energy before the collision. In addition, the assumption for the invariant mass being larger than invariant mass of the atomic electrons is no longer valid for electrons and positrons. The mean energy loss of all particle species with same absolute value of charge follows same function of $\beta\gamma$ since the Bethe-Bloch function does not explicitly depend on the invariant mass of incident particle. This fact is useful in procedure of PID via the number of standard deviations from PID hypotheses as explained later in the subsection 3.5.3.

For $\beta\gamma < 1$, the term $1/\beta^2$ dominates causing a decrease of the energy loss. The minimum energy loss is reached at $\beta\gamma_{\mathrm{MIP}} \approx 3$. A charged particle with the minimum energy loss is often referred to as a minimum ionizing particle (MIP). The relativistic rise follows after the MIP region. It originates from the increasing maximum energy transfer in a single collision W_{max} and the Lorentz contraction of the Coulomb field causing a rise of the interaction cross section. The mean energy loss in the relativistic rise is proportional to $\ln(\beta^2\gamma^2)$.

As W_{max} increases, the probability that electrons that gain sufficient kinetic energy to cause secondary ionizations along their paths rises. Such electrons are often referred to as δ-electrons. Their presence haas a negative impact on the energy loss measurement because secondary electrons are often not associated with the original charged particle causing their emission. This results in measuring smaller energy than is in reality deposited by the charged particle.

3.5.2 The specific energy loss in the ALICE TPC

The calculation of the track PID signal in the TPC is based on the deposited charge in clusters associated with a track. In high-multiplicity environments such as central Pb–Pb collisions, the maximum charge Q_{max} of all pads in single clusters is used. This approach helps to minimize distortion of the PID signal due to cluster overlaps. The distribution of cluster charges Q_{max} associated with a track can be approximated by a Landau distribution with a characteristic tail towards higher values. Since the variance of the Landau distribution is undefined due to the divergence of the corresponding integral, the PID signal is obtained using a truncated-mean procedure. In this approach, only a fraction of clusters with lowest maximum charges is used to retrieve the PID signal referred to as the TPC $\mathrm{d}E/\mathrm{d}x$ signal. Typical choice of the fraction of clusters used in this procedure for the ALICE TPC is 0.6 [137]. This method minimizes the influence of missing energy carried away by δ-electrons and optimizes separation power between different particle species.

Clusters associated with more than one track are excluded from the PID signal determination to avoid PID signal bias. Clusters close to the chamber boundaries are not considered as well due to edge effects. Hence, the number of the TPC clusters used for PID is often lower than the number of clusters used for the final refit of a track. On the other hand, single-pad clusters are used for the PID purpose although they are not included in the final inward propagation of a track.

Since the signal in the pads is dependent on many parameters such as temperature and pressure of the gas mixture or a track topology, single pad charges and the $\mathrm{d}E/\mathrm{d}x$ signal have to undergo calibration. Details of calibration methods and the truncated-mean procedure can be found in [137, 142].

3.5.3 PID via number of standard deviations from PID hypothesis

In this thesis, the electron PID is based on the compatibility of the charged-particle $\mathrm{d}E/\mathrm{d}x$ with hypotheses of different particle species such as pions, protons and electrons. It is quantified by the number of standard deviations from the signal expected for different particle species $\langle \mathrm{d}E/\mathrm{d}x \rangle$:

$$n\sigma_{TPC,i} = \frac{\mathrm{d}E/\mathrm{d}x - \langle \mathrm{d}E/\mathrm{d}x \rangle_i}{\sigma}, \tag{3.3}$$

where i denotes a given particle species and σ is the resolution of the $\mathrm{d}E/\mathrm{d}x$ distribution.
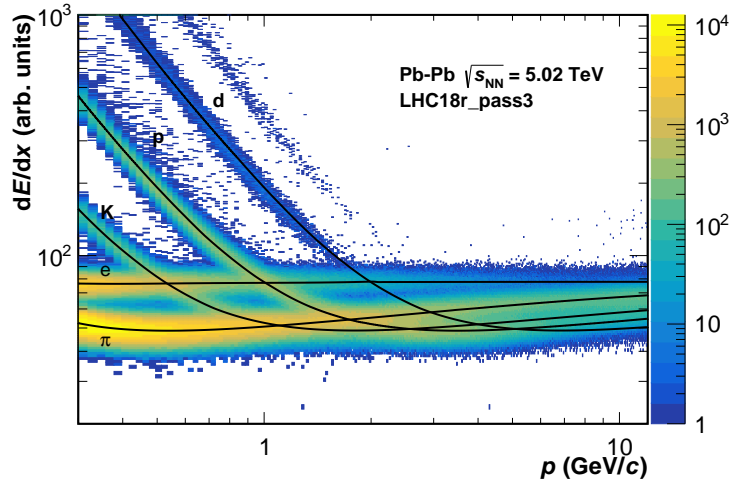
Figure 3.8: Specific energy loss of charged particles, $\mathrm{d}E/\mathrm{d}x$, in the TPC as a function of the particle momentum. Expected values for different particle species are shown as black lines. (Figure by Michael Ciupek.)

A first approximation of $\langle \mathrm{d}E/\mathrm{d}x \rangle$ is obtained by the Bethe-Bloch fit to the mean of the $\mathrm{d}E/\mathrm{d}x$ distributions of clean samples of different particle species. An example of such a fit is shown in Figure 3.9. Although the Bethe-Bloch equation for electrons differs from the one for heavier particles, the specific energy loss in the ALICE TPC can be described by a same function as in the case of other particle species. Therefore, the fitting function is common to all particle species. Various PID strategies are adopted in order to select the clean samples. In the regions, where the TPC separation of a definite particle species from other species is large, the TPC PID only selection is sufficient. In the regions, where the separation decreases, the TOF PID can be used in addition to the TPC PID in order to improve the purity of samples. Clean samples are selected as well by topological identification of V^0 candidate decays or conversions.

Mean energy loss $\langle \mathrm{d}E/\mathrm{d}x \rangle$ for different particle species is corrected before TPC $n\sigma_{TPC,i}$ calculation considering the deviations from the Bethe-Bloch fit at low momenta and detector effects dependent on a track topology and event multiplicity. The resolution dependence on the number of cluster for PID is obtained from fits to the abundant clean proton samples. More details about the procedure can be found in [143].

3.6   Centrality determination

The centrality of a collision is a crucial property in studying strongly interacting matter in heavy-ion collisions as it is directly linked to the geometrical overlap of the colliding nuclei. The centrality of a heavy-ion collision is defined as the percentile of the total nuclear hadronic cross section of an A–A collision with the impact parameter b as is shown in Equation 1.1. Since the impact parameter b is not a measured quantity, the centrality definition in experiments is based on observables related to the nuclear overlap volume. In ALICE, the charged-particle multiplicity measured by the V0 detector is used because the signal amplitude in the V0 monotonously increases with the event centrality. The centrality is then defined as the percentile of the hadronic cross section above the threshold of the measured charged-particle multiplicity $N_{\mathrm{ch}}^{\mathrm{thr}}$ instead of the percentile above the impact parameter b:

$$c \approx \frac{1}{\sigma_{\mathrm{AA}}} \int_{N_{\mathrm{ch}}^{\mathrm{thr}}}^{\infty} \frac{\mathrm{d}\sigma_{\mathrm{AA}}}{\mathrm{d}N_{\mathrm{ch}}'} \mathrm{d}N_{\mathrm{ch}}'. \tag{3.4}$$
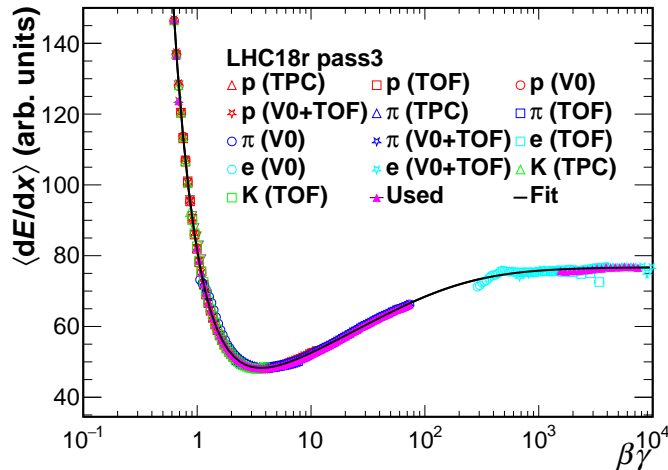
Figure 3.9: Bethe-Bloch fit to the means of the TPC dE/dx distributions of clean samples. The samples of different particle species are obtained using various detector PID signals or decay products of clean V^0 samples. (Figure by Michael Ciupek.)

More details can be found in [144, 20]. In principle, the distribution of the V0 amplitude itself shown in Figure 3.10 would directly serve for the centrality determination if there were only hadronic events triggered and their trigger efficiency is 100%. In such case, the centrality of an event would be simply the integral of the normalized V0 amplitude distribution above the V0 amplitude of the event. However, in the region corresponding to the most peripheral events, it is not feasible to experimentally obtain the V0 amplitude distribution of only hadronic events with a sufficient precision. The measured distribution is largely contaminated by electromagnetic (EM) interaction background. Moreover, the trigger efficiency drops below 100% in this region. This complicates the determination of the percentile corresponding to the measured V0 amplitude. Therefore, the experimentally obtained distribution is fitted in the interval where the contamination is negligible with the Monte Carlo Glauber model [145, 20]. The integral of the normalized Glauber fit function is than later used to deduce the centrality of events.

The Glauber Monte Carlo is a simulation of heavy ion-collisions and their charged-particle multiplicities. In the first step, the positions of nucleons within nuclei is randomly generated according to the nuclear density function approximated by the Fermi distribution (also referred to as modified Wood-Saxon distribution), which has for spherical nuclei following shape:

$$\rho(r) = \rho_0 \frac{1}{1 + \exp\left(\frac{r-R}{a}\right)}, \tag{3.5}$$

where ρ_0 is the nucleon density in the center of the nucleus, R is the nuclear radius and a the skin depth. The nucleon density defining the overall normalization is not relevant for the simulation. The parameters R and a are taken from low energy electron-nucleus scattering measurements [146].

In the second step, the collisions of two nuclei are simulated. The impact parameter is randomly sampled from the geometrical distribution $dP/db \sim b$. The nucleus-nucleus collision is approximated as a superposition of binary nucleon-nucleon collisions. Two nucleons are considered to collide when the distance d of their centers fulfills $d < \sqrt{\sigma_{NN}^{inel}/\pi}$, where σ_{NN}^{inel} is the inelastic nucleon-nucleon cross section taken from the interpolation of existing $p\bar{p}$ and pp measurements of collider and cosmic ray experiments [147]. Nucleons undergoing more than one collision are considered to be unaffected by preceding collisions. At this stage of the simulation, the number of binary nucleon-nucleon collisions N_{coll} and the number of participants N_{part} in a single simulated event can be obtained simply by counting of the binary collisions and the nucleons suffering them.

Afterwards, N_{coll} is linked to the charged-particle multiplicity observed in the V0 detector. The nucleon-nucleon interactions emitting charged particles are considered to be independent. Particle production is divided into two components—the soft and the hard sources. The sources are referred to as "ancestors" and their abundance is expressed by $N_{\mathrm{anc}} = f \times N_{\mathrm{part}} + (1-f) \times N_{\mathrm{coll}}$. The number of soft sources is assumed to be proportional to N_{part}, whereas the number of hard interactions to N_{coll}. The probability to obtain n hits in the V0 detector per one ancestor is approximated by the Negative Binomial Distribution (NBD). This assumption is based on measurements of the charged-particle multiplicity in pp and p$\bar{\mathrm{p}}$ collisions [148]. It was observed that the measurements are well described by the NBD over a wide rapidity range. The V0 amplitude, which is proportional to the charged-particle multiplicity, is simulated for different values of NBD parameters and for the ancestor parameter f. The MC Glauber amplitude is fitted to the observed distribution as is shown in Figure 3.10 in the range with high purity of hadronic events and an event selection efficiency of 100%. The optimal parameters are determined by minimizing the χ^2 difference between the simulated and the experimentally obtained curve.
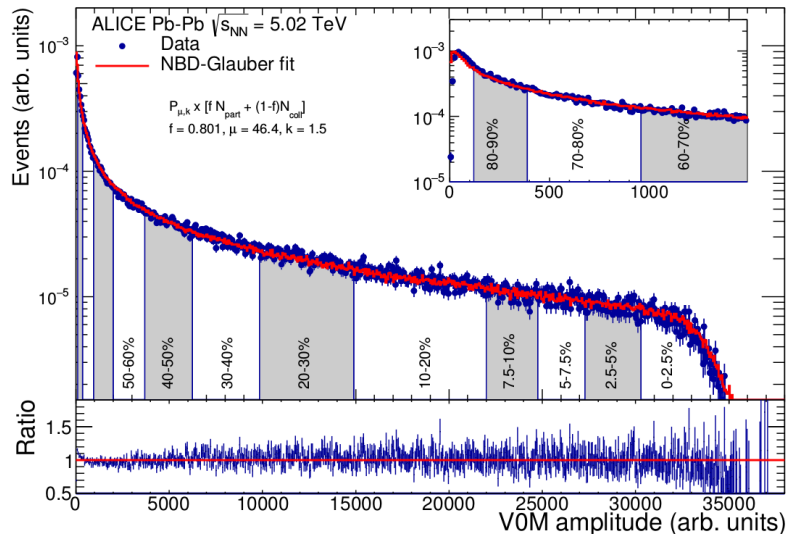
Figure 3.10: The distribution of amplitudes from the V0 detector for Pb–Pb collisions at $\sqrt{s_{\mathrm{NN}}} = 5.02$ TeV. The red line represents the fit of data points by the Glauber model. The ratio of the data to the fit is shown in the lower panel of the figure. A zoom into the interval corresponding to the peripheral events is shown in the right top corner.

As described above, this method allows to find experimentally the centrality of events by the integration of the Glauber fit function and consequently also define centrality classes by boundaries in the V0 amplitude. Furthermore, it connects experimental observables with geometrical quantities such as $\langle N_{\mathrm{coll}} \rangle$ and $\langle N_{\mathrm{part}} \rangle$ allowing to compare theoretical predictions and experimental results obtained within centrality classes. The average values of the nuclear overlap function $\langle T_{\mathrm{PbPb}} \rangle$ and the average number of number of participants $\langle N_{\mathrm{part}} \rangle$ used in this work are listed in Table 3.1. T_{PbPb} is obtained from N_{coll} as explained earlier in Subsection 1.2.3.

There are further methods of defining centrality in ALICE [144], which are used to cross check the approach described above. The first one is based on the simulation of hadronic and EM interactions and subtracting the EM fraction from the measured V0 amplitude distribution. Afterwards, the obtained distribution is corrected for the efficiency of the hadronic event selection. In the second method, instead of measuring charged particles origination from collisions of participants, the centrality is deduced from the amplitudes in the ZDC detectors placed close to the beam pipe. The two ZDC sets placed on opposite sides of the interaction point contain each ZN measuring the energy of spectator neutrons and ZP measuring protons. However, the ZDC amplitude obtained by adding signals of protons and neutrons does not monotonously increase with the number of nuclear

Centrality (%)	0–5	5–10	10–20	20–30	30–40	40–50	50–70	70–90	0–10	30–50
$\langle T_{\mathrm{PbPb}} \rangle$ (mb^{-1})	26.080	20.440	14.400	8.767	5.086	2.747	0.976	0.1611	23.260	3.916
$\langle T_{\mathrm{PbPb}} \rangle$ error (mb^{-1})	0.176	0.166	0.126	0.101	0.081	0.048	0.016	0.0012	0.168	0.047
$\langle T_{\mathrm{PbPb}} \rangle$ error (%)	0.7	0.8	0.9	1.2	1.6	1.7	1.6	0.7	0.7	1.2
$\langle N_{\mathrm{part}} \rangle$	383.40	331.20	262.00	187.90	130.80	87.14	42.66	11.34	357.30	107.47
$\langle N_{\mathrm{part}} \rangle$ error	0.57	1.03	1.15	1.34	1.33	0.93	0.72	0.19	0.75	1.17
$\langle N_{\mathrm{part}} \rangle$ error (%)	0.1	0.3	0.4	0.7	1.0	1.1	1.7	1.7	0.2	1.1

Table 3.1: Average number of participants and nuclear overlap function $\langle T_{\mathrm{PbPb}} \rangle$ for Pb–Pb collisions at $\sqrt{s} = 5.02$ TeV for different centrality classes. The values are taken from [20].

spectators due to the light nuclei fragment formation. The fragments are not detected by the ZDC detector because their charge to mass ratio is similar to that of the colliding nuclei allowing them to continue in the beam pipe. The fragment formation is more probable for peripheral events with more spectators. Therefore, ZDC signals from more central events are distinguished from peripheral events using amplitude measured by the electromagnetic calorimeter ZEM.

3.7 ALICE upgrade

The ALICE detector has underwent a major upgrade in last years during Long Shutdown 2 of the LHC accelerator. It will allow to study probes of the QGP that have not been accessible up to now and currently accessible probes with a higher precision. Minimum-bias samples 50–100 larger in comparison to Run 2 will be collected due to an increased collision rate of 50 kHz employing the full LHC luminosity. Furthermore, tracking performance of the Central Barrel will be improved due to increased granularity and reduction of material budget of the upgraded ITS. Moreover, secondary vertices can be newly reconstructed also at forward rapidity. These improvements will allow for example to extend high precision measurements of heavy-flavor production at midrapidity down to $p_{\mathrm{T}} = 0$ GeV/c, which is unique at the LHC. Prompt and non-prompt components will be better separated at midrapidity and their separation is newly possible also at forward rapidity.

The upgraded ITS [149] consists of seven layers of Monolithic Active Pixel Sensors with smaller size (25 μm x 25 μm) in comparison to the previous ITS. Since the beam pipe diameter is reduced, inner layers of the ITS are placed closer to the interaction point starting with the first layer with radius 2.3 cm. The material thickness decreased in order to reduce multiple scattering. These changes will enable to pin down better particle trajectories, which is crucial for precise reconstruction of the secondary vertices. The resolution of trajectory impact parameters will be better than 40 μm for transverse momenta above 0.5 GeV/c.

At forward rapidity, the reconstruction of particle trajectories was limited by the fact that the Muon Spectrometer was placed behind the hadron absorber with respect to the interaction point. The new Muon Forward Tracker was installed in front of the absorber allowing the separation of primary tracks and tracks from displaced secondary decays.

The TPC readout chambers are upgraded [150] with novel Gas Electron Multiplier (GEM) technology. The GEM foils simultaneously multiply electrons and collect ions, which allows continuous readout. An electron microscope photograph of a GEM foil is shown in the left of Figure 3.11. A simulation of multiplication of two electrons passing through a GEM hole is shown on the right of the same figure. Four layers of foils employing this technology are placed in the readout chambers. Each foil is made of an inner insulator layer covered with conducting copper coating on each side. Voltages with difference of 300–400 V are applied on each copper layer generating strong electric fields in round holes pitched into the foil. The field in the holes is sufficient to multiply electrons. Ions are then collected partially on one side of the same foil or by neighboring foils. The ion back-flow is reduced to an acceptable level below 1% with the 4-GEM arrangement limiting distortions to less than 10 cm in the majority of the TPC drift volume. The TPC readout rate has been limited up to now to approximately 3.5 kHz because electrons drift to the readout chambers up to approximately
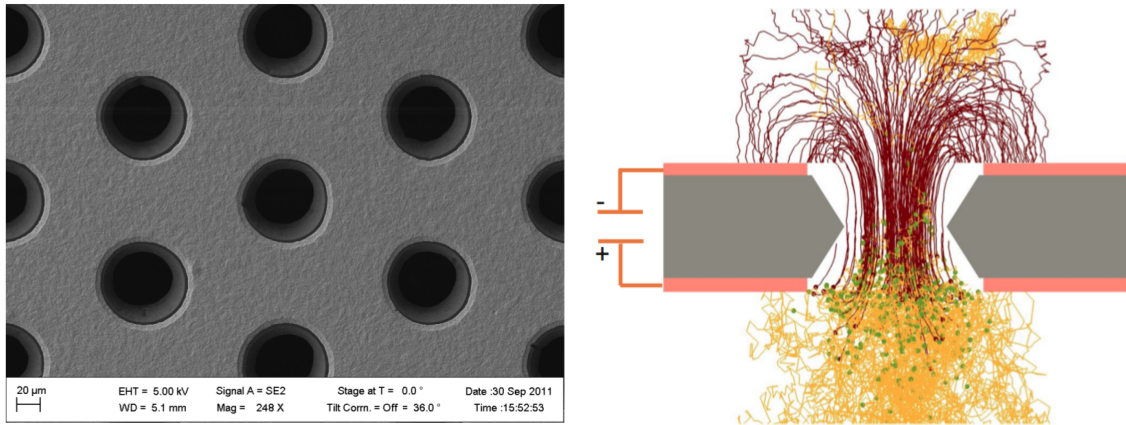
Figure 3.11: Left: An electron microscope photograph of a GEM foil. (Figure is taken from [150].) Right: Simulation of charge dynamics of two electrons passing through a GEM hole. Electron paths are shown as yellow lines, whereas ions as dark red lines. Placed of ionization are marked with spots. (Figure is taken from [151].)

90 μs and the gating grid had to be closed for 180 μs to collect slowly drifting ions. For the upgrade, the gating grid could be removed since ion back-flow is reduced sufficiently by the GEM technology.

Measurement of inclusive J/ψ production in Pb–Pb collisions at $\sqrt{s_{\mathrm{NN}}} = 5.02$ TeV

This thesis presents the analysis of the inclusive J/ψ production in Pb–Pb collisions recorded by the ALICE Collaboration. The measurement of the J/ψ production yields is carried out as a function of the collision centrality and J/ψ transverse momentum for centralities with the largest collected samples with the full data available at $\sqrt{s_{\mathrm{NN}}} = 5.02$ TeV. The main analysis steps from the event selection to the studies of the J/ψ production systematic uncertainties are presented in this chapter.

4.1 Observables

The p_{T}-integrated J/ψ production yield in Pb–Pb collisions is obtained as follows:

$$\frac{\mathrm{d}N_{\mathrm{AA}}}{\mathrm{d}y} = \frac{N_{\mathrm{AA}}^{\mathrm{rawJ}/\psi}}{N_{\mathrm{ev}} \cdot \mathrm{BR}_{\mathrm{J}/\psi \to \mathrm{ee}} \cdot (A \times \epsilon) \cdot \Delta y}. \tag{4.1}$$

The p_{T}-differential J/ψ production yield can be calculated by:

$$\frac{\mathrm{d}^2 N}{\mathrm{d}y\mathrm{d}p_{\mathrm{T}}} = \frac{N_{\mathrm{AA}}^{\mathrm{rawJ}/\psi}}{N_{\mathrm{ev}} \cdot \mathrm{BR}_{\mathrm{J}/\psi \to \mathrm{ee}} \cdot (A \times \epsilon) \cdot \Delta y \cdot \Delta p_{\mathrm{T}}}. \tag{4.2}$$

$N_{\mathrm{AA}}^{\mathrm{rawJ}/\psi}$ is the number of reconstructed J/ψ mesons in a desired centrality class, rapidity interval and p_{T} interval. N_{ev} is the number of events used for the J/ψ signal reconstruction. The signal extraction is described in detail in Section 4.4. $N_{\mathrm{AA}}^{\mathrm{rawJ}/\psi}$ is corrected for the acceptance times efficiency $A \times \epsilon$, which is presented in Section 4.5. The branching ratio of the J/ψ dielectron decay channel $\mathrm{BR}_{\mathrm{J}/\psi \to \mathrm{ee}}$ in the equation translates the corrected number of the J/ψ mesons decaying via the dielectron decay channel to the total number of J/ψ mesons. The branching ratio is equal to $(5.971 \pm 0.032)\%$ [9]. This factor is in the studies presented in this chapter for the simplicity omitted from the equation.

The inclusive J/ψ nuclear modification is obtained from the J/ψ production yield in Pb–Pb collisions in Equation 4.1 as follows:

$$R_{\mathrm{AA}} = \frac{\mathrm{d}N_{\mathrm{AA}}/\mathrm{d}y}{\langle T_{\mathrm{AA}} \rangle \mathrm{d}\sigma_{\mathrm{pp}}/\mathrm{d}y}. \tag{4.3}$$

The p_{T}-differential inclusive J/ψ R_{AA} can be obtained from the yield in Equation 4.2:

$$R_{\mathrm{AA}} = \frac{\mathrm{d}^2 N_{\mathrm{AA}}/(\mathrm{d}y\mathrm{d}p_{\mathrm{T}})}{\langle T_{\mathrm{AA}} \rangle \mathrm{d}^2 \sigma_{\mathrm{pp}}/(\mathrm{d}y\mathrm{d}p_{\mathrm{T}})}. \tag{4.4}$$

The average nuclear overlap function in Pb–Pb collisions $\langle T_{\mathrm{AA}} \rangle$ is discussed earlier in Subsection 3.6. The p_{T}-integrated and p_{T}-differential inclusive J/ψ cross section in pp collisions represents the

reference for the inclusive J/ψ measurement in Pb–Pb collisions. Details about the pp reference are given in Section 4.8.

A first measurement of the inclusive J/ψ production yield and nuclear modification factor R_{AA} at midrapidity in Pb–Pb collisions at $\sqrt{s_{NN}} = 5.02$ TeV is already published [152]. However, it employs only the data sample collected in the year 2015. A larger data set was recorded in the year 2018. The combination of the collected data samples allows to study the inclusive J/ψ production yield and R_{AA} as a function of centrality and as a function of p_T in finer intervals compared to the published results [152]. This is achieved while keeping the precision of the measurement at a similar level in full examined centrality and p_T regions.

Improvements of the new measurement presented in this work do not follow only from the larger used data sample but also from developments of the data analysis methods. In particular, the precision of the measurement is improved by a new data-driven approach used for the calculation of the J/ψ efficiency of PID selections. More details about this and other improvements are given in the corresponding sections of this chapter.

4.2 Data sample

The results presented in this work are obtained by the analysis of Pb–Pb collisions collected at the center-of-mass energy per nucleon-nucleon pair $\sqrt{s_{NN}}$ equal to 5.02 TeV in the years 2015 and 2018. ALICE recorded more than $4 \cdot 10^8$ events reading out the detectors at midrapidity relevant for this analysis. More than about $2.5 \cdot 10^8$ of them are so-called minimum bias (MB) events triggered by a coincidence of signals in both V0 detectors. A threshold on a sum of V0 signals in the V0 detectors discussed in Subsection 3.3.5 served for centrality triggering. The centrality determination is described in Subsection 3.6. The centrality trigger selected additional events in the centrality classes 0–10% and 30–50% on top of these triggered by the MB trigger. The events in centrality class 0–10% are below referred to as the most central events, whereas the events in the centrality class 30–50% are referred to as the semi-central events. The centrality and MB triggers allowed to collect approximately two times as much semi-central events per a centrality window than the MB trigger alone in the centrality ranges from 10 to 30% and from 50 to 90% and four times as much statistics for the most central events.

The number of events relevant for the J/ψ analysis at midrapidity collected in both years is approximately same for the centrality classes 10–30% and 50–90%. The abundance of all collected events is about four times as large compared to the 2015 data set alone in the centrality class 30–50%. The size of full collected data sample for the centrality class 0–10% is even eight times as large as the size of the 2015 data sample.

Bunches of nuclei are at the LHC arranged in trains. There are approximately 20 to 50 bunches per one train. The spacing between bunches within the trains is around 100 and 150 ns. The LHC15o data set from the year 2015 and two 2018 data sets LHC18q and LHC18r are collected at an interaction rate f_{INT} between 1 and 7.5 kHz. f_{INT} was ramping up during the data taking of the LHC15o data set. It varied in the case of the LHC18r data set and was leveled at 7.5 kHz while collecting the LHC18q data set. The probability of an inelastic hadronic collision occurring within one bunch crossing is around 10^{-3}. Therefore, the fraction of so-called in-bunch pile-up events—recorded events with more than one interaction in the triggered bunch crossing—within the collected sample is also only around 1‰. Moreover, the ITS detector is capable of resolving possible pile-up vertices and tracks from one of the events are therefore not used in the analysis. However, the fraction of recorded events that contains an additional interaction seen by the TPC within its drift time is sizable due to the large interaction rate during the data taking.

The out-of-bunch pile-up can bias the TPC dE/dx and consequently the PID. The read-out time window for signals in the TPC that are associated to the triggered interaction is distracted by the electron drift time of around 90 μs from the central TPC electrode to the read-out chambers. This means that tracks from an interaction happening within this time range contribute to the reconstructed event. A bias can be caused by a pile-up interaction happening not only after the triggered one, but also before it. The extent to which the TPC PID is affected depends on the time

of the pile-up interaction with respect to the triggered interaction and multiplicity arising from the interaction that is not triggered. The correction of the TPC dE/dx distribution in the pile-up events of the 2018 data sets has been an object of extensive efforts.

4.2.1 Event classification and selection

Only events selected by MB and centrality triggers provided by the V0 detectors are analyzed for purposes of this work. Beam-gas interactions are already rejected by requiring a coincidence in the V0 detectors as explained in Subsection 3.3.5. The most peripheral events with centrality above 90 % are excluded due to a trigger efficiency decrease and the potential contamination from electromagnetic interactions. Furthermore, selected events are required to have a primary vertex with a vertex z position fulfilling $|V_z| < 10$ cm. Events with $|V_z|$ out of this region suffer from decreased detector acceptance. The vertex z position distribution of events after the selections described in this paragraph is shown in Figure 4.1.
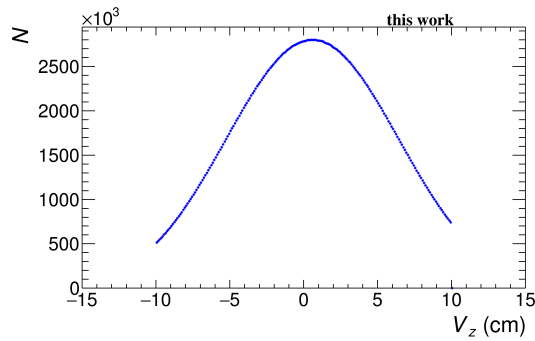
Figure 4.1: The distribution of vertex z position after applying the selection $|V_z| < 10$ cm.

The events are classified based on the correlation between the number of TPC clusters and the sum of SSD and SDD clusters. Whereas the number of TPC clusters in one event can be largely affected by second interactions with spacing of order of tens of μs with respect to the triggered event, the number of clusters of the faster SSD and SDD detectors remains unbiased. Events with a single interaction or these little affected by the second interaction follow a narrow correlation between the sum of SSD and SDD clusters and the number of TPC clusters. These events correspond to the bright yellow regions in Figure 4.2 left from the red curve representing the boundary between rejected and accepted events. On the other hand, the number of TPC clusters in events with more interactions manifests an increase with respect to the values typical for events with a single interaction.
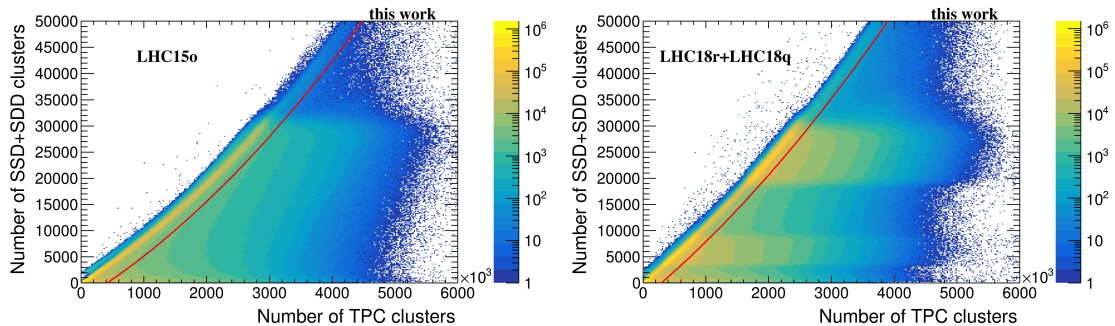
Figure 4.2: The sum of the numbers of SSD and SDD clusters versus the number of TPC clusters. The red line corresponds to the boarder between events that are accepted and rejected events affected by the pile-up. Left: 2015 data set LHC15o. Right: 2018 data sets LHC18q and LHC18r.

The V0 centrality distribution of events after applying all selection criteria is shown in Figure 4.3. The distribution is flat with a percent precision. It guarantees that the measurement within one centrality class is equally represented by events with different centralities within corresponding centrality interval. The sample of collected events in the years 2015 and 2018 after the event selections corresponds to the integrated luminosity of 105 μb^{-1} for the centrality class 0–10%, 52 μb^{-1} for the centrality class 30–50% and 24 μb^{-1} for the centrality classes 10–30% and 50–90%.
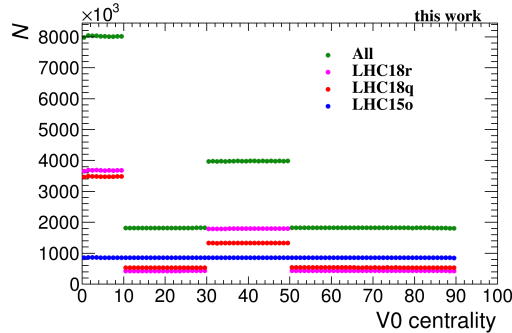
Figure 4.3: The centrality distribution for selected events.

4.2.2 Monte Carlo simulation

J/ψ mesons decaying via the di-electron decay channel $J/\psi \rightarrow e^+e^-$ in collisions recorded by the ALICE detector are not reconstructed in every case. Initially, an electron and a positron from the J/ψ decay fall either into or out of the detector acceptance and kinematic regions defined by acceptance selection criteria. The fraction of J/ψ with decay products passing this step is called acceptance. Only a part of tracks within acceptance passes tracking selection criteria and PID selection criteria used to ensure good quality of tracks for the J/ψ signal reconstruction and suppression of a background. The efficiencies of these two steps are referred to as the tracking and the PID efficiency. Finally, the reconstructed J/ψ signal is counted only within constrained invariant mass interval. The acceptance, the tracking and the mass window efficiency are obtained using a dedicated Monte Carlo (MC) simulation taking into account the detector setup and the data taking conditions.

The HIJING [153] Monte Carlo model developed to study high-energy hadronic collisions serves for the generation of Pb–Pb collisions within the ALICE framework. In total, $1.1 \cdot 10^6$ events are used for the dedicated J/ψ MC simulation LHC16j1 of the LHC15o data set. The simulation for the J/ψ measurement in the LHC18r and LHC18q data sets comprises $16.3 \cdot 10^6$ of events. This simulation called LHC20g5 is due to centrality triggers enhancing the most central and semi-central event samples subdivided into four simulations LHC20g5a, LHC20g5b, LHC20g5c and LHC20g5d corresponding to the different centrality classes 0–10 %, 10–30 %, 30–50 % and 50–90 %.

J/ψ mesons are scarcely produced in Pb–Pb collisions. Therefore, several J/ψ mesons are injected by PYTHIA 6 [154] into every event generated by the HIJING simulation. This approach allows to study the J/ψ acceptance and efficiencies with a good statistical precision. The distributions of J/ψ transverse momentum p_T and rapidity for both simulations are shown in Figure 4.4. The distributions for the LHC16j1 simulation are taken from the interpolation of the inclusive J/ψ measurements in pp collisions carried out by Tevatron, PHENIX and LHC [155]. In addition, the J/ψ meson abundance is enhanced by a flat distribution at low and high transverse momentum below 0.5 GeV/c and above 6 GeV/c important for studies of the J/ψ photoproduction and the high-p_T J/ψ. A different strategy is adopted for the LHC20g5 simulation with approximately 15 times higher amount of events. The natural p_T distribution is sampled to generate transverse momenta of J/ψ mesons. The natural shape is updated by the fit of the preliminary J/ψ p_T-differential spectra in the most central Pb–Pb collisions in the LHC18r and LHC18q data sets—in the other words, by the shape obtained using the preliminary version of this work.
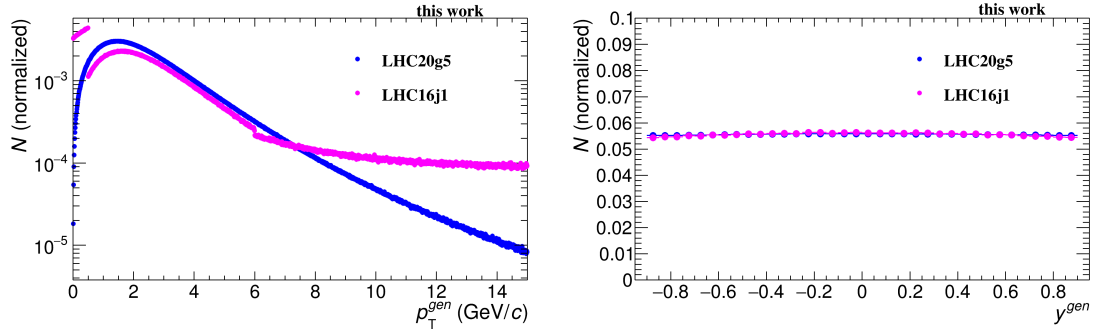
Figure 4.4: The transverse momentum and rapidity distributions of J/ψ generated by the MC simulations.

Prompt and non-prompt J/ψ mesons are injected with the ratio $7:3$. Non-prompt J/ψ mesons originate from decays of beauty quarks and anti-quarks produced in b$\bar{\text{b}}$ pairs. All J/ψ mesons are forced to decay via the dielectron decay channel by the EvtGen [156] package. The PHOTOS algorithm [157] is implemented in the EvtGen in order to simulate the final state radiation. The simulation of the fraction of the radiative J/ψ decays J/$\psi \rightarrow$ e$^+$e$^-\gamma$ is especially important for a calculation of the mass window efficiency as an invariant mass shape of the radiative decays has a longer tail towards low values than in the case of the non-radiative decays. Finally, the propagation of particles through the detector is simulated by the GEANT 3 [158]. This detector description and simulation tool includes the arrangement of all detector systems, the distribution of their matter, the propagation of particles through the detector including all important physics processed and the detector response. The data taking conditions such as a magnetic field polarity or maps of dead detector zones are considered in the simulation.

4.3 Track selection

J/ψ electron candidates are selected in three steps. Firstly, they have to pass acceptance and tracking selection criteria. Afterwards, contamination from pions and protons is suppressed using the TPC PID. These steps will be described in this section.

4.3.1 Tracking and acceptance selections

Acceptance and selection criteria are applied in order to select track candidates with a good quality and suppress background. These selection criteria are listed in Table 4.1. The central barrel tracking and some of the tracking variables are discussed in Section 3.4.

The acceptance selections are the selections on pseudorapidity η and transverse momentum p_T. The selection criterion $|\eta| < 0.9$ rejects particles escaping the TPC acceptance before they reach the TPC outer radius. An exclusion of tracks with p_T below 1 GeV/c suppresses background from other sources of electrons with lower typical transverse momenta such us photon conversions or Dalitz decays.

The TPC refit is a crucial condition for selection of tracks with a good quality of tracking and PID. The J/ψ efficiency is due to this requirement reduced approximately by 20%. All of the other applied TPC related selection criteria are significantly more efficient. Pions and kaons weakly decay in the TPC active volume to one neutral and one charged decay product. They can be identified by finding TPC trajectories with small-angle kinks. They are rejected for the purpose of this work. The selections on numbers of PID clusters, crossed TPC rows and crossed rows over the number of findable clusters assure that tracks with sparse space points or large continuous missing areas along their trajectory are excluded from this analysis. A typical example of such tracks are tracks with larger path length through or close to the TPC chamber boundaries. Furthermore, selection criterion

Variable	Selection criterion
p_{T}	$\geq 1\ \mathrm{GeV}/c$
$|\eta|$	≤ 0.9
TPC refit	required
Rejection of kink daughters	required
Number of PID clusters	≥ 50
Number of TPC crossed rows	≥ 70
Crossed rows/findable clusters	≥ 0.8
TPC χ^2/number of TPC clusters	≤ 4.0 for LHC15o
	≤ 2.5 for LHC18r and LHC18q
ITS refit	required
Number of hits in SPD	≥ 1
ITS χ^2/number of ITS clusters	≤ 36
$|\mathrm{DCA}_{xy}|$	≤ 1 cm
$|\mathrm{DCA}_z|$	≤ 3 cm

Table 4.1: Tracking selection criteria.

on the TPC χ^2 of the track fit per cluster is applied in order to exclude tracks more affected by the TPC space charge distortions. The TPC space charge distortions are discussed in Subsection 3.4.1. This selection criterion differs for 2015 and 2018 data sets since a distribution of the TPC χ^2 per cluster changed due to a modification in an error parametrization of TPC clusters.

The ITS refit and requirement on the track to have at least one hit in two innermost ITS layers improves the momentum resolution and rejects tracks from non-triggered interactions in out-of-bunch pile-up events. In addition to that, requirement on at least one hit in the SPD rejects electrons originating from photon conversions in the detector material at larger radius than the radius of a pixel layer with the first SPD hit. However, these advantages come at the prize of a J/ψ efficiency loss. The ITS refit selection has in the MC simulation the J/ψ efficiency about 90% when applying only the TPC refit criterion first. This efficiency is referred to as the ITS-TPC matching efficiency and is investigated in the data and MC simulation on the track level within common efforts of the ALICE Collaboration. A discrepancy between the values in the MC simulation and the data leads to sizable systematic uncertainty of the J/ψ measurement discussed later in Subsection 4.6.1. Similarly as in the case of the ITS refit selection, the J/ψ efficiency is due to the SPD any requirement reduced by approximately 10% of the efficiency value. The ITS χ^2 per cluster is selected to be below 36. Finally, the distance of the closest approach (DCA) of tracks to the primary vertex is required to be within ± 3 cm in the z direction and within ± 1 cm in the xy plane. The selection in the z direction reduced out-of-bunch pile-up tracks remaining after the already mentioned selection criteria, whereas the selection $|\mathrm{DCA}_{xy}| \leq 1$ cm helps to suppress background from secondaries. At the same time, the selection on DCA_{xy} and DCA_z are wide enough to include tracks from the non-prompt J/ψ decays. The efficiency of the DCA selections is very close to 100 %.

Examples of the tracking variable distributions are compared for selected electron candidates in the data and the J/ψ enhanced MC simulation using only decay products of J/ψ mesons. These distributions can be found in Figure 4.5. The comparisons are done applying all selection criteria on electron candidates including PID selection criteria mentioned in next Subsection 4.3.2. These comparisons are useful for studying mismatches between the data and the MC that could cause bias in the efficiencies obtained using the MC simulation. However, only J/ψ decays are considered in the MC sample, whereas track sample passing selection criteria in the data consists of a various mixture of sources such as secondary electrons from photon conversions and hadrons. This is especially pronounced in the distribution of DCA_{xy}.
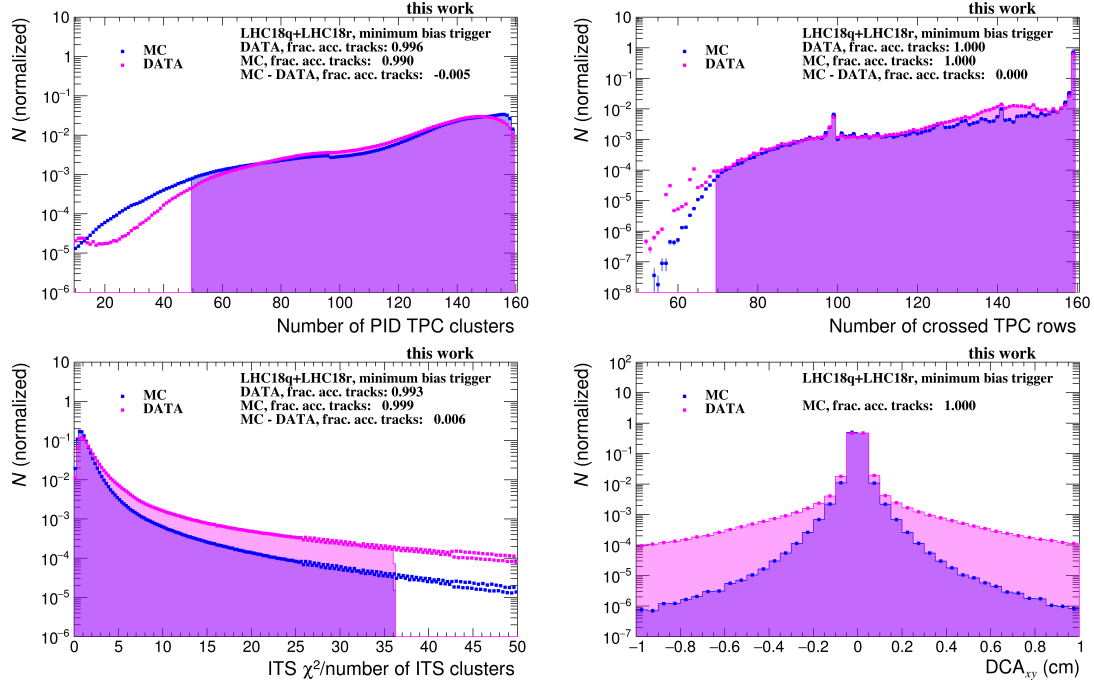
Figure 4.5: Distributions of different tracking variables in MB collisions with centrality 0–90% and fractions of accepted tracks in the data, MC and their difference. The shaded areas correspond to accepted tracks.

4.3.2 Electron identification

The particle identification belongs to the most delicate procedures in this work. It is based on the energy loss dE/dx in the TPC and its distance from hypotheses of different particle species i expressed in the number of standard deviations $n\sigma_i$. The energy loss in the TPC is discussed in Subsection 3.5.2, the procedure of $n\sigma_i$ calculation in Subsection 3.5.3. Electrons with momentum above 1 GeV/c are highly relativistic, therefore their specific energy loss in the TPC is almost constant. However, this is not the case for heavier particle species. The TPC dE/dx signal of abundant protons crosses the typical electron dE/dx signal close to momentum of 1 GeV/c. The signal of pions approaches the dE/dx typical for electrons towards high momentum. Since electrons are rare relative to pions and protons, tracks with the TPC dE/dx close to pion and proton hypotheses are excluded from the analysis. This approach reduces a hadron contamination in the candidate sample and improves J/ψ signal significance at the cost of J/ψ efficiency loss. The particle identification criteria used in this work are summarized in Table 4.2. The selection criterion $|n\sigma_e| < 3$ includes vast majority of electrons. On the other hand, the pion and proton exclusions $n\sigma_\pi > 3.5$ and $n\sigma_p > 3.5$ cause a decrease of the J/ψ efficiency around 45 % in the most central events. The PID efficiency and its calculation are described in Subsection 4.5.3.

Variable	Selection criterion
$|n\sigma_e|$	< 3
$n\sigma_p$	> 3.5
$n\sigma_\pi$	> 3.5

Table 4.2: Particle identification selection criteria.

PID selection of the candidate tracks is sensitive to imperfections of the $n\sigma_i$ calibration. They can cause higher hadron contamination and/or loss of efficiency with respect to the expectation from the
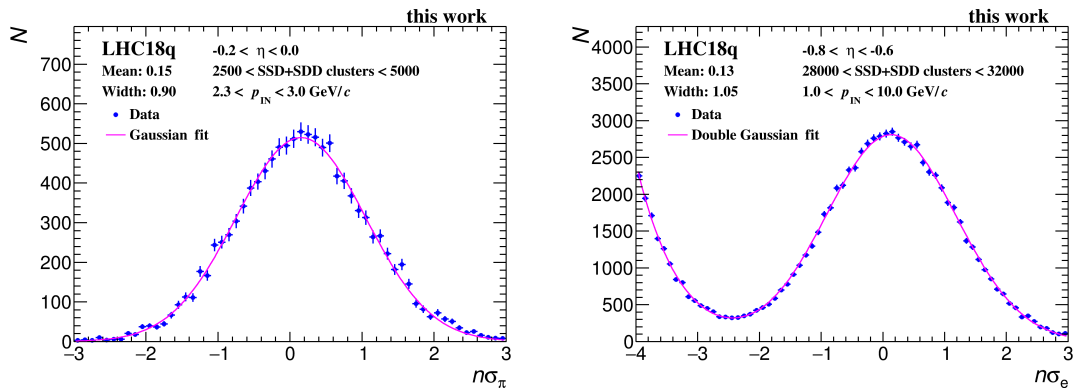
Figure 4.6: Left: Distribution of $n\sigma_\pi$ of clean pion sample fitted by Gaussian function. Right: Distribution of $n\sigma_e$ of relatively clean electron sample from photon conversions fitted by double Gaussian function to account for pion contamination.

data parametrization that is able to describe all calibration artefacts. Therefore, the distributions of $n\sigma_p$, $n\sigma_\pi$ and $n\sigma_e$ are studied using clean samples of electrons from photon conversions, pions from K_s^0 decays and protons from Λ decays. The photon conversions, the K_s^0 decays and the Λ decays are identified via dedicated algorithm finding V^0 topologies. More details about the V^0 identification algorithm can be found in [134].

$n\sigma_i$ distributions of clean proton and pion samples are fitted by a Gaussian function to obtain centroids and widths. In addition to a Gaussian function describing the electron distribution, an another Gaussian function is used to account for residual background in the sample of electrons. The residual background is dominated by pions from misidentified K_s^0 decays. The mean value of the Gaussian function of $n\sigma_i$ distribution of the particle species i (called centroid in the following) should be centered at zero and the width should be equal to unity. However, as can be seen on examples of the fitted pion and electron distributions in Figure 4.8, the widths are deviating from unity and the centroids from zero. Since the distributions vary according to track and event properties, the studies are carried out in intervals in multiple dimensions. Dependence on momentum in the inner wall of the TPC p_{IN} and pseudorapidity η are considered for the track properties. The momentum in the inner wall of the TPC p_{IN} is introduced Section 3.4. The number of SSD and SDD clusters is considered from the event properties since it reflects the occupancy of the TPC placed around the SDD and SDD detectors. Furthermore, the z position of so-called pile-up vertex v_z^{pileup} is studied in the case of LHC15o because this data set manifests a larger spread of events over v_z^{pileup} regions distant from values typical for non-pile-up events.

The v_z^{pileup} value reflects time of pile-up interaction with respect to the triggered event. It is determined as difference of the TPC A- and C-sides medians of z distance of pile-up contributors from the primary vertex divided by two. The distances are positive in the A-side and negative in the C-side. Pileup contributors are defined as tracks with $|DCA_{xy}| < 3$ cm and $|DCA_z| > 4$ cm. They are mainly tracks with the TPC refit only. This approach uses the fact that a drift distance of ionization electrons in the TPC in the time equal to the time difference between triggered and pile-up interaction is not negligible for out-of-bunch pile-up events. Therefore, space points of pile-up tracks appear to be reconstructed at different z positions than they normally would be if they originated from the triggered interaction. The z positions are shifted by $\Delta z = v_D \cdot \Delta t$, where v_D is the drift velocity of electrons in the TPC and Δt the time window between the triggered and pileup interactions. When the pile-up interaction happens in time before the triggered interaction, tracks in the A-side are reconstructed further away from the central electrode and have positive DCA_z. On the other hand, the tracks in C-side appear to have negative DCA_z. As a result, v_z^{pileup} is positive. It is opposite for pile-up interactions in time after the triggered event. v_z^{pileup} value typical for non-pile-up events is around zero.

50
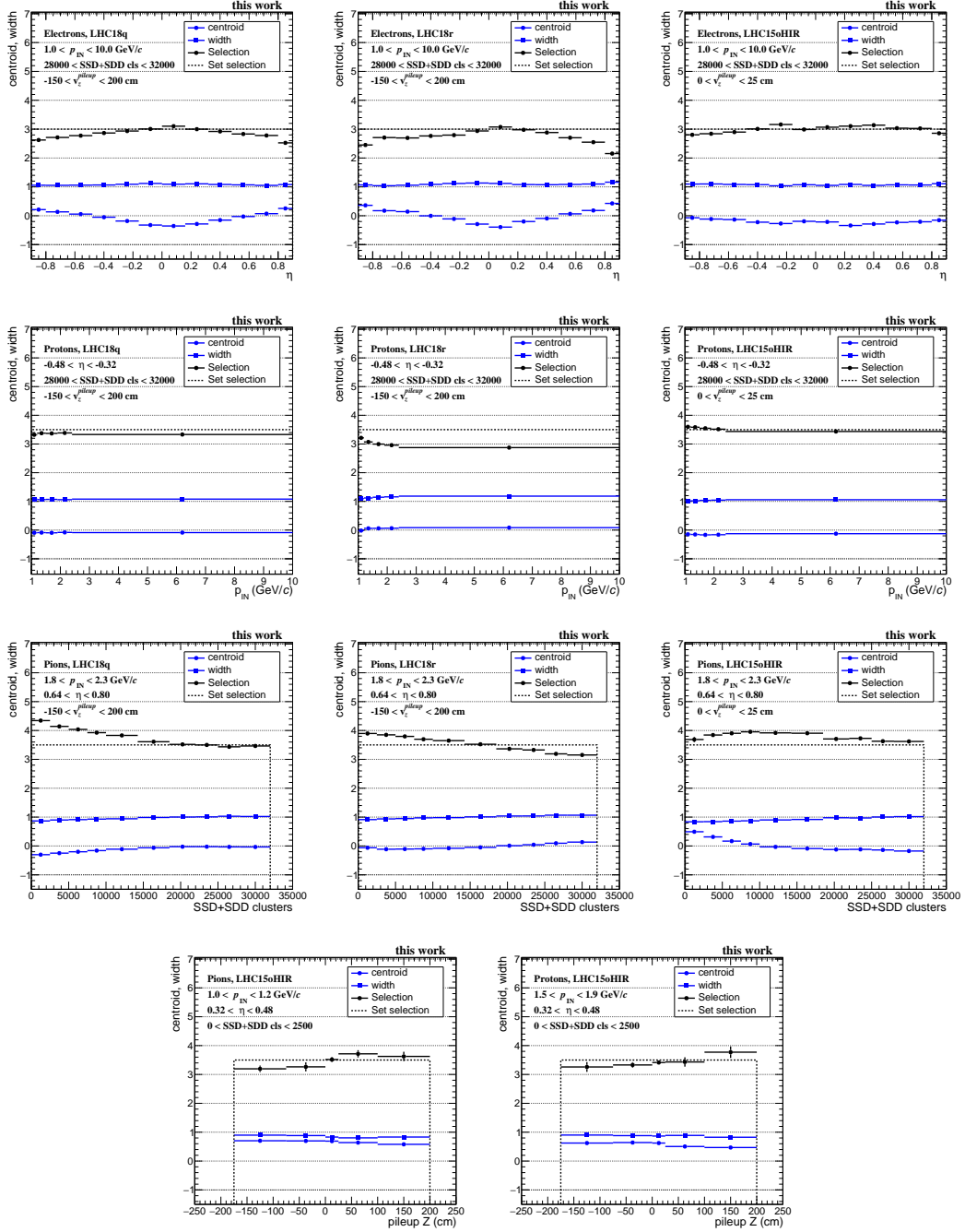
Figure 4.7: Examples of centroids and widths as functions of η, p_{IN}, the number of SSD+SDD clusters and v_z^{pileup} are shown in the blue color. Black dashed lines correspond to the set selections listed in Table 4.2. The black markers represent estimates of the effective selections that would be applied if no additional calibration of $n\sigma_i$ were applied.

Examples of centroids and widths as functions of η, p_{IN}, the number of SSD+SDD clusters and v_z^{pileup} are shown in Figure 4.7 in blue color. Especially, the centroids show relatively strong dependence on η and the number of SSD+SDD clusters. Different efficiencies would be effective than those expected based on the selection mentioned in Table 4.2 in case of no additional calibration.

The effective selection in terms of $n\sigma$ values that would be applied without any additional calibration can be quantified. It is dependent on width σ and centroid μ and can be calculated as $-1 \cdot \mu + 1/\sigma \cdot S$, where S is the set selection such as 3.5 for selection on $n\sigma_\pi$. σ and μ are the values from the fit to the clean sample. Estimates of selections that would be applied without post-calibration are shown in Figure 4.7 as the black points. Calibrated $n\sigma_i^{\mathrm{cal}}$ are obtained using the following equation:

$$n\sigma_i^{\mathrm{cal}}(\eta, p_{\mathrm{IN}}, N_{cls}^{\mathrm{SSD+SDD}}) = \frac{n\sigma_i(\eta, p_{\mathrm{IN}}, N_{cls}^{\mathrm{SSD+SDD}}) - \mu(\eta, p_{\mathrm{IN}}, N_{cls}^{\mathrm{SSD+SDD}})}{\sigma(\eta, p_{\mathrm{IN}}, N_{cls}^{\mathrm{SSD+SDD}})}. \qquad (4.5)$$

In the case of the LHC15o data set, there is also a dependence of the parameters of v_z^{pileup} considered as mentioned above.

$n\sigma_{\mathrm{e}}^{\mathrm{cal}}$ of selected tracks versus p_{IN} is shown in Figure 4.8. Tracks are excluded mostly by the proton rejection at low momentum. The pion rejection dominates at momenta above 2 GeV/c.
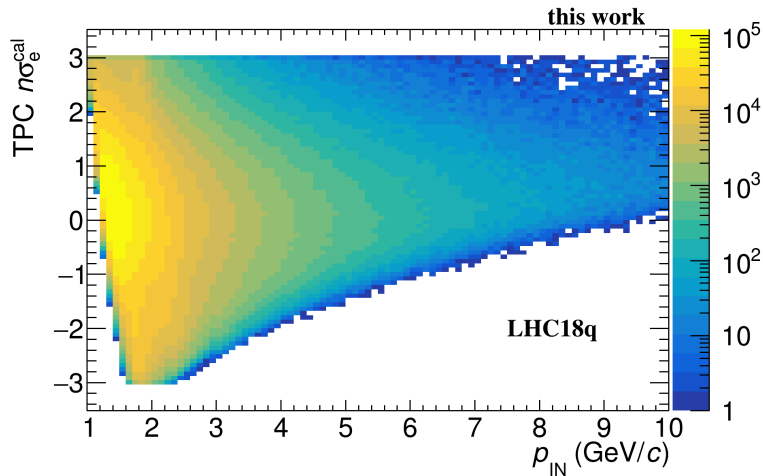
Figure 4.8: $n\sigma_{\mathrm{e}}^{\mathrm{cal}}$ versus momentum in the inner wall of the TPC after applying selection criteria on post-calibrated $n\sigma_{\mathrm{e}}$, $n\sigma_{\mathrm{p}}$ and $n\sigma_\pi$ for LHC18q data set.

The calibration procedure presented in this thesis is based on similar principles as the calibration in the publication using the 2015 data sample only [152] explained in mode details in [159]. However, the procedure presented in this work underwent significant changes in order to improve its performance. Firstly, $n\sigma_{\mathrm{e}}$ is the only from the three $n\sigma_i$ specie calibrated in the previous measurement. The calibration of $n\sigma_\pi$ and $n\sigma_{\mathrm{p}}$ is newly added. These two variables are crucial for rejection of protons and pions while keeping the efficiency of the PID selections as high as possible. Furthermore, the only considered dependence of the calibration parameters on event properties in the previous work is the dependence on the event centrality. The number of SSD+SDD clusters replaced this variable in this work since it directly reflects multiplicity at midrapidity that affects the TPC performance. In addition to that, the dependence on v_z^{pileup} is newly considered for the calibration of the 2015 data set as it is explained above. The choice of the considered dependences as well as the choice of the intervals in which the dependences are probed is carried out in this work. The latter provides balance between steepness of the calibration parameter changes and number of entries in the intervals, which affects a precision of the fits.

4.4   Signal extraction

When the electron and positron candidates are selected, they are paired in order to build J/ψ candidates. In the challenging conditions of Pb–Pb events with high multiplicity, a majority of the reconstructed unlike-sign pairs e$^+$e$^-$ consists of background pairs. On the track level, the

following sources contribute to the background: electrons from photon conversions, misidentified pions and protons,electrons from open-heavy-flavor decays and electrons from Dalitz decays. All of these sources contribute to combinatorial background made up by uncorrelated pairs. Smaller fraction of the total background is caused by decays of open-heavy flavor. The electrons from photon conversions are partially reduced by excluding conversion daughter candidates of pairs with invariant mass below 50 MeV/c. However, to keep efficiency of this selection at unity, the electron candidates are paired for this purpose only with tracks with $p_\mathrm{T} > 0.9$ GeV/c. This threshold is found by gradual changing of the selection on p_T from higher values to lower values as far as the extracted signal does not begin to drop.

The pairs with $0.15 < p_\mathrm{T} < 15$ GeV/c are included in the signal extraction. Pairs with $p_\mathrm{T} < 0.15$ GeV/c are excluded in order to reject J/ψ photoproduction as discussed in Subsection 2.4.5. The photoproduction contributes most to all produced J/ψ in the peripheral events. However, pairs with $p_\mathrm{T} < 0.15$ GeV/c are excluded for consistency in all centrality classes.The signal extraction is restricted to the pair rapidity region $|y| < 0.9$ due to acceptance selection on track pseudorapidity $|\eta| < 0.9$.

The invariant mass distribution of J/ψ candidates for different centrality bins is shown in the top plots of Figure 4.9 in red color. Only a very small fraction of all J/ψ candidates are J/ψ mesons with the exception of the peripheral events. The signal fit without previous estimation of the background would be complicated by the combination of large signal to background ratio and nontrivial background shapes. Thus, the background is modeled and subtracted before the fit of the J/ψ signal. The most common approaches for background estimation are like-sign and event mixing methods. The like-sign method is based on pairing of same-sign pairs within same events. However, the abundance of like-sign pairs is limited by the number of events as well as unlike-sign pairs are. Therefore, event mixing technique combining electrons and positrons from different events is chosen for the background description. The event mixing approach increases signal significance from $S/\sqrt{S + 2B}$ for the like-sign method to $S/\sqrt{S + B}$. In the event mixing method, events are mixed in groups large enough to suppress statistical uncertainties related to the number of mixed pairs. The shape of the invariant mass distribution from mixed events should resemble the shape of background of same event unlike-sign pairs as well as possible. Therefore, groups of events are chosen such that they contain only events similar in terms of centrality and event plane angle. Mixed-event pairs are scaled by weight obtained by dividing the number of like-sign pairs from same events by the same from mixed events. This procedure could be performed with unlike-sign pairs instead of like-sign pairs. However, the J/ψ invariant mass region would have to be excluded resulting in a lower statistical precision of the weight factor scaling down the number of pairs from mixed events to the level of pairs from same events. The event mixing background can describe only the combinatorial part of the background.

The background modeled by the event mixing is subtracted from the distribution of J/ψ candidates. Afterwards, the distribution is fitted by a function consisting of the J/ψ invariant mass shape from the MC simulation and a polynomial function for description of a residual background. The residual background consists partially of the correlated background and residual imperfections of the distribution of mixed-event pairs. The polynomial function has a degree as low as possible for a sufficient description. Higher order polynomial functions tend to fit fluctuations in the background. For all of the centrality classes in this work, a first order polynomial is sufficient when extracting signal for $0.15 < p_\mathrm{T} < 15$ GeV/c. Fitted J/ψ candidate distributions for p_T-integrated analysis after background subtraction is shown in the lower panels in Figure 4.9. The signal extraction is carried out also as a function of p_T for centrality classes 0–10% and 30–50% as shown in Figures 4.10 and 4.11. A first order polynomial is sufficient in all p_T intervals with exception of $2 < p_\mathrm{T} < 3$ GeV/c for centrality 0–10%, where a second order polynomial is used. The invariant mass distribution is fitted between 2 GeV/c^2 and 3.7 GeV/c^2. The only exception is the interval with $0.15 < p_\mathrm{T} < 1$ GeV/c for centrality 0–10% with challenging residual background conditions complicating fitting. Thus, the fitting interval is reduced to 2.4–3.7 GeV/c^2 in this case. The mentioned choices allow to well constrain the fitting function in the vicinity of the J/ψ signal.

Finally, the J/ψ signal is extracted by counting of J/ψ candidate pairs and subtracting integral below the fit function. This is performed in the invariant mass interval 2.92–3.16 GeV/c^2 in order
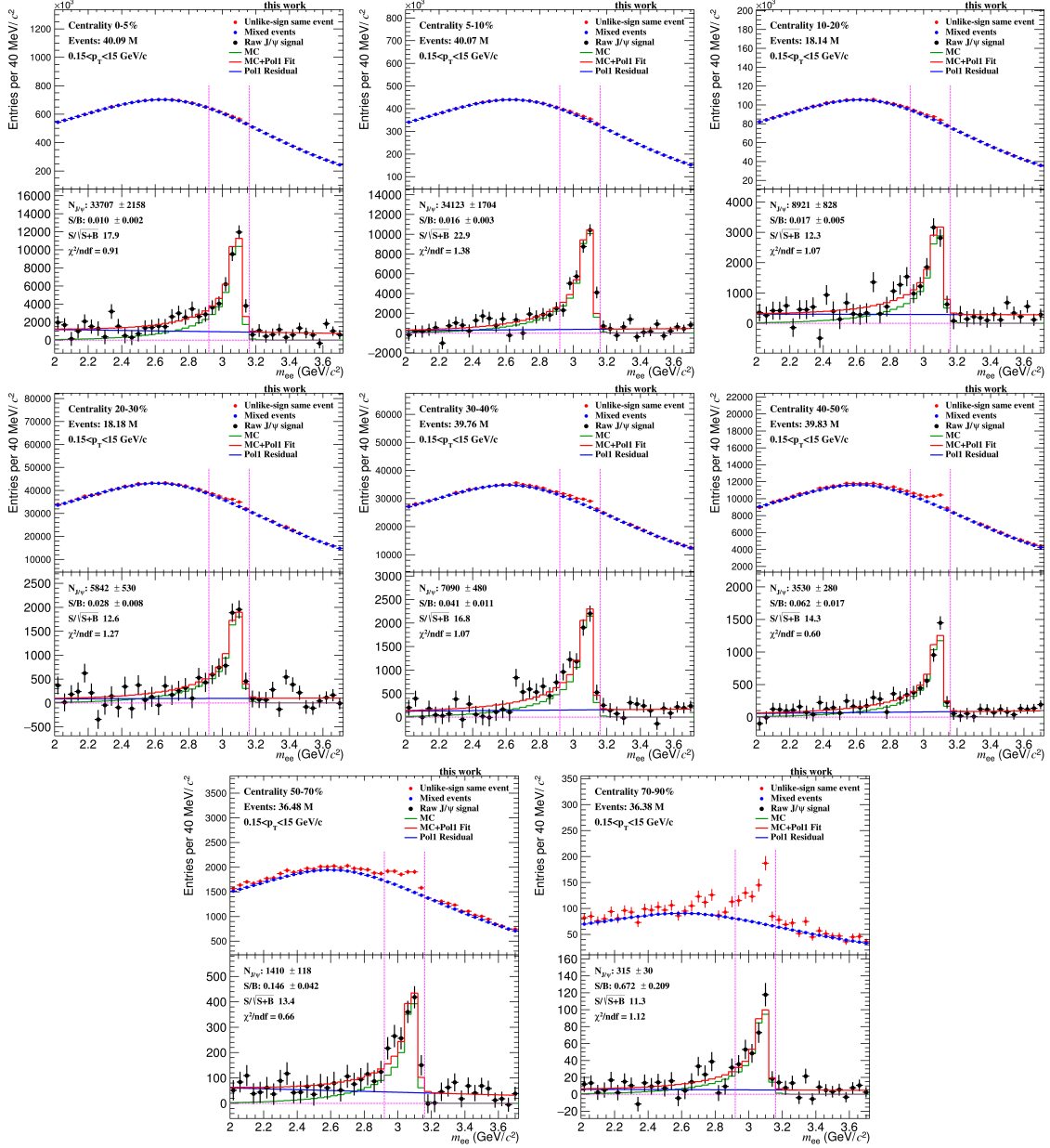
Figure 4.9: Invariant mass distribution of J/ψ candidates and background obtained by event mixing for different centralities and $0.15 < p_T < 15$ GeV/c are shown in the upper panels. The distribution of J/ψ candidates after subtraction of background modeled by event mixing is shown in the lower panels together with a fit function.

to optimize signal significance while keeping reasonable efficiency. The long tail reaching values below the J/ψ invariant mass is caused by the energy loss via bremsstrahlung complicating track momentum reconstruction and the radiative decay $J/\psi \rightarrow e^+e^-\gamma$. For the latter, the photon is not considered in the reconstruction of pair invariant mass. The small fraction of J/ψ peak exceeding the counting interval above the upper boundary is defined by the momentum resolution. In the p_T-integrated analysis, the significance exceeds 11 for all centrality bins. It reaches values 17.9 and 22.9 for most central events with centrality 0–5% and 5–10% due to the enhancement of collected events by the centrality trigger. For centrality intervals with the semi-central trigger, the significance is 16.8 and 14.3 for centralities 30–40% and 40–50%. This allows to perform a p_T-differential analysis in the
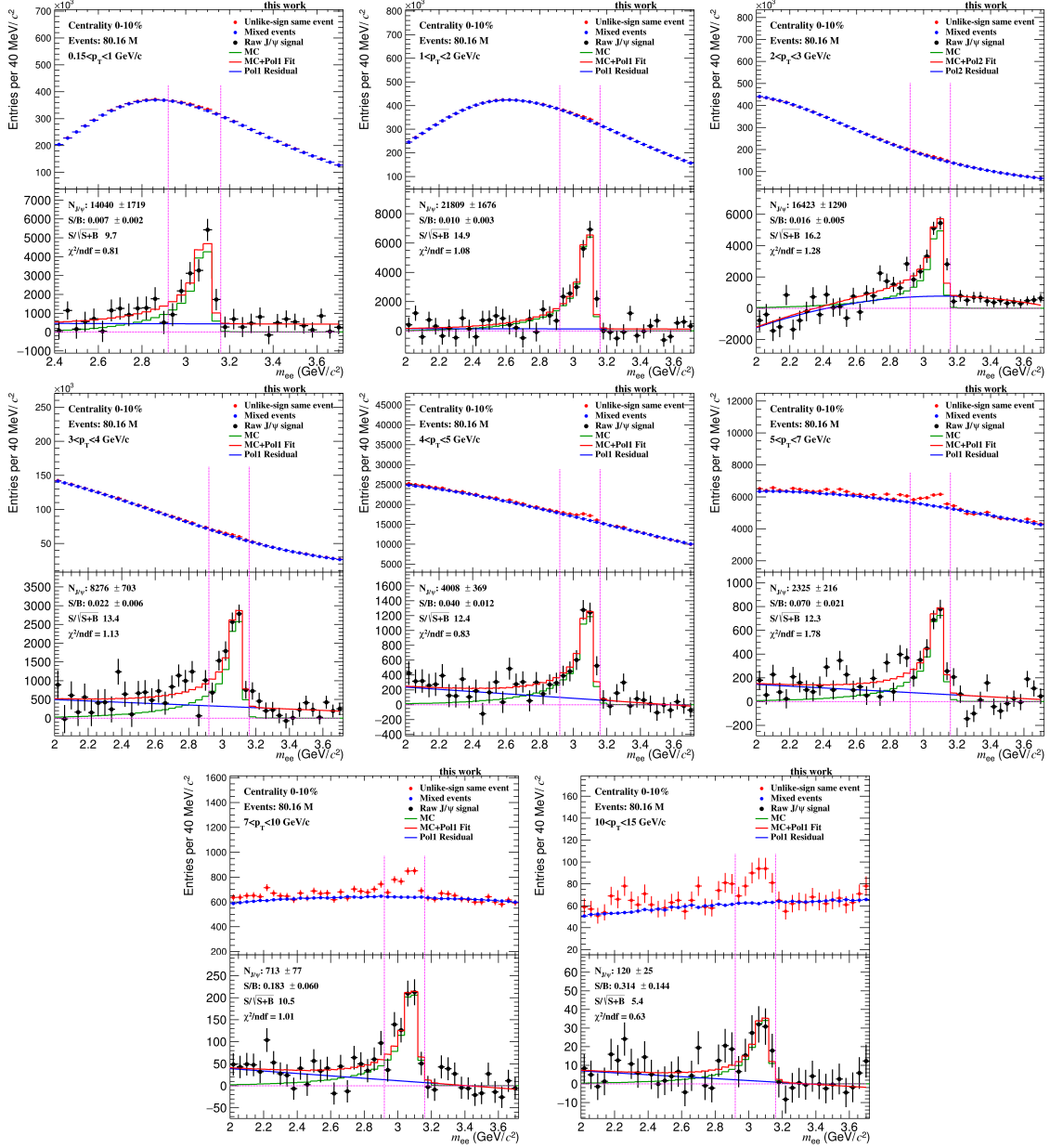
Figure 4.10: Invariant mass distribution of J/ψ candidates and background obtained by event mixing for centrality 0–10% and different p_{T} intervals are shown in the tops of the plots. The distribution of J/ψ candidates after subtraction of background modeled by event mixing is shown in the lower panels together with a fit function.

centrality classes 0–10% and 30–50% in relatively fine p_{T} intervals uncovering shape of p_{T}-spectra while keeping the statistical precision comparable to the systematic uncertainty.

The procedure of the signal extraction described above represents an improvement with respect to the previous measurement [152]. In the previous work, the residual background originating from the correlated background and the residual imperfections of the distribution of mixed-event pairs are neglected in the signal extraction. However, an improved statistical precision of the combined 2015 and 2018 data samples does not allow to continue in neglecting it. Thus, a polynomial function for description of the residual background is added as described above. The algorithm for the signal extraction is developed in ALICE within a common effort. The exact choice of a polynomial function
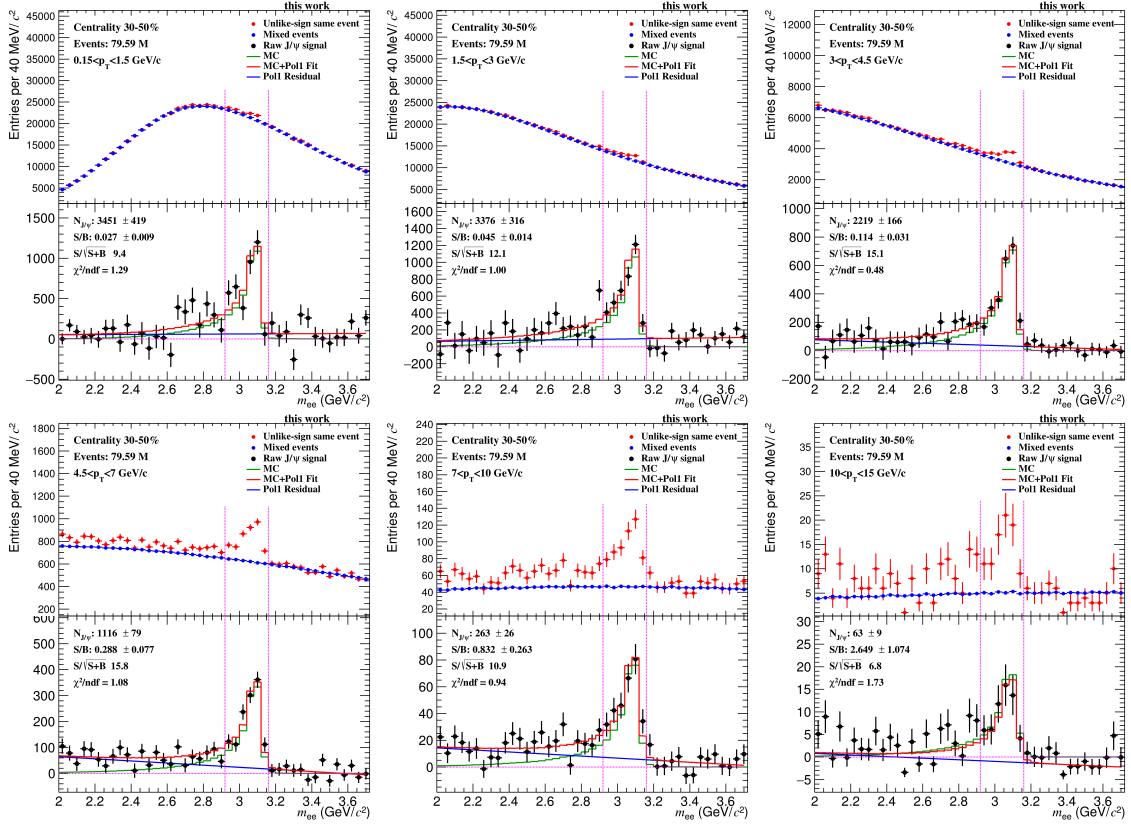
Figure 4.11: Invariant mass distribution of J/ψ candidates and background obtained by event mixing for centrality 30–50% and different p_{T} intervals are shown in the tops of the plots. The distribution of J/ψ candidates after subtraction of background modeled by event mixing is shown in the lower panels together with a fit function.

most suitable for the background description in each interval and the modification of the fit interval, where needed, is performed in the scope of this work. The same applies to the studies of the signal extraction systematic uncertainty sources presented in Subsection 4.6.3.

4.5 Acceptance and efficiency

The raw J/ψ signal per event is corrected for the acceptance and efficiency in order to get the number of J/ψ mesons per event created in the collected collisions in the rapidity window $|y| < 0.9$ and in the defined p_{T} interval. The acceptance times efficiency can be decomposed to the acceptance, the tracking efficiency, the PID efficiency and the efficiency of signal count in the constrained invariant mass window:

$$A \times \epsilon = \frac{N_{\mathrm{J}/\psi}^{\mathrm{acc}}(\Delta p_{\mathrm{T}}^{\mathrm{rec}})}{N_{\mathrm{J}/\psi}^{\mathrm{all}}(\Delta p_{\mathrm{T}}^{\mathrm{gen}})} \cdot \frac{N_{\mathrm{J}/\psi}^{\mathrm{acc,tr}}(\Delta p_{\mathrm{T}}^{\mathrm{rec}})}{N_{\mathrm{J}/\psi}^{\mathrm{acc}}(\Delta p_{\mathrm{T}}^{\mathrm{rec}})} \cdot \frac{N_{\mathrm{J}/\psi}^{\mathrm{acc,tr,PID}}(\Delta p_{\mathrm{T}}^{\mathrm{rec}})}{N_{\mathrm{J}/\psi}^{\mathrm{acc,tr}}(\Delta p_{\mathrm{T}}^{\mathrm{rec}})} \cdot \frac{N_{\mathrm{J}/\psi}^{\mathrm{acc,tr,PID,mass}}(\Delta p_{\mathrm{T}}^{\mathrm{rec}})}{N_{\mathrm{J}/\psi}^{\mathrm{acc,tr,PID}}(\Delta p_{\mathrm{T}}^{\mathrm{rec}})} = \qquad (4.6)$$
$$= A \cdot \epsilon_{\mathrm{tracking}} \cdot \epsilon_{\mathrm{PID}} \cdot \epsilon_{\mathrm{mass\,window}}.$$

$\Delta p_{\mathrm{T}}^{\mathrm{gen}}$ is the interval of the generated transverse momentum and $p_{\mathrm{T}}^{\mathrm{rec}}$ the reconstructed transverse momentum. $N_{\mathrm{J}/\psi}^{\mathrm{all}}$ denotes the number of all J/ψ mesons, $N_{\mathrm{J}/\psi}^{\mathrm{acc}}$ the number of J/ψ mesons passing acceptance selection criteria, $N_{\mathrm{J}/\psi}^{\mathrm{acc,tr}}$ the number of J/ψ mesons passing the acceptance and tracking selections, and so on.

The acceptance, tracking and mass window efficiencies are obtained using the MC simulation discussed in Subsection 4.2.2, whereas the PID efficiency is obtained from the data. All constituent efficiencies and $A \times \epsilon$ are shown in Figure 4.12 and discussed in more details later in this section.

The transverse momenta of the J/ψ decay daughters in the data differ from these reconstructed due to an experimental resolution. Thus, the true J/ψ transverse momentum in the data is as well not equal to the reconstructed one. For the calculation of the acceptance, the number of the generated J/ψ mesons in the MC simulation is counted in the interval of the generated transverse momentum Δp_T^{gen}, whereas the number of J/ψ mesons within acceptance is obtained in the interval of the reconstructed transverse momentum Δp_T^{rec}. Thus, the measured p_T shape reconstructed in the data is translated in the one equivalent to the true J/ψ p_T shape by applying the acceptance and efficiency correction. This approach represents a simplest form of the unfolding for the p_T resolution.

Furthermore, the re-weighting procedure is applied to make the generated p_T distributions shown earlier in the Figure 4.4 and the measured one corrected for the p_T resolution effect equal. In other words, the shape of the p_T^{gen} distribution in the simulation is weighted before obtaining the acceptance and efficiency to get the desired J/ψ meson p_T^{gen} shape. The desired shape is taken from the fit to the J/ψ p_T-differential production yield in the centrality class 0–10% obtained in this work. The first iteration is made using the preliminary result of the J/ψ production yield. The second iteration is then performed using the updated measured J/ψ production yield. Two iterations are sufficient given a current experimental precision.

The weight is calculated as normalized ratio of the p_T spectrum fit to the distribution of p_T^{gen} of the simulated J/ψ mesons. The efficiencies obtained without the weight would suffer from two bias sources. Firstly, the slope difference between the p_T spectra acts on the limit of small p_T intervals due to different contributions of a flow between the p_T intervals due the p_T resolution. Secondly, the difference between the p_T shape in the simulation and in the data would lead to different average efficiency in case of larger p_T intervals used in this work.
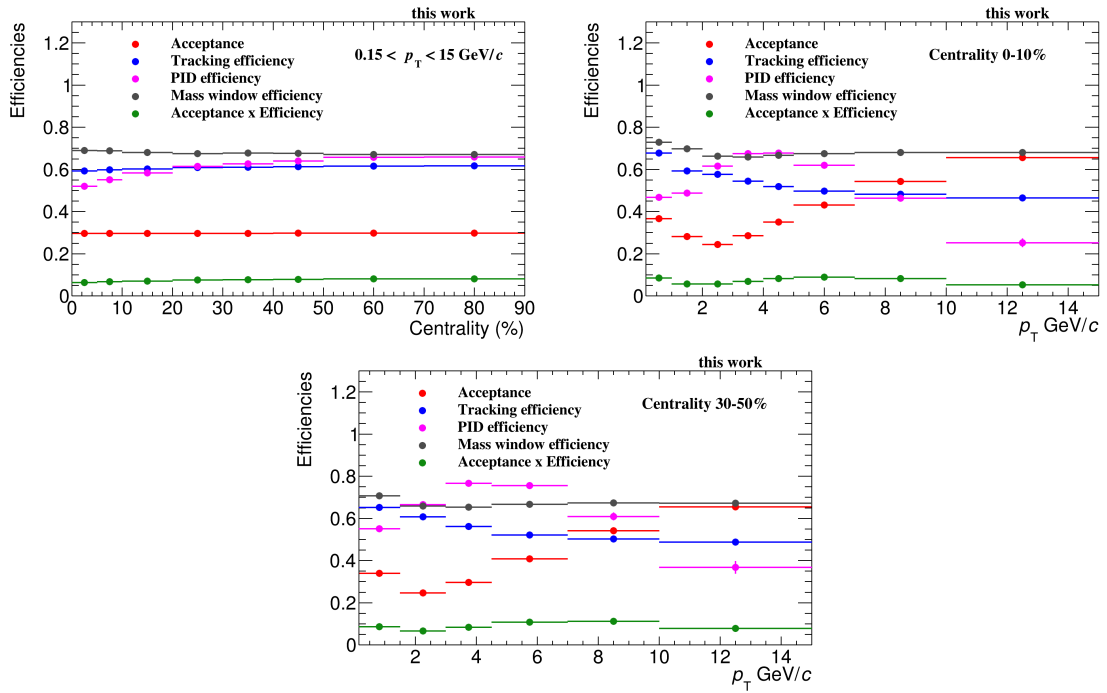
Figure 4.12: J/ψ acceptance and efficiencies as a function of centrality (top left) and p_T for centrality 0–10% (top right) and 30–50% (bottom).

The efficiencies slightly differ between the data sets. The differences are more visible between the data sets from years 2015 and 2018 since the data set collected in 2015 is taken under different

detector conditions and reconstructed by a different strategy compared to the 2018 data sets. Thus, the efficiencies obtained from the MC simulation are at first calculated separately for each of the data sets. Their average weighted by the numbers of events in the data sets is taken as the efficiency for merged data sets:

$$\epsilon = \frac{\epsilon^{\text{LHC15o}} \cdot N^{\text{LHC15o}} + \epsilon^{\text{LHC18q}} \cdot N^{\text{LHC18q}} + \epsilon^{\text{LHC18r}} \cdot N^{\text{LHC18r}}}{N^{\text{LHC15o}} + N^{\text{LHC18q}} + N^{\text{LHC18r}}}. \tag{4.7}$$
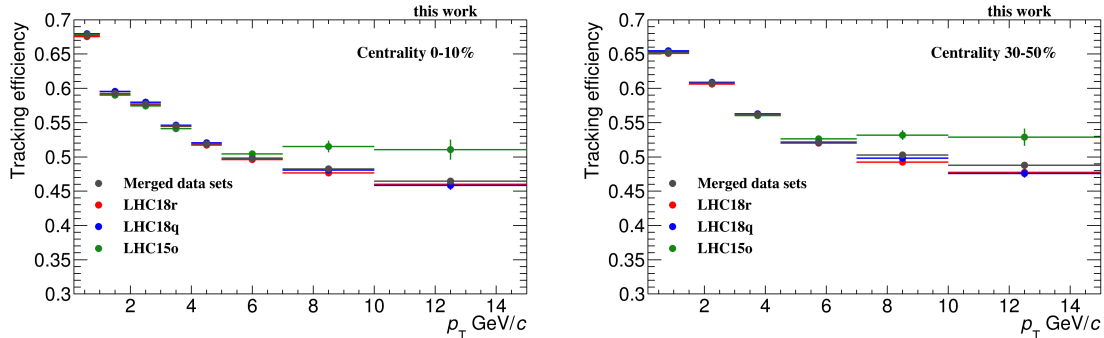
Figure 4.13: J/ψ tracking efficiency calculated separately for different data sets and for merged data set as a function of p_{T} for centrality 0–10% (left) and 30–50% (right).

The number of events for different centrality classes is discussed earlier in Subsection 4.2.1. An example of merged tracking efficiency and tracking efficiencies calculated separately for the data sets is shown in Figure 4.13. While the tracking efficiencies for the 2018 data sets are very similar, the tracking efficiency in the 2015 data set deviates from the 2018 data sets at high transverse momentum. As the abundance of events in the 2018 data sets is enhanced by the centrality triggers compared to the 2015 data set, the merged tracking efficiency for centrality intervals 0–10% and 30–50% resembles the tracking efficiency in the 2018 data sets.

The strategy for calculation of the PID efficiency for the merged data sets differs from the efficiencies obtained from the MC simulation. It is discussed in Subsection 4.5.3.

4.5.1 Acceptance

The acceptance is defined as the efficiency of selection on reconstructed transverse momentum and pseudorapidity discussed in Subsection 4.3.1. The acceptance for the p_{T} integrated yield analysis is approximately 0.3. It decreases with rising p_{T} up to the minimum between 2 and 3 GeV/c. This effect can be explained by the kinematics of J/ψ decays. J/ψ meson with $p_{\text{T}} \approx 0$ GeV/c decays to electron and positron with momenta of opposite directions and approximately same magnitude. Both of decay daughters (referred to as legs in following) pass the selection $p_{\text{T}} > 1$ GeV/c for leg pseudorapidity around zero due to large J/ψ invariant mass. For larger J/ψ p_{T}, the leg momenta become asymmetric in the laboratory frame as leg p_{T} component originating from the J/ψ invariant mass superimposes with the J/ψ meson p_{T}. As a result, p_{T} of one of the legs can fall below 1 GeV/c. The acceptance increases at larger J/ψ p_{T} since the leg p_{T} is more driven by the J/ψ meson p_{T}.

4.5.2 Tracking efficiency

Over 50% of the total tracking efficiency loss originates from the efficiency to find the J/ψ decay daughters in the TPC. Therefore, the shape of the tracking efficiency as a function of p_{T} is driven by the TPC track finding efficiency shape and the J/ψ decay kinematics similarly as in the case of the selection on track p_{T} and J/ψ acceptance. As is shown in [134], the TPC track finding efficiency in Pb–Pb collisions reaches its maximum for $p_{\text{T}} \approx 0.7$ GeV/c, drops rapidly below 0.7 GeV/c and decreases slowly with increasing p_{T} up to $p_{\text{T}} \approx 2.5$ GeV/c. The drop at low p_{T} originates from

energy loss in the detector material and shorter path length of low momentum tracks in the TPC. However, all the low momentum tracks affected by the drop are rejected already by acceptance selections. The shape at large p_T is caused by the dependence of the TPC cluster losses on the track p_T. The cluster losses originate mainly from the dead zones between the TPC read-out chambers. Further loss of the tracking efficiency originates predominantly from the ITS refit requirement and the requirement on at least one hit in the SPD layers. Each of these two selection criteria reduces the J/ψ tracking efficiency by approximately 10% of its value.

4.5.3 Data driven PID efficiency

The efficiency of PID selection criteria shown in Table 4.2 is in this work obtained from the data. This approach consists of two steps. Firstly, the leg PID efficiency is extracted using relatively clean electron sample from photon conversions as in the case of $n\sigma_e$ calibration parameters presented in Subsection 4.3.2. Afterwards, the leg efficiency is propagated to the pair level in order to get J/ψ efficiency. This approach represents substantial improvement in comparison to previous ALICE measurements of J/ψ at midrapidity in Pb–Pb collisions. Previous works obtained the PID efficiency from the MC simulation despite imperfections of the TPC PID MC simulation in high multiplicity environments.

As discussed in Subsection 4.3.2, the necessary pion and proton rejection criteria cause a sizable decrease in the J/ψ efficiency. Thus, the precision of the MC J/ψ PID efficiency relies on an accurate simulation of the separation power between electrons and protons and between electrons and pions. The TPC dE/dx signal in the data is not well described by the MC simulation. Therefore, the dE/dx distribution parametrization from data is applied in the MC simulation. The expected energy loss $\langle dE/dx \rangle$ and energy loss resolution for a particle in the MC simulation are obtained using the key components for $n\sigma_e$, $n\sigma_p$ and $n\sigma_\pi$ calculation in the data discussed in Subsection 3.5.3: the Bethe-Bloch fit to the mean dE/dx signal in the TPC $\langle dE/dx \rangle$, its correction and dE/dx signal resolution. The dE/dx signal for a present particle is generated while assuming a Gaussian with the mean at the expected mean dE/dx signal and the width equal to the dE/dx signal resolution. Afterwards, the TPC dE/dx signal is translated to the $n\sigma_e$, $n\sigma_p$ and $n\sigma_\pi$ by the same procedure as in the data.

However, the method for $n\sigma$ calculation in the data suffers from imperfections, especially in high multiplicity environments such as Pb–Pb collisions. This is proven by the fact that centroids and widths of $n\sigma$ distributions deviate from zero and unity as shown in Subsection 4.3.2. Therefore, the dE/dx signal distributions for different particle species and consequently also separation power in the MC simulation deviate from the true data distributions. On top of that, another problem with separation power description in the MC may arise from possible imperfections of the MC description of the event multiplicity and track PID clusters. The deviation between the J/ψ PID efficiency from the data and MC has been studied for the LHC15o data set used for publication [160]. It ranges between 0 and 12% for the p_T-integrated analysis.

Photon conversion electrons used for the PID efficiency calculation are selected by the same the tracking criteria as J/ψ electron candidates in order to keep the topology of the selected electrons as similar as possible to the topology of the J/ψ decays tracks. The only exception from this rule is the requirement on at least one hit in the SPD layers. The criterion is left out to increase the available track statistics since it rejects approximately half of the conversion electron candidates. This is caused by the fact that photon conversions in material occur in all ITS layers. Electron tracks from conversions at larger radii than the SPD detector cannot leave hits in the SPD detector.

The leg PID efficiency is obtained in intervals of event centrality, track momentum in the inner wall of the TPC detector p_{IN} and pseudorapidity η since the PID efficiency is affected by event activity and track properties. If the electron samples were absolutely clean, it would be possible to calculate leg PID efficiency simply by dividing the number of electrons after PID selections by their number without them. However, electrons from topologically selected photon conversions suffer from pion contamination from K_s^0 decays. Therefore, a purity of the electron sample is obtained using fit of a function consisting of two Gaussian functions to the $n\sigma_e^{cal}$ distribution of the contaminated electron sample. One Gaussian function describes a distribution of electrons, whereas the second one accounts for the contamination. The purity in one interval of $n\sigma_e^{cal}$ with edges $n\sigma_{e,1}^{cal}$ and $n\sigma_{e,2}^{cal}$
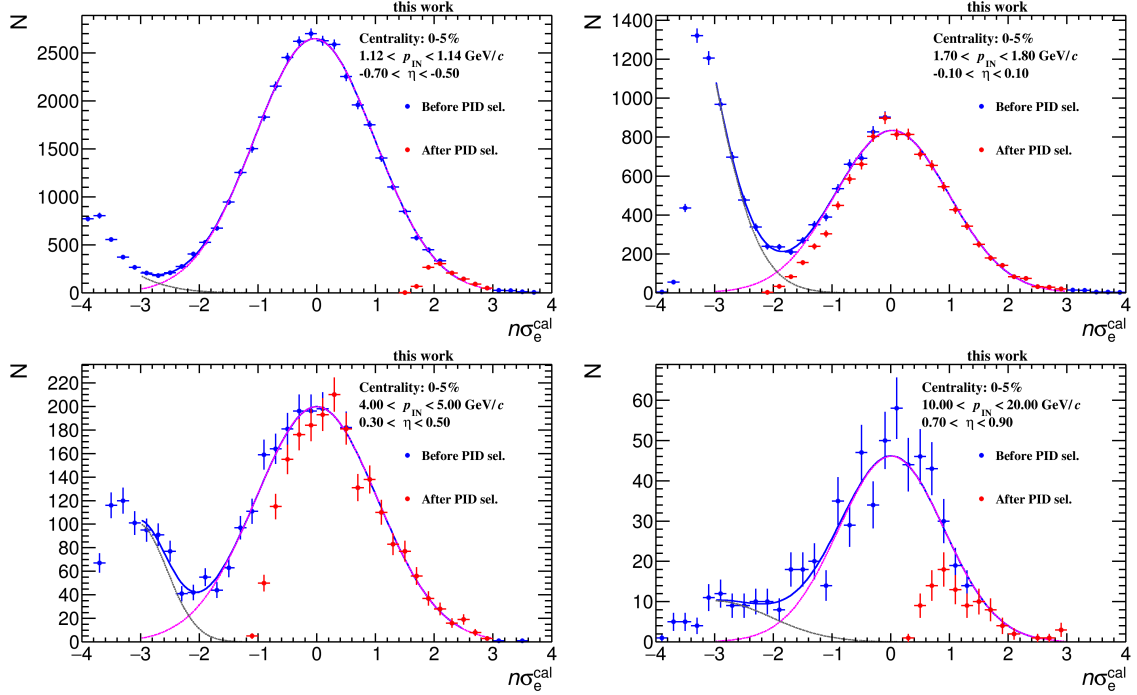
Figure 4.14: Examples of $n\sigma_{\mathrm{e}}^{\mathrm{cal}}$ distributions before (blue) and after (red) applying the PID selection criteria. Function consisting of two Gaussian functions used to describe $n\sigma_{\mathrm{e}}^{\mathrm{cal}}$ distribution is shown in blue color, the component describing the pion contamination in gray color and the electron component in magenta color.

is calculated by:

$$p(n\sigma_{\mathrm{e},1}^{\mathrm{cal}}, n\sigma_{\mathrm{e},2}^{\mathrm{cal}}) = \frac{\int_{n\sigma_{\mathrm{e},1}^{\mathrm{cal}}}^{n\sigma_{\mathrm{e},2}^{\mathrm{cal}}} f_{\mathrm{e}}(n\sigma_{\mathrm{e}}^{\mathrm{cal}})\mathrm{d}\sigma_{\mathrm{e}}^{\mathrm{cal}}}{\int_{n\sigma_{\mathrm{e},1}^{\mathrm{cal}}}^{n\sigma_{\mathrm{e},2}^{\mathrm{cal}}} (f_{\mathrm{e}}(n\sigma_{\mathrm{e}}^{\mathrm{cal}}) + f_{\pi}(n\sigma_{\mathrm{e}}^{\mathrm{cal}}))\mathrm{d}\sigma_{\mathrm{e}}^{\mathrm{cal}}}. \tag{4.8}$$

f_{e} and f_{π} are the Gaussian functions describing electron distribution and pion contamination. Finally, the leg PID efficiency is obtained by dividing electron counts before and after PID selections weighted by the purity:

$$\epsilon_{\mathrm{PID}}^{\mathrm{leg}} = \frac{\sum_{i=1}^{N_{bins}} N_{\mathrm{PID}}^{i}(n\sigma_{\mathrm{e}}^{\mathrm{cal}}) \cdot p^{i}(n\sigma_{\mathrm{e}}^{\mathrm{cal}})}{\sum_{i=1}^{N_{bins}} N_{\mathrm{woPID}}^{i}(n\sigma_{\mathrm{e}}^{\mathrm{cal}}) \cdot p^{i}(n\sigma_{\mathrm{e}}^{\mathrm{cal}})}. \tag{4.9}$$

N_{PID} is the number of the conversion electron candidates when applying the PID selection criteria and N_{woPID} is the number of the conversion electron candidates when not applying the PID selections. Examples of $n\sigma_{\mathrm{e}}^{\mathrm{cal}}$ distributions for electron sample before and after PID selections are shown in Figure 4.14. The examples correspond to different p_{IN} and η intervals and centrality 0–5%. Amount of pion contamination varies for the different cases.

Examples of the leg PID efficiency as a function of p_{IN} for different centrality and η intervals are shown in Figure 4.15. The specific proton energy loss in the TPC crosses the one for electrons close to $p_{\mathrm{IN}} = 1$ GeV/c. Therefore, all electrons around 1 GeV/c are excluded the by proton rejection criterion. Above $p_{\mathrm{IN}} = 1$ GeV/c, the leg PID efficiency at low momentum rapidly increases as the proton specific energy loss moves away from the electron one. The leg PID efficiency reaches its maximum around $p_{\mathrm{IN}} = 1.8$ GeV/c and decreases for larger momenta due to pion rejection. At the same time, it is smaller for more central events. This is caused by the worsening of separation power between electrons and protons/pions in the high multiplicity environment.

Examples of the leg PID efficiency as a function of η for different centrality and p_{IN} intervals are shown in Figure 4.16. As well as in the case of p_{IN} intervals, the exact choice of η intervals
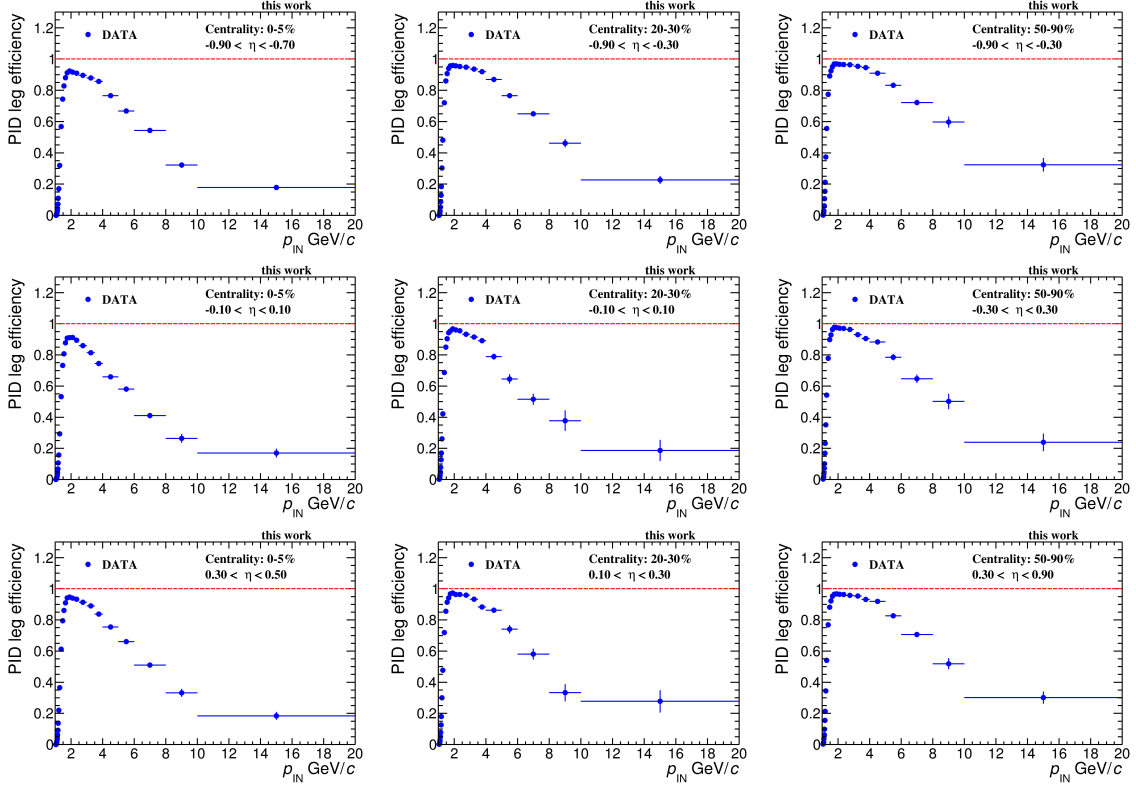
Figure 4.15: Examples of leg PID efficiency distribution as a function of p_{IN} for different η intervals and centralities 0–5% (left), 20–30% (middle) and 50–90% (right).

reflects available amount of conversion electrons and speed of leg PID efficiency change. If too coarse intervals were chosen in ranges, where the leg PID efficiency changes rapidly, it could lead to a sizable bias in the pair PID efficiency. On the other hand, too fine intervals would result in the decrease of the statistical precision of the PID efficiency. In this work, η intervals are finer in most central events with faster change of the leg PID efficiency as a function of η than in the case of peripheral collisions. The shape of the leg PID efficiency is similar for the proton crossing at low momentum and at high momentum region affected by the pion rejection.

The leg PID efficiency from the data is propagated to the pair level using J/ψ mesons generated in the standard MC simulation used to calculate other efficiencies in this work. This approach allows to employ the complex MC simulation including the propagation of the legs through detector or the simulation of radiative decays. This leads to a better precision compared to a simplified toy simulation used up to now for studies of the systematic uncertainty of the previous J/ψ measurements at midrapidity such as [66]. A validation of the precision of the new leg PID efficiency propagation approach is done by the closure test described later in Subsection 4.6.2.

In the new approach, each J/ψ count passing the acceptance and tracking selection criteria is weighted by a so-called efficiency weight:

$$w_{\mathrm{J}/\psi} = \epsilon_{\mathrm{PID}}^{\mathrm{leg1}}(p_{\mathrm{IN}}, \eta, \mathrm{centrality}) \cdot \epsilon_{\mathrm{PID}}^{\mathrm{leg2}}(p_{\mathrm{IN}}, \eta, \mathrm{centrality}). \qquad (4.10)$$

The weight is equal to the J/ψ PID efficiency for J/ψ decaying into legs with properties corresponding to the leg efficiencies $\epsilon_{\mathrm{PID}}^{\mathrm{leg1}}$ and $\epsilon_{\mathrm{PID}}^{\mathrm{leg2}}$. Finally, the pair PID efficiency is calculated by diving weighted J/ψ counts by counts without the efficiency weight. The J/ψ PID efficiency using each data set separately and merged data sets is shown in Figure 4.17. For the latter case, the data sets are merged before the calculation of the leg PID efficiency in order to improve the statistical precision. It has been tested that this approach does introduce a bias larger than the gained statistical precision.

61
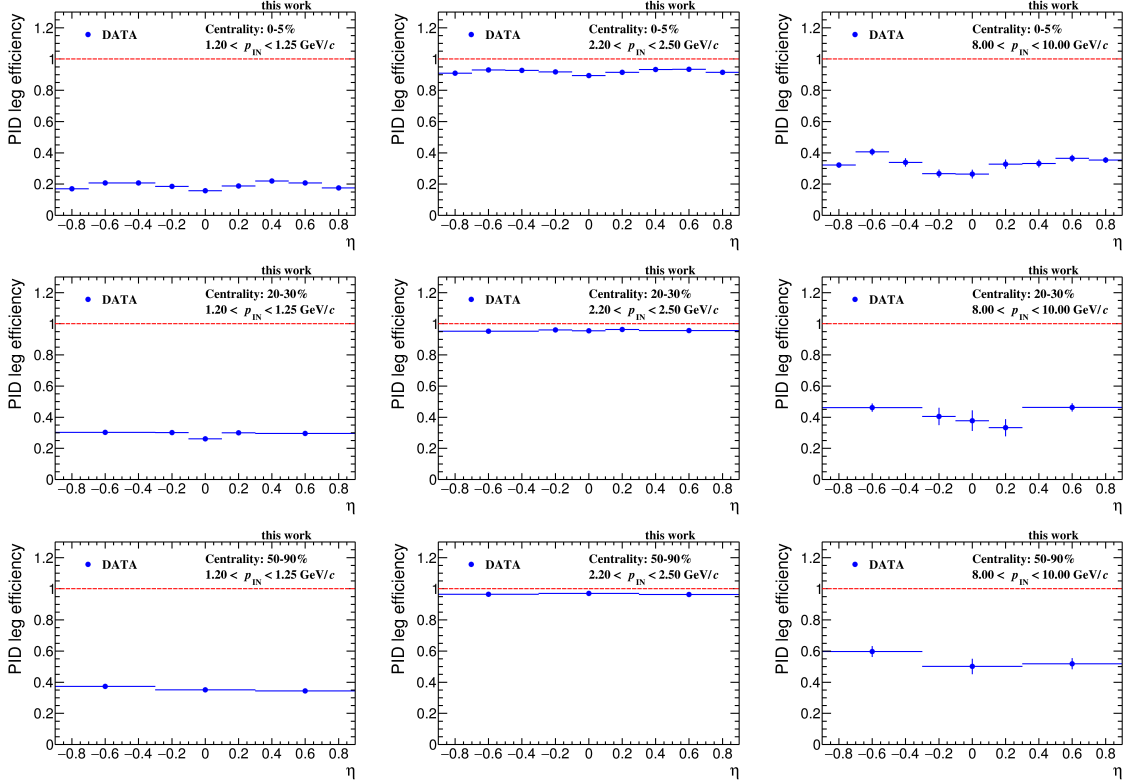
Figure 4.16: Examples of leg PID efficiency distribution as a function of η for different p_{IN} intervals and centralities 0–5% (top), 10–20% (middle) and 50–90% (bottom).

The PID efficiency is obtained also by the merging strategy from Equation 4.7 and is found to be consistent within statistical error bars with the default approach. A series of tests performed in order to further probe the precision of the PID efficiency is presented in Subsection 4.6.2.

4.5.4 Mass window efficiency

The J/ψ signal is counted only in the mass window 2.92–3.16 GeV/c as explained in the section 4.4. The centrality and p_{T} shapes depend on the fraction of pairs including an electron emitting bremsstrahlung passing the earlier applied selection criteria. Since the J/ψ invariant mass shape depends on previously applied selection criteria, the PID efficiency weight is applied before the mass window efficiency calculation. It ensures that the invariant mass shape used for the calculation reflects the PID selection criteria applied in the data. This is discussed in more details in Subsection 4.6.2.

4.6 Systematic uncertainty estimation

This section describes the strategy for the estimation of systematic uncertainties on the efficiency corrected J/ψ yields per event. There are three basic uncertainty categories considered: uncertainty originating from tracking, PID and signal extraction. Sources contributing to each category are discussed in details later in this section. The values obtained for the p_{T}-integrated Pb–Pb yields are shown in Table 4.3, whereas uncertainties for the p_{T}-differential analysis are shown in Tables 4.4 and 4.5.

The total uncertainty ranges between 8 and 11% for p_{T}-integrated yields and reaches values up to 15% for the highest p_{T} interval. The total uncertainty is dominated by the tracking contribution.
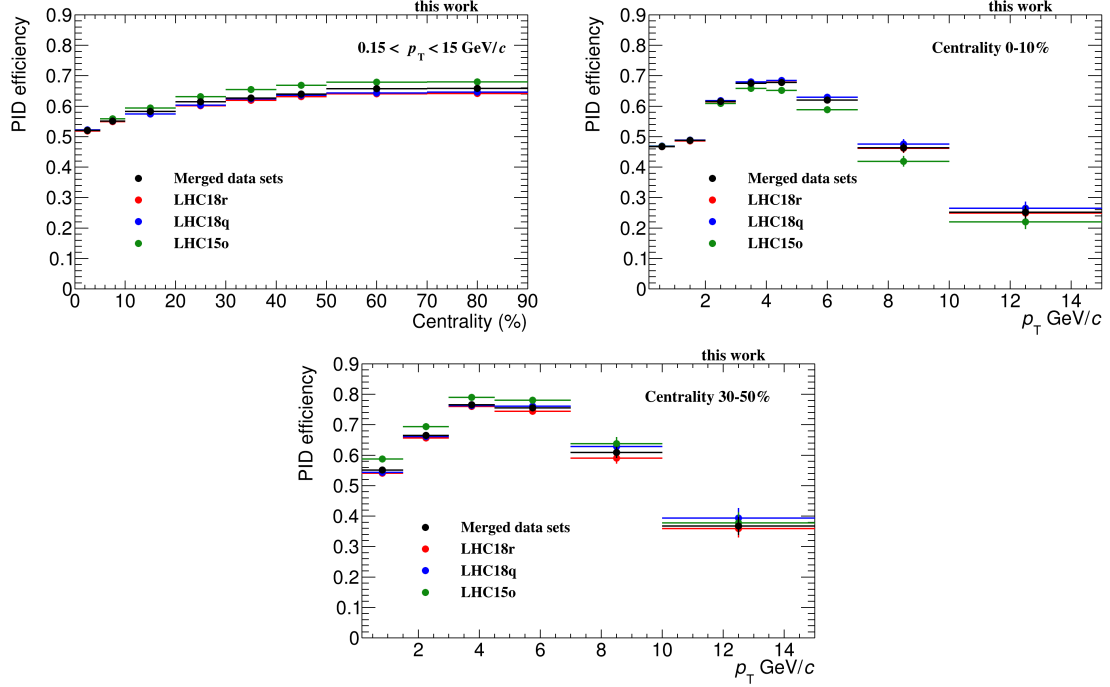
Figure 4.17: The J/ψ PID efficiency calculated separately for different data sets and merged data set as a function of centrality (top left) and p_{T} for centrality 0–10% (top right) and centrality 30–50% (bottom).

Uncertainty ↓ Centrality (%) →	0–5	5–10	10–20	20–30	30–40	40–50	50–70	70–90
Tracking, cut variations	2.7	2.7	2.7	2.7	2.7	2.7	2.7	2.7
Tracking, ITS-TPC matching	9.7	9.7	8.0	8.0	7.5	7.5	7.4	7.4
Tracking, total	10.1	10.1	8.5	8.5	8.0	8.0	7.9	7.9
PID, leg PID efficiency (statistical)	0.64	0.63	0.73	0.78	0.60	0.72	0.75	0.75
PID, fit range	0.15	0.07	0.01	0.06	0.03	0.03	0.04	0.04
PID, p_{IN} and η binning	0.65	0.63	1.04	1.06	0.90	0.96	0.80	0.80
PID, SPD any requirement	1.27	0.90	0.47	0.00	0.00	0.00	0.00	0.00
PID, closure test	0.30	0.31	0.37	0.45	0.27	0.32	0.31	0.73
PID, total	1.6	1.3	1.4	1.4	1.1	1.2	1.1	1.3
Mass fit range	0.9	0.8	1.6	1.9	0.7	0.8	1.3	1.6
Polynomial degree choice	2.3	2.6	1.0	6.3	2.5	0.5	1.2	2.0
Signal extraction, total	2.5	2.7	1.9	6.6	2.5	1.0	1.8	2.5
Total	10.5	10.5	8.8	10.8	8.5	8.2	8.1	8.4

Table 4.3: Systematic uncertainties on the efficiency corrected J/ψ yield in percent as a function of centrality for 0.15 < p_{T} < 15 GeV/c.

The second largest contribution in the most of considered centrality and p_{T} intervals originates from the signal extraction. A special attention has been paid to the PID uncertainty, since the strategy for the PID efficiency calculation considerably changed with respect to the previous works. The typical values for the PID systematic uncertainty are between 1 and 2% for p_{T} up to 7 GeV/c after considering five dominant PID uncertainty sources.

Studies of all of the considered systematic uncertainty sources are carried out within the scope of this work. Since the method of the PID efficiency calculation is newly data driven, the approach for

Uncertainty ↓ p_T(GeV/c) →	0.15–1	1–2	2–3	3–4	4–5	5–7	7–10	10–15
Tracking, cut variations	3.9	3.9	3.9	3.9	4.6	4.6	4.6	4.6
Tracking, ITS-TPC matching	9.4	9.8	10.1	10.1	9.7	8.8	7.3	6.3
Tracking, total	10.2	10.5	10.9	10.8	10.7	9.9	8.6	7.8
PID, leg PID eff. (statistical)	0.54	0.53	0.53	0.66	0.93	1.50	3.11	7.72
PID, fit range	0.14	0.11	0.09	0.08	0.10	0.08	0.13	0.27
PID, p_{IN}- and η-binning	1.02	0.76	0.52	0.34	0.38	0.00	0.00	0.00
PID, SPD any requirement	1.07	1.08	1.04	1.08	1.23	0.98	0.00	0.00
PID, closure test	0.37	0.30	0.31	0.33	0.37	0.19	0.66	0.95
PID, total	1.6	1.5	1.3	1.4	1.6	1.8	3.2	7.8
Mass fit range	2.2	1.5	3.3	1.1	2.8	2.1	1.1	2.7
Polynomial degree choice	3.4	5.7	0.4	2.4	4.5	1.0	4.7	5.1
Signal extraction, total	4.0	5.9	3.3	2.6	5.3	2.3	4.9	5.8
Total	11.1	12.1	11.4	11.2	12.1	10.3	10.4	12.5

Table 4.4: Systematic uncertainties on the efficiency corrected J/ψ yield in percent as a function of p_T for centrality 0–10%.

Uncertainty ↓ p_T(GeV/c) →	0.15–1.5	1.5–3	3–4.5	4.5–7	7–10	10–15
Tracking, cut variations	3.3	3.3	3.3	0.7	0.7	0.7
Tracking, ITS-TPC matching	7.6	7.7	7.5	6.8	5.7	5.0
Tracking, total	8.3	8.4	8.2	6.8	5.7	5.0
PID, leg PID eff. (statistical)	0.59	0.53	0.64	1.17	2.99	7.94
PID, fit range	0.02	0.03	0.06	0.07	0.09	0.11
PID, p_{IN}- and η-binning	1.22	0.88	0.64	0.45	0.00	0.00
PID, SPD any requirement	0.00	0.00	0.00	0.00	0.00	0.00
PID, closure test	0.36	0.28	0.24	0.43	0.95	0.86
PID, total	1.4	1.1	0.9	1.3	3.1	8.0
Mass fit range	1.4	0.9	1.1	2.1	0.8	2.8
Polynomial degree choice	0.6	1.1	0.7	4.8	0.1	11.1
Signal extraction, total	1.5	1.4	1.3	5.3	0.8	11.4
Total	8.5	8.6	8.4	8.7	6.6	14.8

Table 4.5: Systematic uncertainties on the efficiency corrected J/ψ yield in percent as a function of p_T for centrality 30–50%.

estimation of the uncertainty on the PID is as well completely changed with respect to the previous approach [152]. For the other sources of the systematic uncertainties, the largest differences in the currently used methods with respect to the previous measurement are specified in the corresponding sections.

4.6.1 Tracking

The tracking systematic uncertainty consists of two components: the uncertainty on the matching of TPC tracks to the ITS and the uncertainty on the efficiency for the track quality in the MC simulation.

A major fraction of the total uncertainty on the yields in Pb–Pb originates from the uncertainty on the ITS-TPC matching efficiency. The ITS-TPC matching efficiency is defined as the ratio of tracks with assigned clusters in the TPC and the ITS over the number of all TPC tracks. Only tracks found both in the ITS and the TPC can pass the applied tracking selection criteria. All of the TPC only tracks are rejected by the requirement on the track refitting in the ITS detector. Thus,

a possible discrepancy of the ITS-TPC matching in the MC simulation and the data can bias the tracking efficiency presented in Subsection 4.5.

The first step on the way to the ITS-TPC matching uncertainty estimation for J/ψ meson is the estimation of the single track uncertainty. Afterwards, this estimation is propagated to the pair level. The single track uncertainty on the ITS-TPC matching efficiency is obtained within a common effort in the ALICE Collaboration. The values provided by the collaboration relevant for this work are listed in Table 4.6. The values are calculated using pions due to their large abundance compared to electrons and the fact that values for electrons and pions are similar. A method carried out to obtain the provided values is based on the comparison of the ITS-TPC matching efficiency in the data and the simulation. However, the fraction of primary and secondary particles is different in the data and the MC simulation. This affects the inclusive ITS-TPC matching efficiency in the MC simulation since primaries have a higher efficiency. Secondaries contain for example tracks from strangeness decays likely to happen out of first two SPD layers or tracks from interactions with the detector material. Such tracks have on average less clusters in the ITS. The inclusive ITS-TPC matching efficiencies from the MC and the data are compared after the fraction of secondary particles in the MC simulation is corrected. The difference between the efficiency in the MC and the data is assigned as the systematic uncertainty on the ITS-TPC matching efficiency.

p_{T}(GeV/c)	1–2	2–3	3–4	4–5	5–6	6–7	7–8	8–9	9–10	10–11	11–12	12–13	13–100
Uncertainty (%), LHC18q, 0–10%	5	6	5	4	2	3	3	3	3	2	2	1	2
Uncertainty (%), LHC18r, 0–10%	5	6	4	3	2	3	2	2	2	2	2	2	2
Uncertainty (%), LHC18q, 30–50%	4	4	4	3	2	2	1	3	2	2	2	3	2
Uncertainty (%), LHC18r, 30–50%	4	4	2	2	2	1	1	2	2	2	2	2	2
Uncertainty (%), LHC15o, 0–90%	3.3	4.6	3.9	3.7	2.2	2.3	2	1.6	1.2	1.2	1.2	1.3	1.3

Table 4.6: Systematic uncertainty on the ITS-TPC matching efficiency carried out in common effort within the ALICE Collaboration as a function of p_{T}.

The method for the uncertainty propagation to the pair level exploits as in the case of the PID efficiency propagation the efficiency weight presented in Subsection 4.5.3. The leg efficiency is set to unity minus the track ITS-TPC matching efficiency uncertainty. The uncertainty for J/ψ mesons is obtained by dividing weighted J/ψ counts by unweighted J/ψ counts in the MC simulation. Since the uncertainty for tracks is provided as a function of track p_{T} and event centrality, the procedure is performed while considering dependencies on these variables. However, the uncertainties in the case of the 2018 data sets are provided only for the centrality classes 0–10% and 30–50%. Therefore, the averaged values of the leg uncertainties are set for the centrality range 10–30%. The uncertainties for the centrality class 30–50% serve as a rather conservative estimate for the events with the centrality interval 50–90%. The leg uncertainties vary between the data sets. Thus, the leg uncertainties are propagated separately for each of them and later averaged using the number of events in the data sets. This approach is same as in the case of the efficiency merging from the Equation 4.7.

The final relative uncertainty on the ITS-TPC matching for the J/ψ mesons efficiency is shown together with uncertainties for separate data sets in Figure 4.18. It is approximately twice as large as the leg uncertainty. The p_{T} shape follows approximately a shape of the leg uncertainties, which are largest at low p_{T} and decrease above $p_{\mathrm{T}} \approx 4$ GeV/c.

Some of the further tracking properties are not precisely described in the MC simulation. This is a source of a discrepancy between tracking efficiency in the data and its simulation as well as in the case of the ITS-TPC matching. The uncertainty caused by the imperfect description of the track quality selection criteria is estimated by a simultaneous variation of the selections on TPC χ^2/ndf and the requirements on hits in the SPD detector. These selection criteria cause the largest
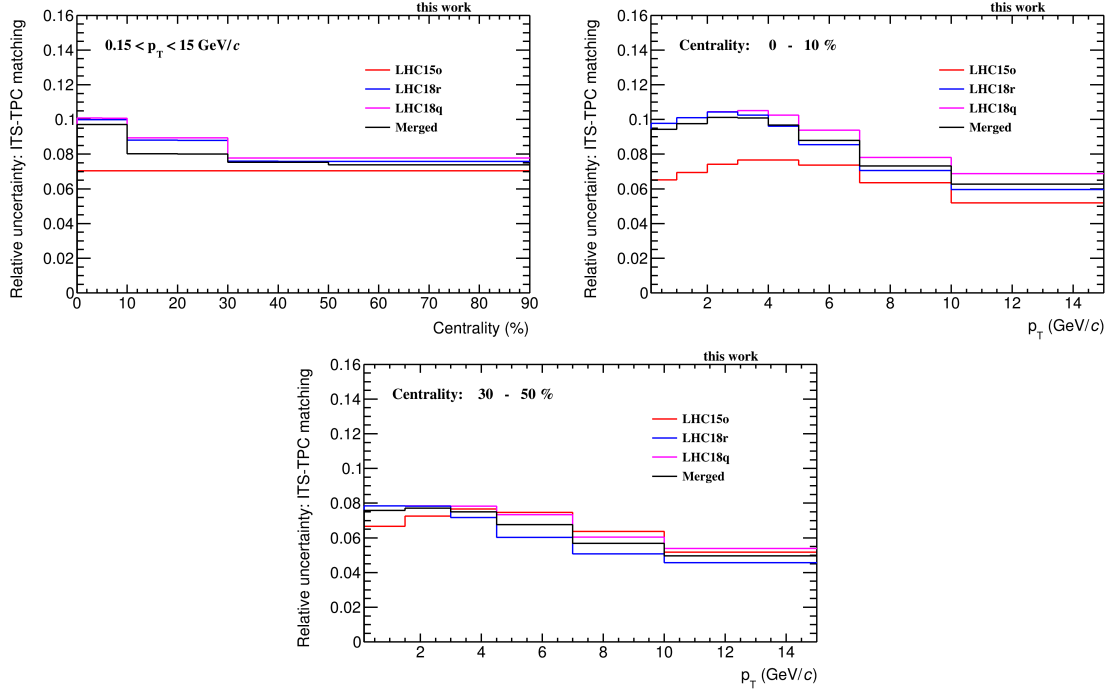
Figure 4.18: Systematic uncertainty originating from the uncertainty on the ITS-TPC matching efficiency as a function of the centrality (top left) and p_T for centrality 0–10% (top right) and 30–50% (bottom).

differences in the corrected J/ψ yields while being varied. The considered configurations are the following:

- LHC18r and LHC18q: TPC χ^2/ndf < 2.2, 2.5 (standard), 2.8,

- LHC15o: TPC χ^2/ndf < 3.5, 4.0 (standard), 4.5,

- requirement on at least one hit in the SPD (standard) and on one hit in the first SPD layer.

The chosen selections on the TPC χ^2/ndf differ for 2018 and 2015 data sets since this variable has different distributions in these two years due to a changed reconstruction strategy as discussed in Subsection 4.3.1. When the tightest/standard/loosest selection is applied in the 2018 data sets, the tightest/standard/loosest selection is applied as well in the 2015 data set. In the approach of the simultaneous variation, all possible combinations of one selection from the set of the TPC χ^2/ndf selections and one selection of the set of the requirements on the hits in the SPD detector are used.

The uncertainty on the tracking efficiency is not expected to vary rapidly with centrality and p_T. Therefore, the whole procedure can be performed in wider centrality and p_T intervals than in the analysis of the corrected yields itself in order to suppress the influence of statistical fluctuations:

- The centrality intervals 0–10% and 30–50% with a large abundance of the collected events are used to calculate the desired uncertainties. The uncertainty for the centrality interval 10–30% is obtained by averaging the values from neighboring intervals. The uncertainty for the centrality interval 50–90% are taken from the interval 30–50%.

- p_T-differential analysis, the centrality interval 0–10 %: 0.15, 4, 15 GeV/c.

- p_T-differential analysis, the centrality interval 30–50%: 0.15, 4.5, 15 GeV/c.
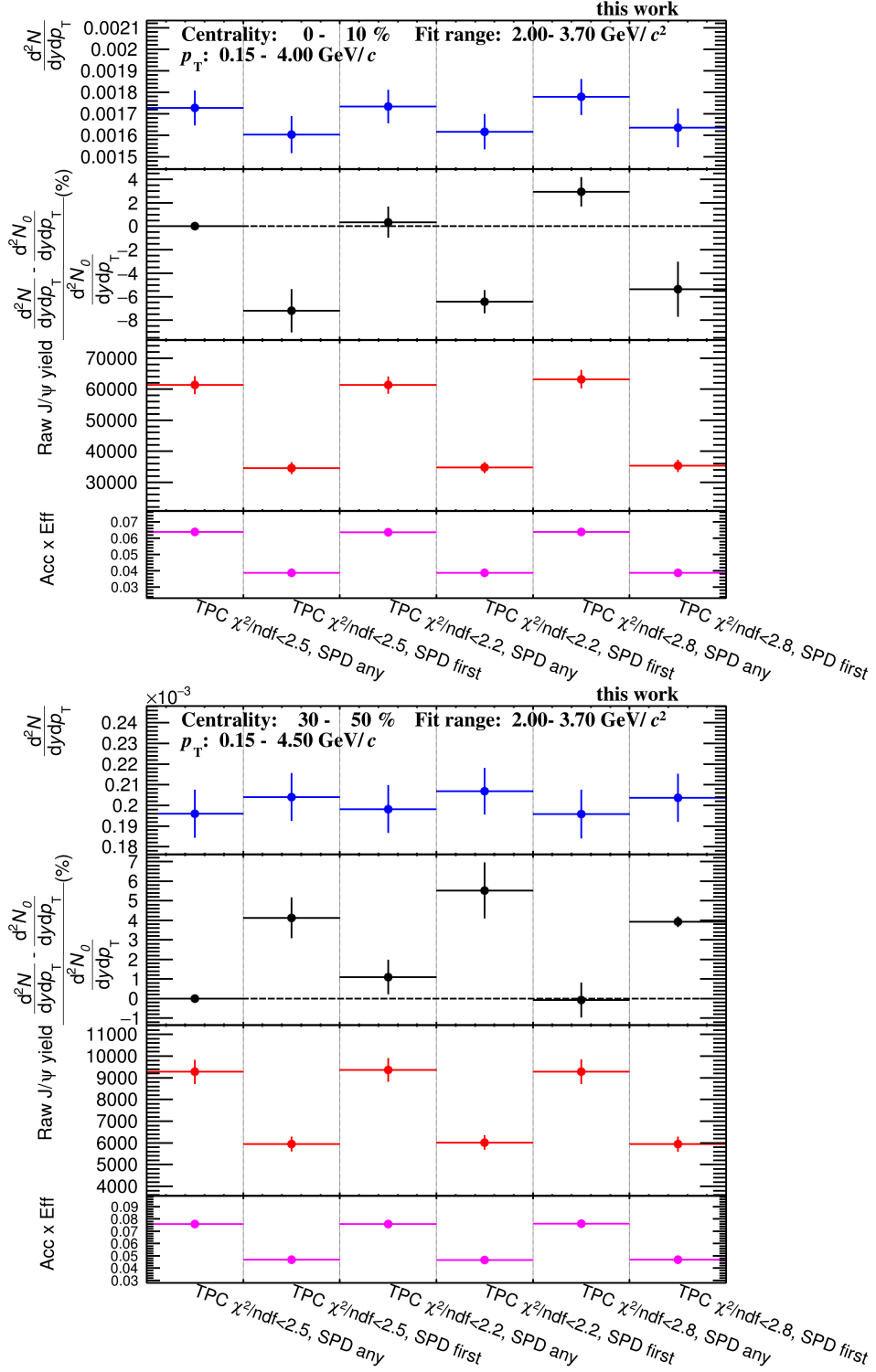
Figure 4.19: Corrected J/ψ yield, deviation from the standard case, J/ψ raw yield and acceptance times efficiency as a function of tracking selection criteria variations. The first tracking selection criterion is the standard one. Shown examples correspond to the standard fit range, p_T range $0.15 < p_T < 4$ GeV/c and the centrality interval 0–10% (top) and the centrality interval 30–50% (bottom).
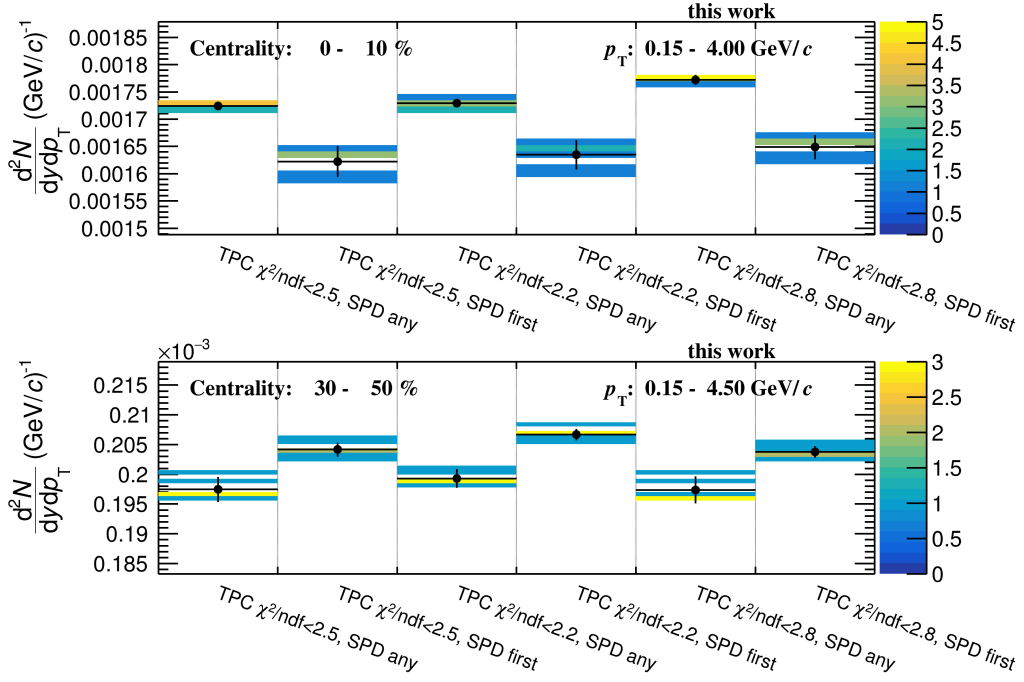
Figure 4.20: Examples of corrected J/ψ yield for simultaneous fit range and tracking selection variations. Means of cases with different fit ranges for one set of tracking selections shown in black. Color scale corresponds to the number of the variations falling into an interval of corrected J/ψ yield.
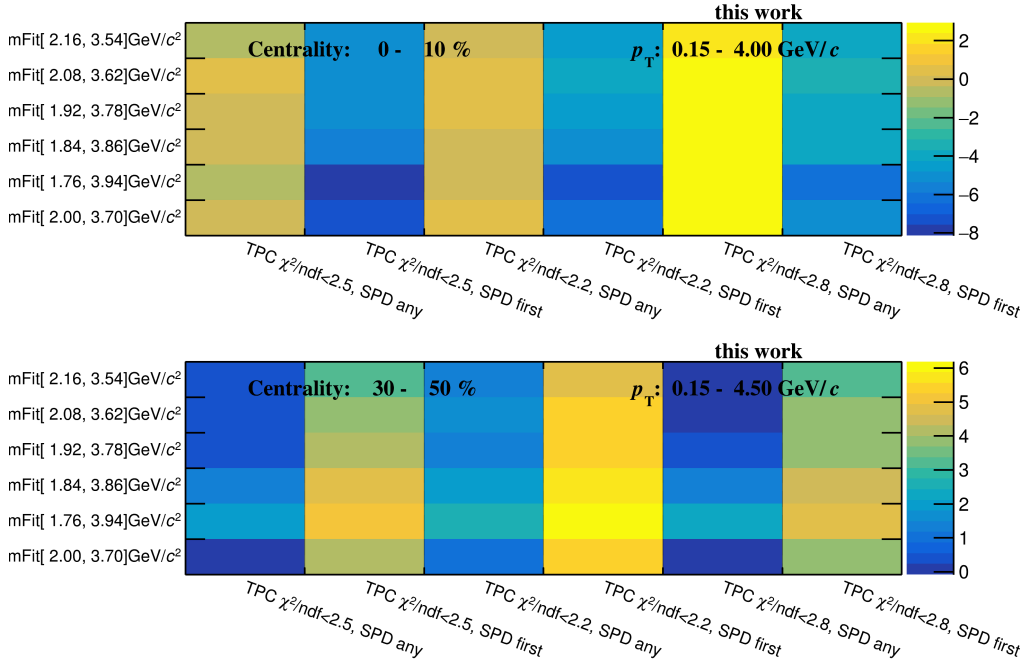
Figure 4.21: Examples of deviations in percent shown in color from the standard case for the simultaneous variations of the tracking selection criteria and fit range.

The variations of tracking selection criteria are shown in Figure 4.19. Although changes in raw J/ψ yield are approximately followed by the efficiency, relative difference between the corrected yield for the standard case and variations reveals deviations up to 8% for shown examples. The deviations are often not consistent with zero within error bars suggesting that the method uncovers rather systematic deviations than fluctuations of the J/ψ yield. The tracking selection criteria are varied together with the fit range for the signal extraction. This approach minimizes bias from choice of the fit range on the resulting uncertainty from the tracking. All used settings of the mass fit range are listed later in Subsection 4.6.3. Within the simultaneous variation approach, all possible combinations of one of the tracking selection settings and one of the mass fit ranges are used.

Simultaneous variations of the tracking selection criteria and the fit range are shown in Figure 4.20. The colors in the figure reflect the number of cases falling in an interval of the corrected J/ψ yield $\mathrm{d}^2N/(\mathrm{d}y\mathrm{d}p_\mathrm{T})$. Black points correspond to the means of the fit range variations for a fixed tracking selection variations. Their root mean square deviation (RMS) calculated using the case with the standard fit range and standard selection criteria as the reference mean is used for the uncertainty estimation. The uncertainty obtained in this way reflects whether the corrected J/ψ yield of the standard case belongs rather to utmost variations or is located in the middle of them. For example, the standard case for centrality 30–50% and $0.15 < p_\mathrm{T} < 4.5$ GeV/c belongs rather to utmost variations. This can be seen in Figure 4.21 showing the deviations in percents from the standard case for all of tracking selection and fit range settings. The distribution of the means for different variations of the selection criteria is shown in Figure 4.22. The RMS divided by the mean value (relative RMS) is assigned as the systematic uncertainty. The systematic uncertainty from the tracking selection criteria ranges from 0.7 to 4.6% for all centrality and p_T intervals.
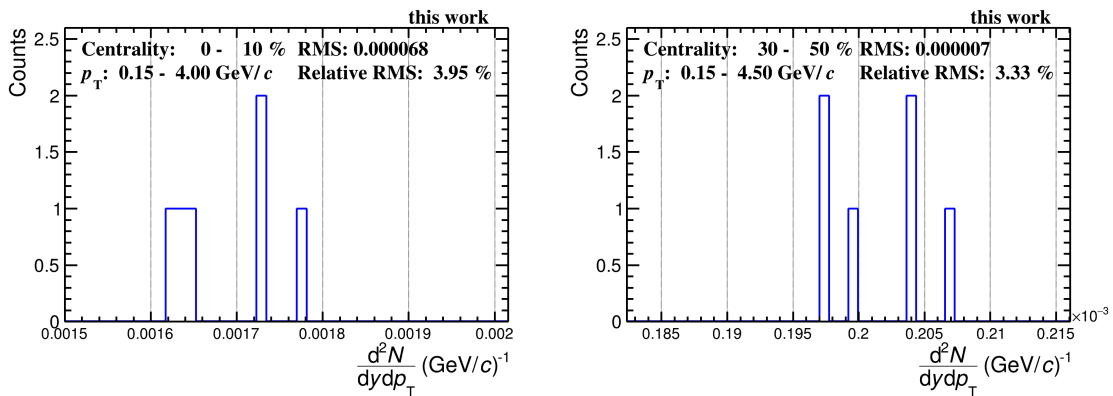
Figure 4.22: Distribution of means over signal extraction variations for a given tracking selection used for the estimation of systematic uncertainty originating from imperfect MC description of tracking selection criteria. Each entry corresponds to one tracking selection criterion.

The most significant difference between the current methods for the estimation of the systematic uncertainty on tracking used in this work and in the previous measurement [152] lies in the calculation of the systematic uncertainty arising from the uncertainty on the ITS-TPC matching efficiency. It is very difficult to extract the uncertainty values for this source by the variation of the selection criteria as it is done in the previous analysis. This is caused by the fact that the ITS refit is one of the crucial track quality selection criteria. It cannot be removed for the J/ψ signal reconstruction since it would cause a large increase of the background in the reconstructed invariant mass distribution. At the same time, there is no good alternative option to tighten the tracking selection criteria in a similar way as by adding the ITS refit to the list of the selection criteria.

The tracking systematic uncertainty investigated solely by the tracking variations in the previous measurement ranges for the p_T-integrated analysis between 2 and 7%. However, the contribution from the ITS-TPC matching uncertainty alone is for the 2015 data set approximately 7% as can be seen in Figure 4.22.

4.6.2 Particle identification

The systematic uncertainty originating from PID can be divided into three categories: the statistical uncertainty on the PID efficiency defined by the abundance of the photon conversion electrons, uncertainty from the closure test of the PID efficiency propagation and the uncertainty from other various systematic sources. All of them will be described in detail in this subsection.

The PID efficiency is obtained from the data as it is described in Subsection 4.5.3. The data driven PID efficiency suffers from a low abundance of the clean electron sample from photon conversions in some of the intervals used for the leg PID efficiency calculation. These are typically high p_{IN} intervals and finer η intervals around the central electrode for the centralities 10–50%. Therefore, the statistical uncertainty on leg PID efficiency is considered as one of the PID systematic uncertainty sources. The procedure starts with setting the leg PID efficiency in every interval to the PID leg efficiency plus one sigma of the statistical uncertainty. The same procedure is repeated with the negative deviation. Both cases are propagated to obtain the corresponding J/ψ PID efficiency using the efficiency weight described in Subsection 4.5.3. The deviation between the standardly obtained J/ψ PID efficiency and the upper and lower bounds is approximately symmetric. The full relative difference of these two cases divided by two is taken as the systematic uncertainty.

The statistical deviation of the leg PID efficiency in different intervals is in the data independent from each other. Therefore, this approach for the uncertainty estimation of the J/ψ PID efficiency tends to overestimate the uncertainty since all of the leg PID efficiency values are either simultaneously increased or simultaneously decreased. However, this overestimation is not a problem since the total systematic uncertainty is not dominated by this source in almost full kinematic region probed in this work.

The resulting relative PID systematic uncertainty from the statistical uncertainty on the PID leg efficiency as a function of centrality and p_{T} can be seen in Figure 4.23. The uncertainty is below 1% at p_{T} below approximately 5 GeV/c. At higher p_{T}, this source of systematic uncertainty steeply grows up to 8% for $10 < p_{\mathrm{T}} < 15$ GeV/c. This is caused by an increase of the statistical uncertainty at high leg momentum. J/ψ mesons with high p_{T} tend to have also at least one of the legs with high momentum. The uncertainty for p_{T}-integrated cases is below 1% since the majority of the J/ψ mesons is produced at a p_{T} interval with low systematic uncertainty from this source.
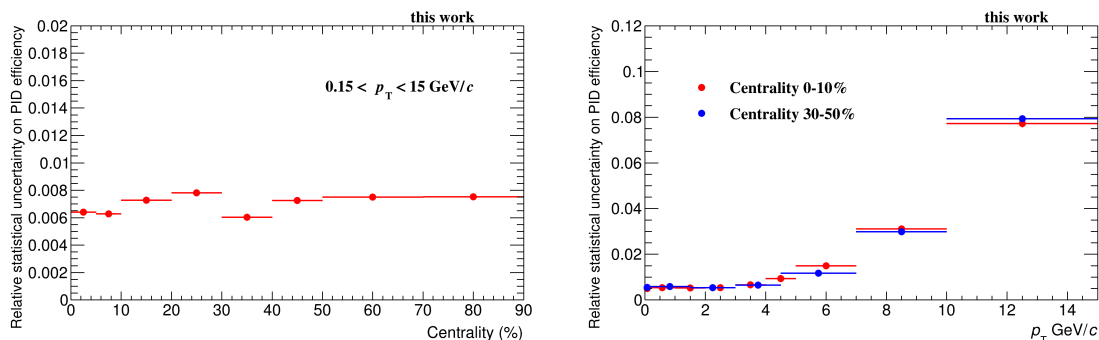
Figure 4.23: The systematic uncertainty from the statistical uncertainty on the leg PID efficiency as a function of centrality (left) and p_{T} for centralities 0–10% and 30–50% (right).

The propagation of the leg PID efficiency by the efficiency weight via the standard J/ψ MC simulation is tested by a closure test. The MC PID efficiency is obtained using two ways that should ideally give both exactly the same result. Firstly, the J/ψ PID efficiency is obtained by the standard procedure used in the previous measurements at midrapidity based on the selections on the number of standard deviations from electron, proton and pion hypotheses $n\sigma_{\mathrm{e}}$, $n\sigma_{\mathrm{p}}$, $n\sigma_{\pi}$ in the MC simulation. This is analogue to the calculation of the acceptance and the tracking efficiency in Subsections 4.5.1 and 4.5.2. Secondly, the leg PID efficiency in the MC J/ψ simulation is calculated in the same centrality and η intervals as used to obtain J/ψ PID efficiency in the most central events from the data. The abundance of J/ψ electrons in the MC simulation is larger than in the case of

the photon conversion electrons in the data. Thus, finer p_{IN} intervals are chosen for the closure test than in the data to minimize the binning effect while keeping a very good statistical precision. The ratios of the PID efficiency for the two discussed cases is shown in Figure 4.24. A small deviation from unity below one percent is observed and added to the systematic uncertainty on the PID. The same check is performed separately for all three data sets with identical conclusions.
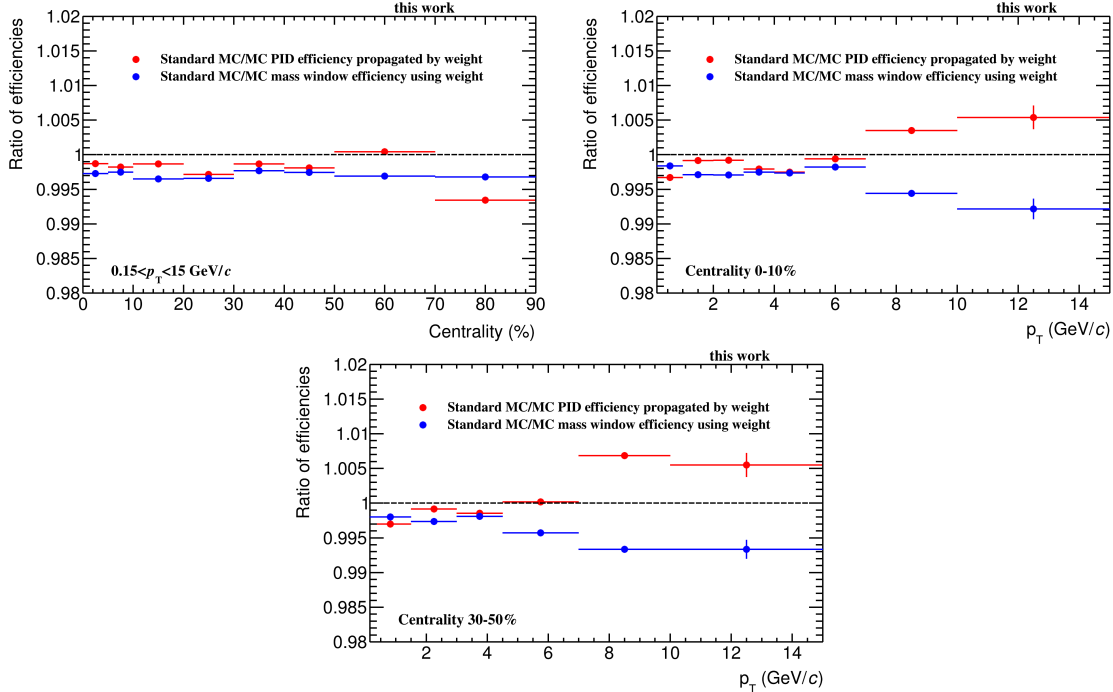
Figure 4.24: Ratios of MC PID and mass window efficiencies: the ratio of the standard MC J/ψ PID efficiency to the J/ψ PID efficiency propagated via the efficiency weight using the MC leg PID efficiency and the ratio of mass window efficiency after applying PID selections in the MC simulation to the efficiency weight. The ratios are shown as a function of centrality (top left) and p_T for centrality 0–10% (top right) and centrality 30–50% (bottom).

It was found that there are substantial differences at low p_T between the mass window efficiency when applying and not applying PID selection criteria in the MC simulation before the calculation of the mass window efficiency. Since PID selections in the data and the simulation differ, the PID efficiency weight is applied before the calculation of the mass window efficiency as discussed in Subsection 4.5.4. Therefore, the closure test is performed not only in the case of the PID efficiency, but also for the mass window efficiency. Examples of J/ψ invariant mass shapes without applying PID selection criteria, when applying them in the simulation and when testing the efficiency weight are shown in Figure 4.25. The latter two cases should result ideally in the same shape of the distribution. They are indeed almost identical. The shape without PID selections has a larger tail towards lower values caused by a larger abundance of electrons emitting bremsstrahlung passing the previously applied selection criteria at low momenta. They are partially rejected by the proton exclusion in the case of PID selections applied. The ratios of the mass window efficiency with PID selections in the simulation to the case with the efficiency weight are shown in Figure 4.24. Deviation of the ratio from unity is below 1% in all intervals and is added to the systematic uncertainties.

Few other sources of PID systematic uncertainty are considered. The ratio of the PID efficiency with standard settings to the PID efficiency with different settings for systematic studies is calculated for each individual source and shown in Figure 4.26. The difference is added to systematic uncertainty when the ratio deviates from unity by more than one standard deviation. The following sources are studied:
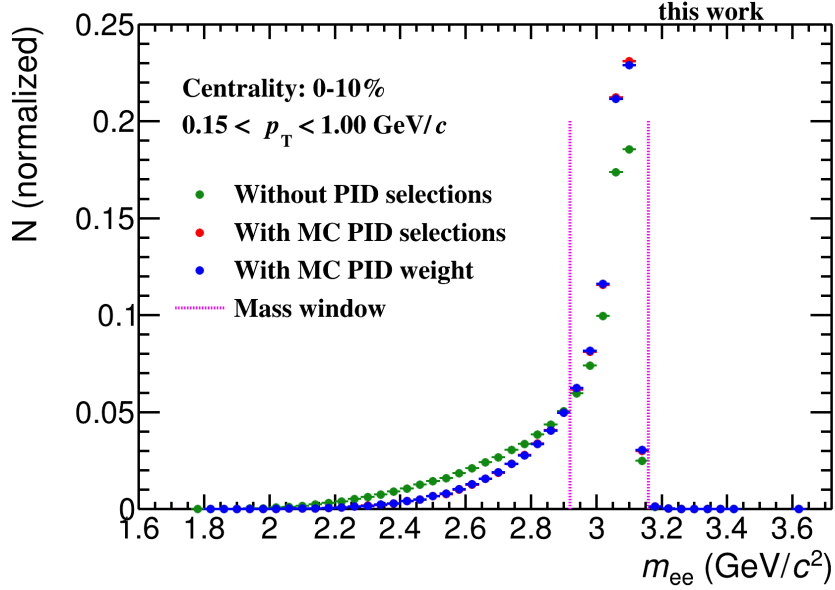
Figure 4.25: J/ψ invariant mass shape for $0.15 < p_T < 1$ GeV/c and centrality 0–10% for three cases: when not applying PID selections, when applying MC PID selections and when applying the efficiency weight using the MC leg PID efficiency.

- The leg PID efficiency is obtained in p_{IN} and η intervals causing a deviation from a true continuous shape. Thus, finer p_{IN} and η binning is set to estimate the effect of the binning granularity on the J/ψ PID efficiency.

- The purity of photon conversion electron sample is estimated by a fit to $n\sigma_e$ distribution constrained to interval $-3 < n\sigma_e < 3$. The pion contamination is present in the area of the lower bound of the interval. Therefore, the lower bound is varied to -2.8 and -3.2 in order to study effect of background fraction included in the fit. This source contributes to the total PID uncertainty the least from all studied sources.

- Opening angles of photon conversions are typically small. In addition, photons can converge to electron pairs in a detector material located further from the interaction point. The distances of two tracks from such conversion are small in areas close to the inner wall of the TPC. This can lead to a bias of measured energy loss in the TPC associated to these two tracks. Electrons from conversions occurring later than in the first four ITS layers should be removed by the requirement on track refitting in the ITS. However, a possible effect of persisting fraction of near photon conversion electron tracks in the TPC is studied by applying stricter ITS selections. At least one hit in the SPD layers is required in addition to the standard photon conversion electron selections. The uncertainty from this source is estimated to be zero for centrality ranges above 20% since the ratio of standard PID efficiency and PID efficiency with requirement on a hit in the SPD is consistent with unity. It reaches values around 1% for the most central events.

4.6.3 Signal extraction

A function for the description of residual background in the J/ψ signal extraction only approximates a true background distribution. The systematic uncertainty from the choice of the function is estimated by increasing by one the order of the polynomial used in the standard signal extraction configuration. The first-order polynomial is the standard case for the residual background description in almost all centrality and p_T intervals in this work. Therefore, the difference between the raw J/ψ yields using
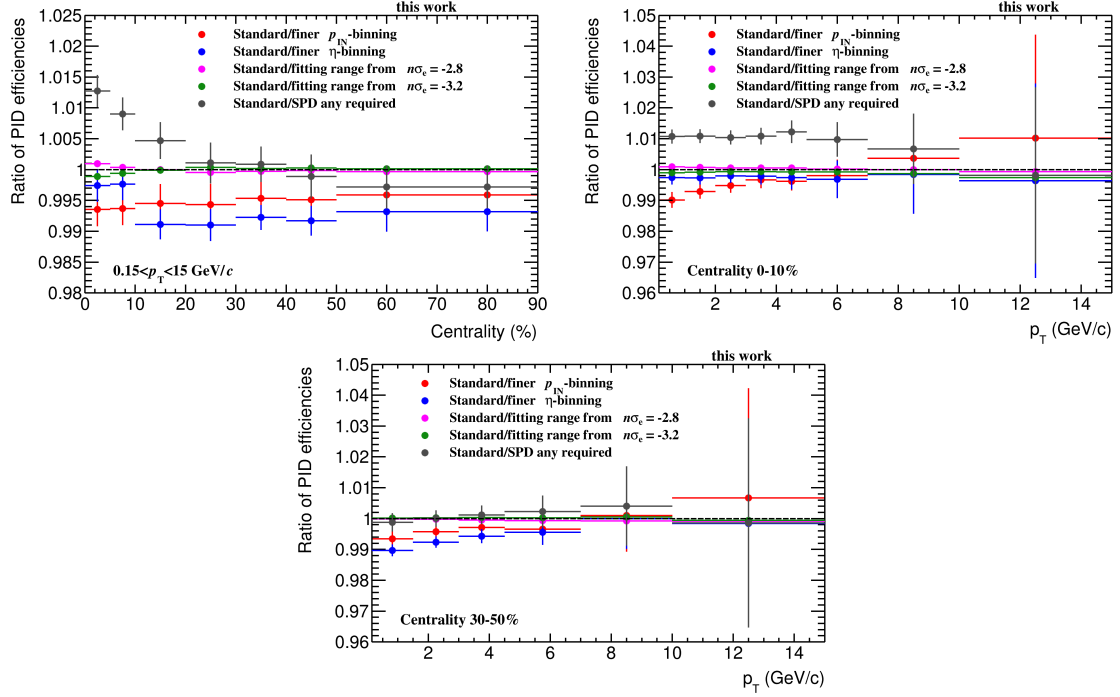
Figure 4.26: Ratios of the PID efficiency with standard settings to the PID efficiency using different settings for studies of systematic uncertainties. The ratios are shown as a function of centrality (top left) and p_T for centralities 0–10% (top right) and 30–50% (bottom).

either the first or second-order polynomial is assigned as the uncertainty. However, the second-order polynomial describes the residual background better for $2 < p_T < 3$ GeV/c in the p_T-differential analysis for centrality 0–10%. Therefore, it is used as the standard setting. The difference between the second and the third-order polynomial is assigned as the systematic uncertainty in this case. The extracted raw J/ψ yields per event from fits with different polynomial degrees are shown on the left of Figure 4.27, the relative differences between raw yields extracted using different polynomial degrees are on the right of the same figure. The relative difference between the standard and higher order case is typically below 5%. Larger differences are found for cases with more challenging residual background shapes or with low J/ψ yields.

The systematic uncertainty due to the choice of the fit range for J/ψ signal extraction is also considered. The fit range for signal extraction is modified such that low and high invariant mass edges are changed simultaneously to obtain a broader or a tighter fit range. The fit interval edges for the event mixing procedure are changed correspondingly. The considered fit ranges are:

- 2.0–3.7 GeV/c^2 (standard fit range),
- 1.76–3.94 GeV/c^2 (broadest fit range),
- 1.84–3.86 GeV/c^2,
- 1.92–3.78 GeV/c^2,
- 2.08–3.62 GeV/c^2,
- 2.16–3.54 GeV/c^2 (tightest fit range).

They are chosen such that the ranges are not so broad that the fit function would miss the shape of the background nearby the J/ψ signal peak. On the other hand, the fit range is broad enough to well constrain the fit. The standard fit range for interval $0.15 < p_T < 1$ GeV/c in p_T-differential

73
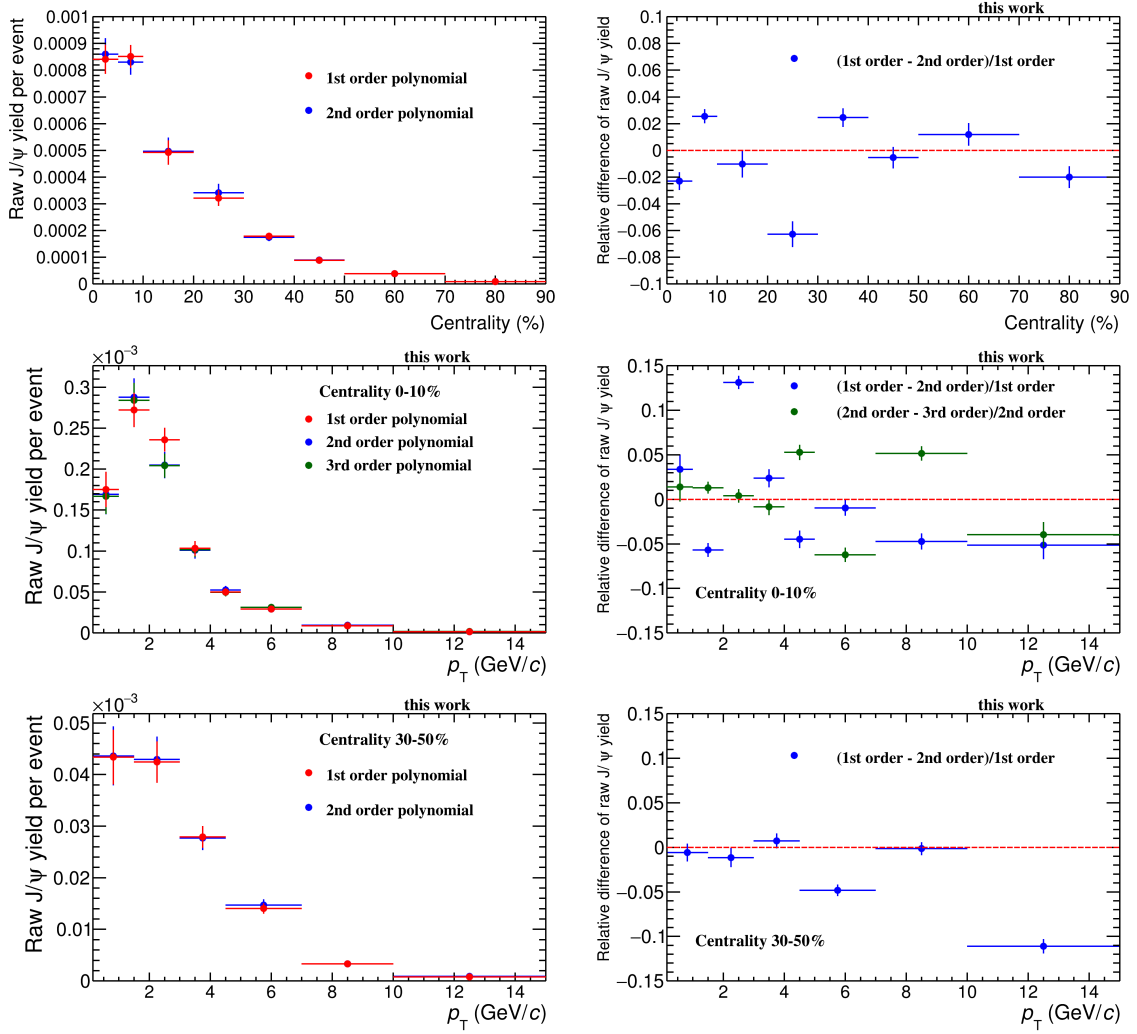
Figure 4.27: Raw J/ψ yield per event from fits with different polynomial degrees for the description of the residual background (left) and the ratio of the raw J/ψ yield obtained using different orders of polynomial function.

analysis of centrality class 0–10% is changed with respect to the rest of the intervals. The lower bound is shifted up to 2.4 GeV/c^2 in order to avoid the problematic low mass region as discussed in Section 4.4. Therefore, the configuration of the fit range variations for this case is different:

- 2.4–3.7 GeV/c^2 (standard fit range),

- 2.36–3.86 GeV/c^2 (broadest fit range),

- 2.44–3.66 GeV/c^2,

- 2.48–3.62 GeV/c^2,

- 2.52–3.58 GeV/c^2,

- 2.56–3.54 GeV/c^2 (tightest fit range).

The whole procedure is repeated in all centrality classes and p_T intervals used in this work. The intervals are not merged to suppress statistical fluctuations since the background shape and

74

composition change as a function of p_T and centrality. Examples of the fit range variations for the standard set of the track quality selection criteria are shown in Figure 4.28. The corrected J/ψ yield typically varies from the standard case up to a few percent. The final uncertainty is obtained using independent variations of the fit range and of the tracking selection criteria from Subsection 4.6.1. The latter changes a fraction of background in the invariant mass extraction and a background shape. Examples of results for simultaneous variations are shown in Figure 4.29. Means for fit range variations and fixed tracking selections are shown in black color. The error bars of means are calculated as the RMS from the case with the standard fit range. A distribution of the RMS for different fixed tracking selections is presented in Figure 4.30. The relative mean of the RMS distribution is assigned as systematic uncertainty. The systematic uncertainty values from the choice of the fit range range between 0.7 and 2.8% for all cases in this work.

The residual background in the J/ψ signal extraction in the measurement [152] is neglected as discussed in the Section 4.4. Thus, the same applies naturally to the systematic uncertainty from the choice of the function for the residual background description. The values of this uncertainty source are in this work estimated by the change of the polynomial degree as is discussed above. The systematic uncertainty due to the choice of the fit range is estimated in a similar way in both analyses.
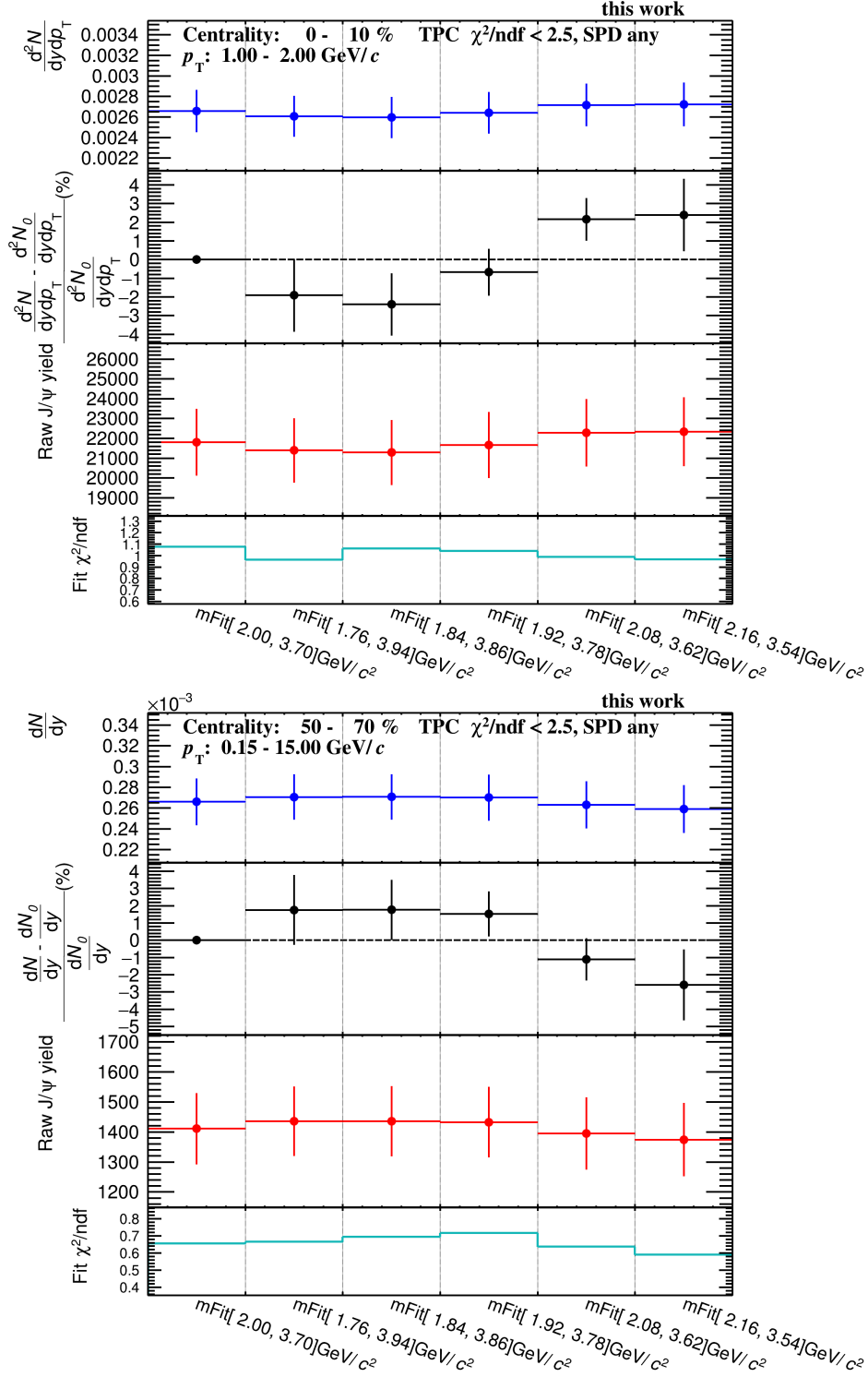
Figure 4.28: Corrected J/ψ yield, deviation from the standard case, J/ψ raw yield and fit χ^2/ndf as a function of the fit range variations. The first fit range is the standard one. The shown examples correspond to the standard tracking selection criteria. The examples correspond to the p_{T} range $1 < p_{\mathrm{T}} < 2$ GeV/c and the centrality class 0–10% (top) and the p_{T}-integrated case and the centrality class 50–70% (bottom).
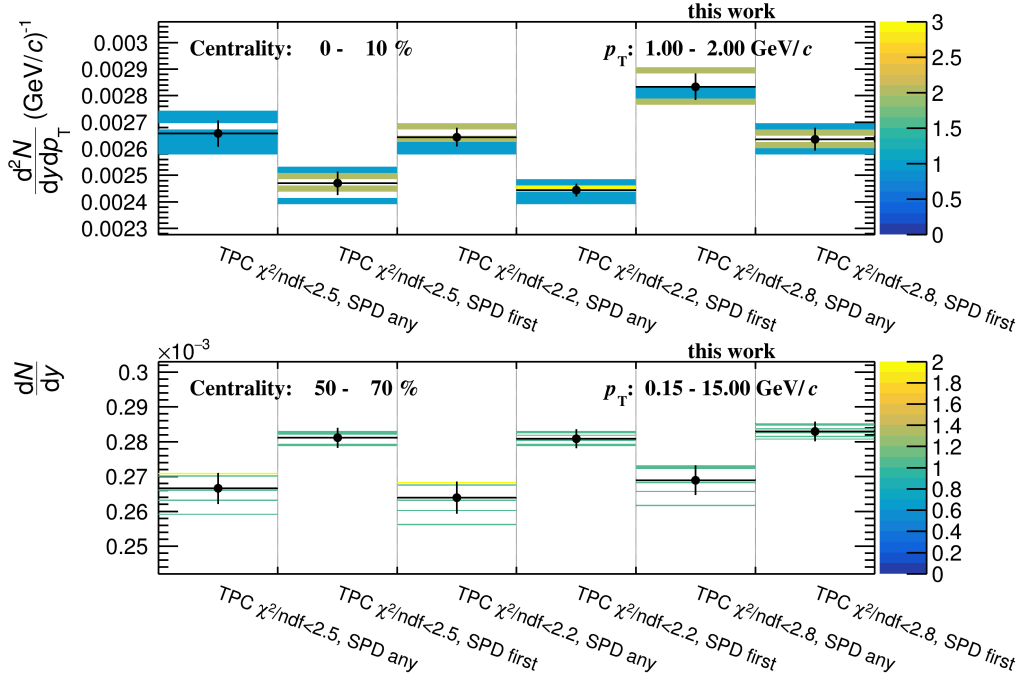
Figure 4.29: Examples of corrected J/ψ yield for simultaneous fit range and tracking cut variations and means of cases with different fit ranges for one set of tracking selections shown in black. Error bar on means is calculated as RMS with respect to the case of standard fit range. Color scale corresponds to the number of the variations falling into a bin of corrected J/ψ yield.
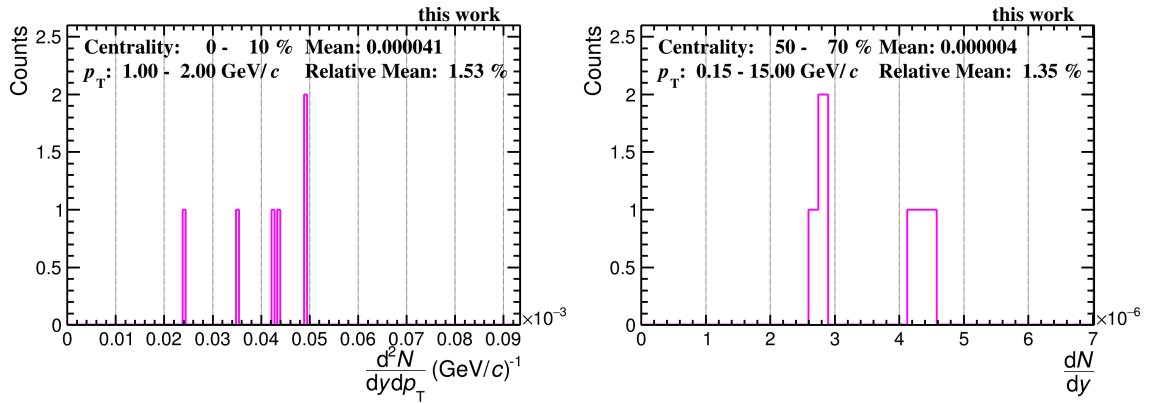
Figure 4.30: Distributions of RMS used for the estimation of systematic uncertainty originating from the choice of the fit range. Each entry corresponds to one tracking selection criterion. The shown examples of the distributions correspond to the p_{T} range $1 < p_{\mathrm{T}} < 2$ GeV/c and the centrality class 0–10% (top) and the p_{T}-integrated case and the centrality class 50–70% (bottom).

4.7 Improvements with respect to previous measurement in Pb–Pb at $\sqrt{s_{\mathrm{NN}}} = 5.02$ TeV

The improvements carried out in this work with respect to the previous measurement of the J/ψ production yield in Pb–Pb collisions at $\sqrt{s_{\mathrm{NN}}} = 5.02$ TeV [152] are summarized in this section. ALICE collected data samples at this collision energy in the years 2015 and 2018. The publication presents measurement using only the 2015 data sample. In this work, the data samples from both years are combined. The full data sample contains approximately eight times as much events as the 2015 data sample alone in the centrality class 0–10%, four times as much in the centrality class 30–50% and twice as much in the centrality classes 10–30% and 30–50%.

The full data sample allows to study the J/ψ production yield in finer centrality and p_{T} intervals. This is achieved while keeping the precision of the new measurement at a similar level as in the publication. Consequently, the centrality and p_{T} dependences are better revealed. The centrality dependence of the J/ψ production yield is studied in eight centrality classes compared to previous four. In the publication, the J/ψ p_{T} spectra are extracted in four p_{T} intervals in the range $0.15 < p_{\mathrm{T}} < 10$ GeV/c. In the same p_{T} region, the p_{T} spectra are newly measured in seven intervals in the centrality class 0–10% and in five intervals in the centrality class 30–50%. In addition to that, the measurement is extended up to 15 GeV/c.

There are numerous improvements of methods used in different steps of the data analysis. The most significant development represents the data-driven approach for the PID efficiency calculation. This method is not affected by an imperfect description of the PID selection criteria in the MC simulation. Therefore, the data driven PID efficiency is more precise than the previously used MC based one. The new method is validated by different tests. Obtained systematic uncertainty on the data driven PID efficiency ranges between 1.1 and 1.6% for the p_{T}-integrated measurement. The data-driven PID efficiency will be important as well for the J/ψ measurements at midrapidity carried out using abundant Run 3 data samples.

The methods of calculation of other systematic uncertainty sources are updated. In particular, the systematic uncertainty on the J/ψ tracking efficiency is now estimated more precisely. The systematic uncertainty on the ITS–TPC matching is newly propagated from the track level to the pair level. This uncertainty was previously investigated only via tracking selection criteria variation and subsequent repeating the analysis chain.

4.8 pp reference

The measurement of the inclusive J/ψ production cross section in pp collisions serves as an important reference to the measurement in Pb–Pb collisions. The inclusive J/ψ cross section in pp collisions is an essential component for the calculation of the nuclear modification factor. The inclusive J/ψ cross section at midrapidity in pp collisions at $\sqrt{s} = 5.02$ TeV needed as a reference in this work for constraining medium effects in Pb–Pb collisions is published by the ALICE Collaboration [66]. The measurement in pp collisions is carried out in the same rapidity interval $|y| < 0.9$ as is used in this work. This result is shown and discussed earlier in this thesis in Subsection 2.3.2. In the case of the total cross section, the value for cross section in the interval 0–0.15 GeV/c is subtracted from the published cross section giving the result used in this work for the p_{T}-integrated analysis: $\mathrm{d}\sigma/\mathrm{d}y = 5.59 \pm 0.22(\mathrm{stat.}) \pm 0.33(\mathrm{syst.}) \pm 0.12(\mathrm{luminosity})\mu\mathrm{b}$. The values used for the p_{T}-differential analysis in centrality class 0–10% and their uncertainties are shown in Table 4.7. The global uncertainty of 2.2% is not listed in the table. It is dominated by the uncertainty on the integrated luminosity of the pp data sample equal to 2.1%. All of the values with exception of the first and the last p_{T} intervals are taken from the publication. In the case of interval 0.15–1 GeV/c, the used value is obtained by subtraction from the published value for the interval 0–1 GeV/c as in the case of the total cross sections. An extrapolation was carried out within ALICE Collaboration due to lack of J/ψ signal in the collected pp collisions for p_{T} interval 10–15 GeV/c.

The extrapolation approach already used in previous works such as [161, 162, 159] exploits an observation that inclusive J/ψ p_{T} spectra in pp collisions at various energies follow the universal

function:

$$\frac{\langle p_\mathrm{T} \rangle}{\mathrm{d}\sigma/\mathrm{d}y} \cdot \frac{\mathrm{d}^2\sigma}{\mathrm{d}y\mathrm{d}p_\mathrm{T}} = \frac{2(n-1) \cdot B^2 \cdot p_\mathrm{T}/\langle p_\mathrm{T} \rangle}{(1 + B^2 \cdot (p_\mathrm{T}/\langle p_\mathrm{T} \rangle)^2)^n}, \tag{4.11}$$

where $B = \Gamma(3/2)\Gamma(n - 3/2)/\Gamma(n - 1)$. The mean transverse momentum $\langle p_\mathrm{T} \rangle$ and the total cross section $\mathrm{d}\sigma/\mathrm{d}y$ are measured. Thus, p_T-differential cross sections published by different experiments can be fitted by the universal function while only the parameter n is free. When the parameter n is known, $\mathrm{d}\sigma/\mathrm{d}y$ and $\langle p_\mathrm{T} \rangle$ from the ALICE measurement at 5.02 TeV are used to obtain the extrapolation function for the desired energy. The uncertainty on the extrapolation originates from uncertainties on uncertainties of the input p_T spectra, $\mathrm{d}\sigma/\mathrm{d}y$, $\langle p_\mathrm{T} \rangle$ and shape uncertainty of the fit function. The latter is estimated by the mean deviation of the data points from the resulting fit. The systematic uncertainty on the cross section extrapolation value for the interval $10 < p_\mathrm{T} < 15$ GeV/c is 13.3%. The precision of the performed extrapolation procedure is defined by a broad selection of used measurements. The parameter n of the universal fit function is obtained using the measurements from ALICE at midrapidity at 13 TeV [163] and at forward rapidity at 7, 8 and 13 TeV [164, 165, 166], CDF at midrapidity at 1.96 TeV [167], LHCb at forward rapidity at 7, 8, 13 TeV [168, 169, 170] and ATLAS [171] and CMS [172] at forward rapidity at 7 TeV. The mean transverse momentum $\langle p_\mathrm{T} \rangle$ and the total cross section $\mathrm{d}\sigma/\mathrm{d}y$ at midrapidity in pp collisions at 5.02 TeV [66] are used to extract the desired value of the extrapolation.

p_T (GeV/c)	0.15–1	1–2	2–3	3–4	4–5	5–7	7–10	10–15
$\mathrm{d}^2\sigma/\mathrm{d}p_\mathrm{T}\mathrm{d}y$ (nb)	908.6	1668.8	1316.2	795.1	484.8	206.7	59.4	6.8
Statistical uncertainty (nb)	90.8	131.0	116.0	77.7	53.8	23.0	10.1	0.0
Systematic uncertainty (nb)	47.5	91.0	74.9	45.8	27.1	13.2	4.1	0.9
Statistical uncertainty (%)	10.0	7.9	8.8	9.8	11.1	11.1	17.0	0.0
Systematic uncertainty (%)	5.2	5.5	5.7	5.8	5.6	6.4	6.9	13.3

Table 4.7: pp reference for p_T-differential analysis in the centrality class 0–10%: p_T-differential inclusive J/ψ cross section and its uncertainties in pp collisions at $\sqrt{s} = 5.02$ TeV taken from [66]. The global uncertainty (2.2%) is not included in this table. It is dominated by the uncertainty on integrated luminosity of the pp data set (2.1%). The values for $10 < p_\mathrm{T} < 15$ GeV/c are obtained by an extrapolation carried out with the ALICE Collaboration.

The p_T intervals used for centrality 30–50% do not coincide with the intervals in the publication [66]. Therefore, the analysis was carried out within the ALICE Collaboration again in desired p_T intervals. This approach has a better precision than adding values for finer intervals to get values for broader intervals.

p_T (GeV/c)	0.15–1.5	1.5–3	3–4.5	4.5–7	7–10	10–15
$\mathrm{d}^2\sigma/\mathrm{d}p_\mathrm{T}\mathrm{d}y$ (nb)	1207.4	1352.7	751.5	223.4	59.4	6.8
Statistical uncertainty (nb)	91.3	98.6	61.0	21.6	10.1	0.0
Systematic uncertainty (nb)	62.1	77.1	43.4	14.0	4.1	0.9
Statistical uncertainty (%)	7.6	7.3	8.1	9.7	17.0	0.0
Systematic uncertainty (%)	5.1	5.7	5.8	6.3	6.9	13.3

Table 4.8: pp reference for p_T-differential analysis in the centrality class 30–50%: p_T-differential inclusive J/ψ cross section and its uncertainties in pp collisions at $\sqrt{s} = 5.02$ TeV obtained by analysis presented in [66] in p_T intervals used in this work for p_T-differential spectra for the centrality class 30–50%. The global uncertainty (2.2%) is not included in this table. It is dominated by the uncertainty on integrated luminosity of the pp data set (2.1%). The values for $10 < p_\mathrm{T} < 15$ GeV/c are obtained by an extrapolation carried out with the ALICE Collaboration.

Results and discussion

The results obtained in this thesis are presented in this chapter. The inclusive J/ψ production yield at midrapidity $|y| < 0.9$ in Pb–Pb collisions at $\sqrt{s_{NN}} = 5.02$ TeV is shown in the Section 5.1. The J/ψ production yield is studied as a function of centrality and transverse momentum down to $p_T = 0.15$ GeV/c in the centrality classes 0–10% and 30–50%. A centrality dependence of the inclusive J/ψ modification factor R_{AA} is reported in Section 5.2. The p_T-differential inclusive J/ψ production yield and R_{AA} are discussed in detail in Section 5.3. In each of the two sections, the results, comparisons to other measurements and models are presented and discussed.

5.1 Inclusive J/ψ production yields in Pb–Pb collisions

The inclusive J/ψ production yield in this work is obtained using Equation 4.1. The J/ψ yield as a function of the mean number of participants $\langle N_{part} \rangle$ is presented in Figure 5.1. The statistical uncertainty on the yield is represented by the vertical error bars, whereas the systematic uncertainty is indicated by the boxes. The mean number of participants $\langle N_{part} \rangle$ evaluated by the Monte Carlo Glauber simulation [20] for the centrality intervals used in this work is provided earlier in Table 3.1.
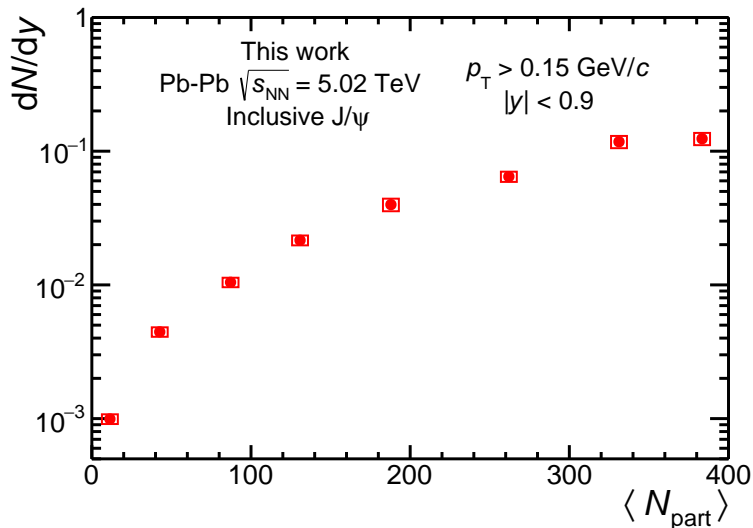
Figure 5.1: Inclusive J/ψ production yield in Pb–Pb collisions at $\sqrt{s_{NN}} = 5.02$ TeV as a function of the average number of participants $\langle N_{part} \rangle$. The values of $\langle N_{part} \rangle$ are obtained for collisions in centrality classes (0–5%, 5–10%, 10–20%, 20–30%, 30–40%, 40–50%, 50–70%, 70–90%). The vertical error bars indicate statistical uncertainty and the boxes around the data points represent the systematic uncertainty.

The inclusive J/ψ yield in Pb–Pb collisions increases towards central events. The J/ψ production

is in first order proportional to the number of binary nucleon-nucleon collisions N_{coll}. This is expected since the $c\bar{c}$ cross section in nuclear collisions is proportional to N_{coll}.

The p_{T}-differential J/ψ production yields for the centrality intervals 0–10% and 30–50% are shown in Figure 5.2. They are calculated using Equation 4.2. The uncertainties are indicated by the same way as in the case of the centrality dependence. For both centrality classes, the J/ψ production yield increases from the first studied p_{T} interval (0.15–1 GeV/c for 0–10%, 1.5–3 GeV/c for 30–50%) to the second interval (1–2 GeV/c for 0–10%, 1.5–3 GeV/c for 30–50%). At higher p_{T}, the J/ψ production yield decreases towards high p_{T}. Slopes of the observed p_{T} spectra can be studied for example via the measurement of the mean transverse momentum $\langle p_{\mathrm{T}}\rangle$, which is carried out using the 2015 data set at $\sqrt{s_{\mathrm{NN}}} = 5.02$ TeV in scope of an earlier publication [152].
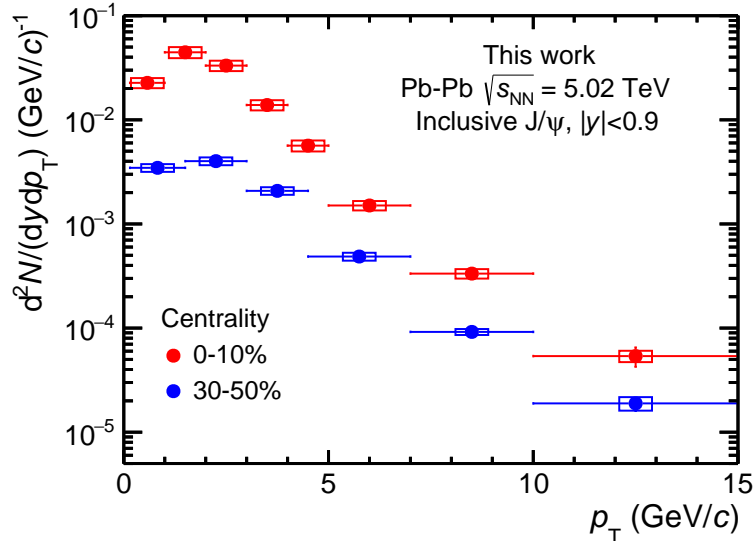
Figure 5.2: Transverse momentum dependence of the inclusive J/ψ production yields for the centrality classes 0–10% and 30–50%. The vertical error bars indicate statistical uncertainty and the boxes around the data points represent the systematic uncertainty.

5.2   Inclusive J/ψ R_{AA} as a function of centrality

The p_{T}-integrated inclusive J/ψ nuclear modification factor R_{AA} is obtained as a function of centrality using Equation 4.3. The result is shown in Figure 5.3. Obtained values of the J/ψ R_{AA} and corresponding uncertainties are listed in Table 5.1. The statistical uncertainty is indicated by the vertical bars. The systematic uncertainty is shown by the boxes. It is calculated by adding in quadrature the systematic uncertainty on the inclusive J/ψ production yields in Pb–Pb collisions and the uncertainty on the average nuclear overlap function $\langle T_{\mathrm{AA}}\rangle$. The uncertainty on the yields is approximately 10% and dominates over the $\langle T_{\mathrm{AA}}\rangle$ uncertainty ranging between 0.1% for the most central collisions and 1.7% for the peripheral events. The global systematic uncertainty represented by the box around unity originates from the uncertainty on the J/ψ cross section in pp collisions discussed in Section 4.8.

The J/ψ R_{AA} shows a decreasing trend as a function of $\langle N_{\mathrm{part}}\rangle$ up to $\langle N_{\mathrm{part}}\rangle \approx 90$ (centrality 40–50%). Whereas the J/ψ R_{AA} is consistent with unity for the centrality interval 70–90%, the R_{AA} for the centrality class 40–50% indicates suppression of the J/ψ production in Pb–Pb collisions with the significance of 3.4σ. For $\langle N_{\mathrm{part}}\rangle \gtrsim 90$, the measurement hints at an increasing trend of the R_{AA} towards unity.

The increased statistics of the used data sample compared to [152] allows to study the J/ψ R_{AA} as a function of centrality using smaller granularity of the centrality intervals. The publication
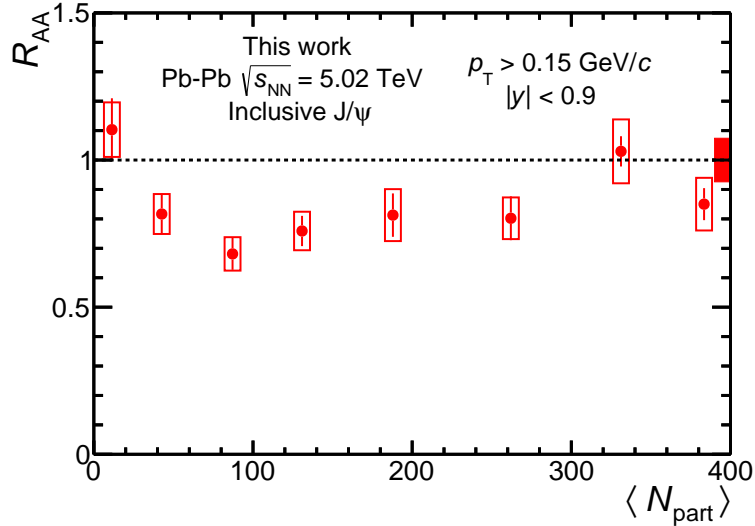
Figure 5.3: Inclusive J/ψ nuclear modification factor R_{AA}, integrated over p_T, as a function of $\langle N_{part} \rangle$. Vertical bars indicate statistical uncertainty, the boxes around the data points represent the systematic uncertainties on J/ψ yield in Pb–Pb collisions and the average nuclear overlap function $\langle T_{AA} \rangle$. The box around unity show global uncertainty originating from the uncertainty on the J/ψ cross section in pp collisions.

Centrality (%)	0–5	5–10	10–20	20–30	30–40	40–50	50–70	70–90
$\langle N_{part} \rangle$	383.4	331.2	262.0	187.9	130.8	87.1	42.7	11.3
$\langle N_{part} \rangle$ uncertainty	0.6	1.0	1.1	1.3	1.3	0.93	0.72	0.19
R_{AA}	0.850	1.030	0.802	0.813	0.759	0.681	0.817	1.103
R_{AA} statistical uncertainty	0.054	0.051	0.074	0.074	0.051	0.054	0.069	0.107
R_{AA} systematic uncertainty	0.089	0.109	0.071	0.088	0.065	0.057	0.068	0.093
R_{AA} global uncertainty	0.063	0.076	0.059	0.060	0.056	0.050	0.061	0.082

Table 5.1: Inclusive J/ψ nuclear modification factor R_{AA}, integrated over p_T, for different centrality classes. The mean number of participants $\langle N_{part} \rangle$ in the centrality classes is taken from [20].

presented the J/ψ R_{AA} obtained in five centrality intervals, whereas it is eight intervals for the measurement carried out in this thesis. In the publication, the hint of an increase in comparison to lower centrality can be concluded only for $\langle N_{part} \rangle \approx 260$.

5.2.1 Comparisons with other measurements

Firstly, the comparison of measurements in different rapidity ranges is discussed. The presented result at midrapidity is compared to the J/ψ R_{AA} at forward rapidity. The inclusive J/ψ nuclear modification factor R_{AA} at midrapidity is compared with the ALICE measurement at forward rapidity using the dimuon decay channel [173] in Figure 5.4. The J/ψ R_{AA} at forward rapidity is obtained in three rapidity classes: $2.5 < y < 3.0$, $3.0 < y < 3.5$ and $3.5 < y < 4.0$. The statistic, systematic and global error bars are indicated in the figure as described in the previous section. The J/ψ R_{AA} at forward rapidity shows a similar trend as the J/ψ R_{AA} at midrapidity up to $\langle N_{part} \rangle \approx 90$ (centrality 40–50%). A clear suppression at forward rapidity fairly independent of the centrality is observed for $\langle N_{part} \rangle \gtrsim 130$ (centrality larger than about 40%). There is no strong rapidity dependence of the J/ψ R_{AA} at forward rapidity.

A comparison of the J/ψ R_{AA} at midrapidity and at forward rapidity interval $3.5 < y < 4.0$ suggests an enhancement of the J/ψ production compared to expectations based on pp collisions towards midrapidity in collisions with the centrality above approximately 40%. This points to a

larger (re)generation contribution to the J/ψ production due to a larger charm quark density at midrapidity.

When comparing the published results at same collision energy [152] at midrapidity to the measurement at forward rapidity in rapidity interval $3.5 < y < 4.0$, a hint of an increase could be seen for two broad centrality intervals 0–10% and 20–40%. In this work, the comparison hints at an increase in five centrality intervals in total (0–5%, 5–10%, 10–20%, 20–30%, 30–40%).
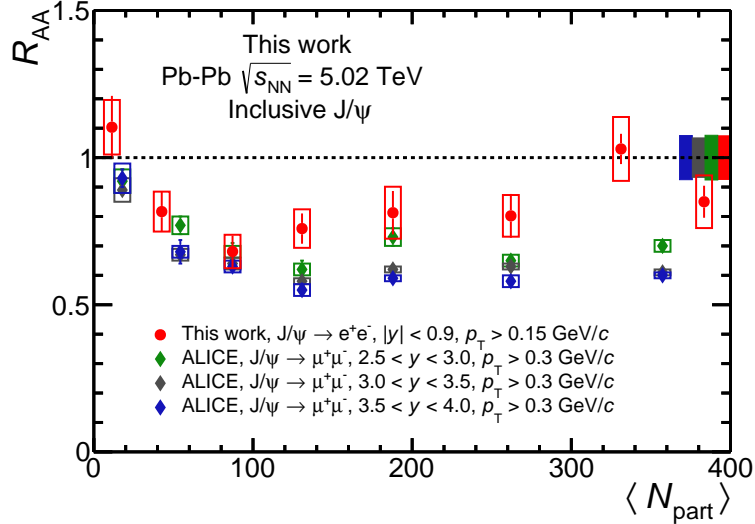
Figure 5.4: Inclusive J/ψ nuclear modification factor R_{AA} in Pb–Pb collisions at $\sqrt{s_{NN}} = 5.02$ TeV as a function of $\langle N_{part} \rangle$ at midrapidity ($|y| < 0.9$) and at forward rapidity for three rapidity intervals ($2.5 < y < 3.0$, $3.0 < y < 3.5$ and $3.5 < y < 4.0$) [173].

In this paragraph, the energy dependence is discussed. The inclusive J/ψ nuclear modification factor R_{AA} as a function of the charged-particle density at midrapidity $\mathrm{d}N_{ch}/\mathrm{d}\eta|_{\eta=0}$ is shown in Figure 5.5. It is compared to the ALICE measurement at $\sqrt{s_{NN}} = 2.76$ TeV and the PHENIX measurement at $\sqrt{s_{NN}} = 0.2$ TeV. All the measurements are performed at midrapidity. The $\mathrm{d}N_{ch}/\mathrm{d}\eta|_{\eta=0}$ reflects the density of the medium created in heavy-ion collisions. The suppression of the J/ψ meson production due to the color screening in the deconfined medium should be proportional to the $\mathrm{d}N_{ch}/\mathrm{d}\eta|_{\eta=0}$ rather than $\langle N_{part} \rangle$. Therefore, the dependence on the $\mathrm{d}N_{ch}/\mathrm{d}\eta|_{\eta=0}$ is chosen for this comparison between the measurements at different collision energies.

The measurements at the two LHC energies are consistent with each other. At $\mathrm{d}N_{ch}/\mathrm{d}\eta|_{\eta=0} \lesssim 300$, the J/$\psi$ R_{AA} shows a similar decreasing trend at the highest and lowest presented energies. The J/ψ R_{AA} at $\sqrt{s_{NN}} = 0.2$ TeV continues in decreasing also for larger $\mathrm{d}N_{ch}/\mathrm{d}\eta|_{\eta=0}$ due to the J/ψ suppression in the QGP. On the other hand, the J/ψ R_{AA} at the larger LHC energies does not follow this trend, which can be attributed to significantly larger (re)generation contribution at the LHC.

5.2.2 Model comparisons

In Figure 5.6, the inclusive J/ψ nuclear modification factor R_{AA} as a function of centrality is compared to model calculations of the statistical hadronization model (SHM) [101], the transport models TM1 [105] and TM2 [106], and the comover interaction model (CIM) [108]. Models are shown as colored bands. The width of the bands represents the model uncertainties. The model calculations are discussed earlier in more details in Section 2.6. They all consider some contribution from (re)generation. However, specific model assumptions and implementations are different.

The SHM assumes that the charm quarks are thermalized and J/ψ mesons are formed at the phase boundary. Temperature and the fireball volume at chemical freeze-out are fixed from the fit
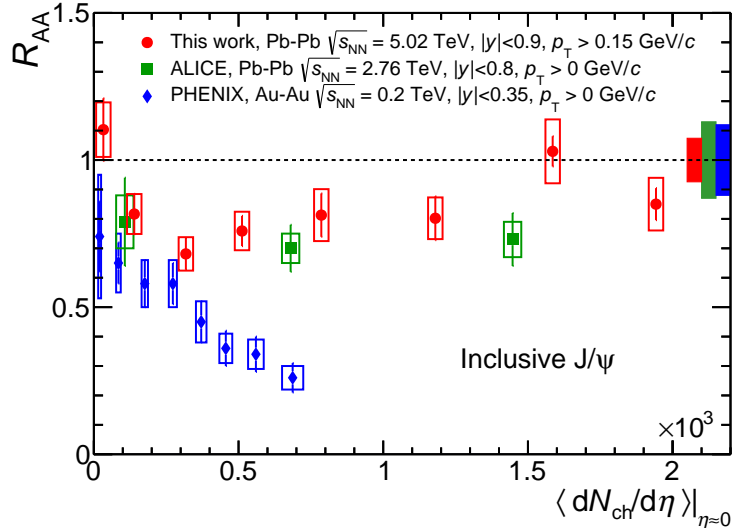
Figure 5.5: Inclusive J/ψ R_{AA} at midrapidity as a function of the midrapidity charged-particle density dN_{ch}/d$\eta|_{\eta=0}$ measured in Pb–Pb collisions at $\sqrt{s_{NN}}$ = 5.02 TeV and at $\sqrt{s_{NN}}$ = 2.76 TeV [174] and in Au–Au collisions at $\sqrt{s_{NN}}$ = 0.2 TeV [97]. Values of dN_{ch}/d$\eta|_{\eta=0}$ are taken from [175] for $\sqrt{s_{NN}}$ = 5.02 TeV, from [176] for $\sqrt{s_{NN}}$ = 2.76 TeV and from [177] for $\sqrt{s_{NN}}$ = 0.2 TeV.

of the SHM to the measured light-flavor hadron yields. The only remaining parameter of the model is the c$\bar{c}$ cross section defining the number of c$\bar{c}$ pairs produced during the hard scatterings. It is discussed in more details below.

The transport models TM1 and TM2 consider J/ψ formation already during the QGP phase. The medium evolution is described by a hydrodynamic modeling. Continuous charmonium (re)generation and dissociation are governed by the Boltzmann equation. Whereas incomplete charm quark thermalization is assumed in the framework of the TM1, the TM2 calculations assume thermalized charm quark distribution.

In the CIM, J/ψ mesons are dissociated via interactions with a comoving hot partonic medium. The dissociation and (re)generation terms are considered in a rate equation. The J/ψ dissociation rate is proportional to the density of comoving medium and the dissociation cross section is obtained from fits to low energy data. The (re)generation term is proportional to the squared charm quark density. The (re)generation cross section is assumed to be identical with the dissociation cross section.

An essential input to all of the discussed model calculations is the c$\bar{c}$ cross section at midrapidity in Pb–Pb collisions at $\sqrt{s_{NN}}$ = 5.02 TeV, which has not been measured up to now. In the models, this parameter is obtained in the following way. The measurement of the c$\bar{c}$ cross section in pp collisions is reduced by a shadowing factor and scaled by the mean number of binary nucleon-nucleon collisions $\langle N_{coll} \rangle$ in order to get the c$\bar{c}$ cross section for different centrality classes. Shadowing in the SHM is considered using rapidity-dependent measurements of the D-meson nuclear modification factor in p–Pb collisions [178]. Interpolation of the measurements is done via model calculations [179, 180, 181]. The shadowing factors in TM1 and TM2 are based on the EPS09 NLO calculations [179]. In the CIM, they are taken into account using the EPS09 LO calculations [182]. The c$\bar{c}$ cross section in pp collisions at midrapidity at $\sqrt{s}$ = 5.02 TeV [183] was not available yet when model calculations were provided. Thus, the model calculations use different estimates of the c$\bar{c}$ cross section in pp based on measurements at different energies and rapidity intervals.

The values of the c$\bar{c}$ cross section per nucleon-nucleon collision after including the shadowing effect considered in the model calculations are 0.53 ± 0.10 mb (uncertainty 18%) for the SHM, 0.92 ± 0.12 mb (uncertainty 13%) for the TM1, 0.78 ± 0.09 mb (uncertainty 11%) for the TM2 and 0.56 ± 0.11 mb (uncertainty 20%) for the CIM. Sizable differences between these values affect as well

differences between values of model predictions.

Considering large model uncertainties, the SHM and the TM1 are in agreement with the measurement, although the data points are close to the upper band of TM1. The centrality dependence shown by the data points with a dip around $\langle N_{\mathrm{part}} \rangle = 90$ is shown as well by the model predictions. This is not apparent from the comparison of the previous measurement [152] using coarser centrality binning and the model predictions. The TM2 undershoots the data points in peripheral collisions and approaches them in more central events. The CIM is in good agreement with the measurement in the peripheral and semi-central events and tends to underestimate it in the most central events. Precise physics conclusions cannot be made due to the large model uncertainties, discrepancies between the model input parameters and the measurement uncertainty.
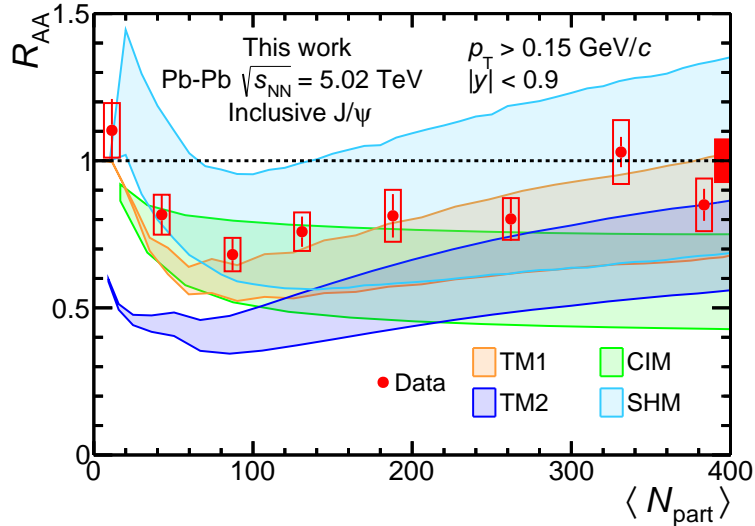
Figure 5.6: Inclusive J/ψ nuclear modification factor R_{AA} in Pb–Pb collisions at $\sqrt{s_{\mathrm{NN}}} = 5.02$ TeV compared to the model calculations of the comover interaction model (CIM) [108], the statistical hadronization model (SHM) [101] and two transport models TM1 [105] and TM2 [106].

The $c\bar{c}$ cross section in pp collisions at midrapidity at $\sqrt{s} = 5.02$ TeV [183] has been recently published by ALICE. The published value of the $c\bar{c}$ cross section per unit of rapidity is $\mathrm{d}\sigma_{c\bar{c}}^{\mathrm{pp}}/\mathrm{d}y = 1.165^{+0.140}_{-0.110}$ mb when adding up all uncertainties. However, the results of the theoretical calculations compared to the measurement presented in this work have not been updated yet at the time writing of this thesis. The differences between model inputs complicate drawing conclusions on the phenomenology of the J/ψ production from comparisons between models and measurements. Therefore, it would be beneficial for the future to agree on a common model input value based on available experimental results, including uncertainties. The mentioned ALICE measurement at 5.02 TeV in pp collisions represents an opportunity for the input unification at midrapidity. For example, when considering the shadowing factor 0.65 ± 0.12 used in the SHM framework [184], the resulting value $\mathrm{d}\sigma_{c\bar{c}}/\mathrm{d}y = 0.76^{+0.17}_{-0.16}$ mb could be used. This would lead to a reduction of the (re)generation contribution in TM1 and its enhancement in the SHM and the CIM. Nevertheless, when comparing model predictions based on this input value to the measurement presented in this work, it would be most probably not yet sufficient to draw a conclusion on that whether the (re)generation takes place already during the QGP phase or solely at the phase boundary.

5.3 Inclusive J/ψ production yields and R_{AA} as a function of transverse momentum

The p_T-differential nuclear modification factor R_{AA} in the most central events (0–10%) and semi-central events (30–50%) is presented in this section. Comparisons of model calculations to the J/ψ R_{AA} and production yields are discussed.

The inclusive J/ψ nuclear modification factor R_{AA} in Pb–Pb collisions at $\sqrt{s} = 5.02$ TeV as a function of p_T is shown in Figure 5.7. The vertical bars indicate the statistical uncertainty, whereas the boxes around the data points represent the systematic uncertainty. In both cases, the uncertainty is calculated by adding in quadrature the uncertainty on the J/ψ production yield in Pb–Pb collisions and the uncertainty on the inclusive p_T-differential J/ψ cross section in pp collisions at $\sqrt{s} = 5.02$ TeV. The boxes around unity represent the global uncertainty originating from the integrated luminosity of the pp data sample and the mean nuclear overlap function $\langle T_{AA} \rangle$.

The J/ψ R_{AA} in the centrality class 0–10% is consistent within error bars with unity up to $p_T = 3$ GeV/c, whereas the R_{AA} in the centrality class 30–50% shows suppression of the J/ψ production in Pb–Pb collisions in the full examined p_T region. The difference between the results for the two centrality classes at low p_T suggests a larger contribution of (re)generation to the J/ψ production in the most central events compared to the semi-central events. For $3 < p_T < 10$ GeV/c, the R_{AA} shows a decreasing trend, which is steeper in the centrality class 0–10% compared to 30–50%. The large suppression at high p_T is caused by the color screening of the c$\bar{c}$ potential and/or energy loss of charm quarks in the deconfined medium.
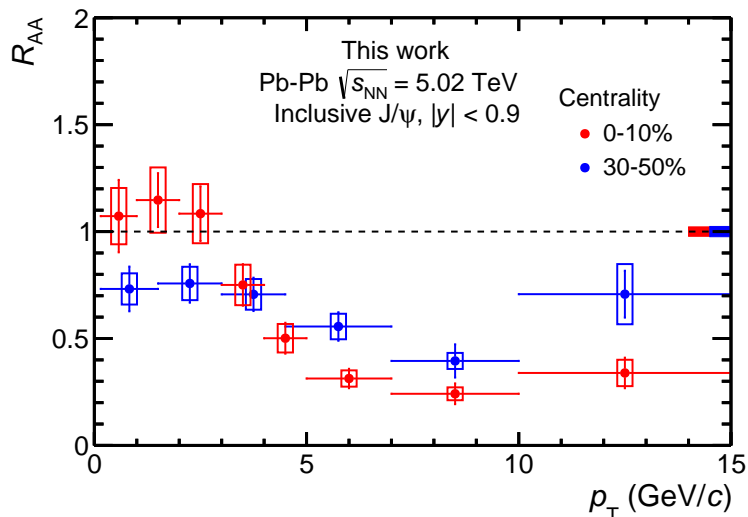
Figure 5.7: Inclusive J/ψ nuclear modification factor R_{AA} in Pb–Pb collisions at $\sqrt{s_{NN}} = 5.02$ TeV as a function of p_T in the centrality classes 0–10% and 30–50%. The vertical bars indicate the statistical uncertainty, whereas the boxes around the data points indicate the systematic uncertainty. In both cases, the uncertainties on the J/ψ production yield in Pb–Pb collisions and the pp reference are added. The box around unity represents the global uncertainty originating from the integrated luminosity of the pp data sample and the mean nuclear overlap function $\langle T_{AA} \rangle$.

The previous results at $\sqrt{s_{NN}} = 5.02$ TeV [152] are obtained in three centrality classes: 0–20%, 20–40% and 40–90%. The p_T-differential J/ψ R_{AA} is measured in the interval $0.15 < p_T < 10$ GeV/c, which is divided into four bins. In this thesis, seven and five intervals are used in the same p_T region in the centrality classes 0–10% and 30–50%, respectively. Furthermore, the studied kinematic region is extended newly up to 15 GeV/c. In the publication, the data points in the centrality classes 0–20%, 20–40% and 40–90% are consistent within error bars for $p_T < 3$ GeV/c. The only exception is the interval $1.5 < p_T < 3$ GeV/c in the centrality class 40–90%, where the measurement suggests

decrease of the J/ψ R_{AA} with respect to the other studied centrality classes. On the other hand, the results in this work show ordering of the J/ψ R_{AA} values for the examined centrality classes in the interval $0.15 < p_T < 3$ GeV/c as discussed above.

5.3.1 Comparisons with other measurements

The inclusive J/ψ nuclear modification factor R_{AA} as a function of p_T at midrapidity in the centrality class 0–10% is compared to the measurement at forward rapidity ($2.5 < y < 4.0$) in the centrality class 0–20%. The J/ψ R_{AA} in both rapidity intervals shows similar trend as a function of p_T. However, the p_T-dependence at forward rapidity is shallower. Both measurements are compatible within uncertainties above $p_T = 4$ GeV/c. The comparison between the measurements for $p_T < 4$ GeV/c, where the contribution of the (re)generation component is expected to dominate, suggests larger J/ψ R_{AA} at midrapidity compared to forward rapidity. This behavior is expected due to a larger charm quark density at midrapidity [185].
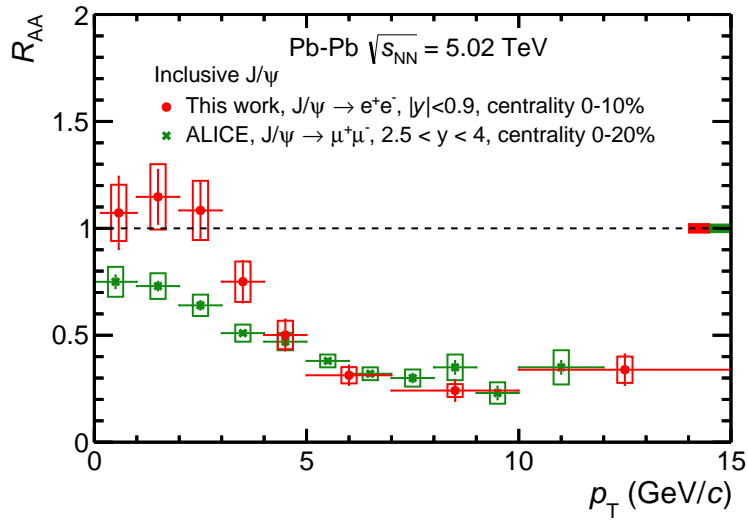
Figure 5.8: Inclusive J/ψ nuclear modification factor R_{AA} in the most central Pb–Pb collisions at $\sqrt{s} = 5.02$ TeV as a function of p_T at midrapidity ($|y| < 0.9$) and forward rapidity ($2.5 < y < 4.0$) [173].

The J/ψ R_{AA} for centrality 0–20% [152] obtained using coarser p_T intervals than in this work shows increase at midrapidity with respect to forward rapidity up to $p_T = 5$ GeV/c. The interval $3 < p_T < 5$ GeV/c used in the publication is split in this work to two p_T intervals. This allows to conclude that the results at different rapidities are consistent within uncertainties already from $p_T = 4$ GeV/c as discussed above.

5.3.2 Model comparisons

The inclusive J/ψ production yield and R_{AA} as a function of p_T in the centrality class 0–10% are compared to the model calculations in Figure 5.9. Both models are in a very good agreement with the measurements for $p_T < 4$ GeV/c, where both model calculations predict sizable contribution to the J/ψ production from (re)generation. At higher p_T, the TM1 describes well the measurement, whereas the SHM model underestimates it.

The same observables measured in the centrality interval 30–50% are compared to the model calculations in Figure 5.10. The TM1 tends to underestimate the J/ψ R_{AA} in the interval $3 < p_T < 7$ GeV/c. The SHM is in good agreement with the measurement up to $p_T = 4.5$ GeV/c and undershoots it at higher p_T.
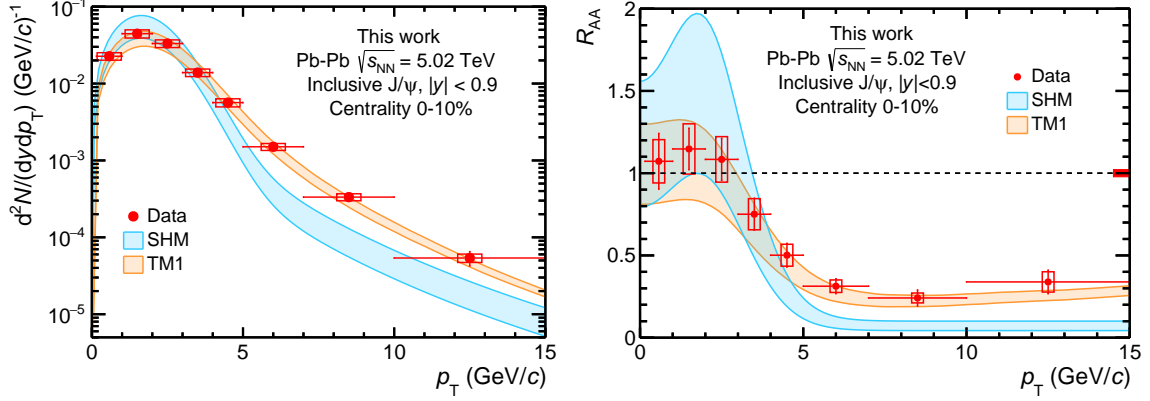
Figure 5.9: Inclusive J/ψ production yield (left) and R_{AA} (right) as a function of p_T in Pb–Pb collisions in the centrality class 0–10%. The measurement is compared to the model calculations of the SHM [101] and the TM1 [105].
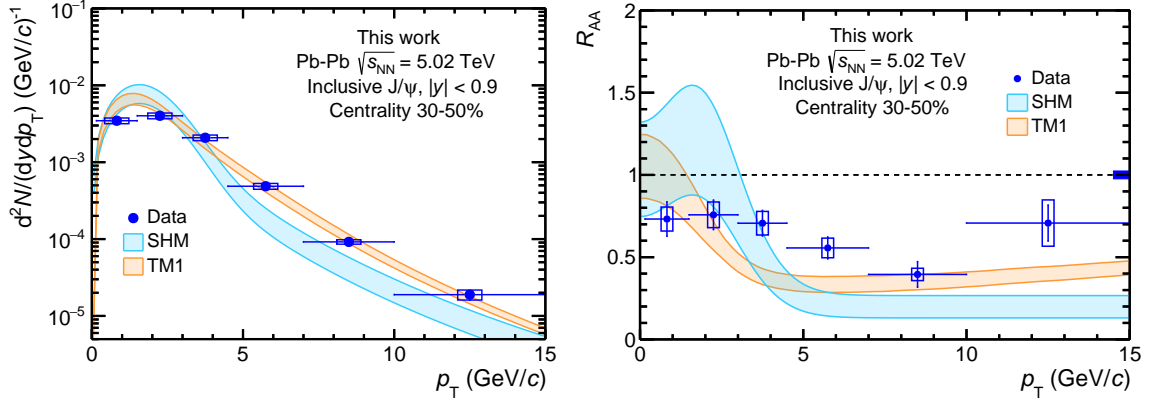
Figure 5.10: Inclusive J/ψ production yield (left) and R_{AA} (right) as a function of p_T in Pb–Pb collisions in the centrality class 30–50% compared to the model calculations of the SHM [101] and the TM1 [105].

5.3.3 Summary

The inclusive J/ψ production at midrapidity in Pb–Pb collisions at $\sqrt{s_{NN}} = 5.02$ TeV is presented as a function of centrality and p_T. The p_T-differential measurement is carried out in the central (0–10%) and semi-central collisions (30–50%).

Smaller granularity of centrality intervals in comparison to [152] used for the measurement in this thesis allows to better explore the centrality dependence of the J/ψ R_{AA}. The measurement presented in this thesis shows an increase towards the most central events from the centrality around 40%. This conclusion could be made only for the centrality above 20% in the case of [152].

The p_T-differential J/ψ R_{AA} for the centrality class 30–50% suggests a decrease in comparison to the centrality class 0–10% at $p_T < 3$ GeV/c. This points to a larger (re)generation contribution to the J/ψ production at low p_T in the most central collisions compared to semi-central collisions. In the same p_T region, the J/ψ R_{AA} values for different examined centrality classes (0–20%, 20–40% and 40–90%) do not show an ordering with respect to each other.

The J/ψ R_{AA} values as a function of centrality are higher at midrapidity compared to forward rapidity (3.5 < y < 4.0) for the centrality range 0–40%. The p_T dependence of the J/ψ R_{AA} for the centrality class 0–10% is newly examined in seven p_T intervals in 0.15 < p_T < 10 GeV/c. Four intervals are used in [152] for the same p_T range. The measurement is newly extended up

to $p_T = 15$ GeV/c. In the most central collisions, the measurement in finer p_T intervals allows to conclude that the J/ψ R_{AA} at midrapidity suggests an increase in comparison to forward rapidity for $p_T < 4$ GeV/c. The two measurements are consistent within uncertainties at higher p_T. The discussed comparisons of measurements at different rapidity ranges as a function of centrality and p_T support picture of stronger (re)generation due to a larger charm quark density at midrapidity compared to forward rapidity.

The J/ψ R_{AA} and production yields are compared to the model calculations. The transport approach TM1 and the SHM are in agreement with the J/ψ R_{AA} obtained as a function of centrality over full centrality range considered. At low p_T, both models predict a significant contribution of (re)generation to the J/ψ production compensating fully or to a large extent the suppression due to the color screening. This leads to the large J/ψ production yields and R_{AA} at low p_T, which is in agreement with the presented measurements.

Conclusion and outlook

The J/ψ meson in heavy-ion collisions serves as a probe of the state of deconfined strongly interacting matter called the quark-gluon plasma. Free color charges in the deconfined medium can prevent the formation of J/ψ mesons due to the color screening of the c$\bar{c}$ potential. This leads to a suppression of the J/ψ production yields in heavy-ion collisions with the QGP stage. At large collision energy such as the LHC energy, the density of charm quarks and anti-quarks in the deconfined medium leads to a significant contribution of (re)generation to the J/ψ production.

The inclusive J/ψ production yield and nuclear modification factor R_{AA} at midrapidity are measured in Pb–Pb collisions collected by ALICE at $\sqrt{s_{\mathrm{NN}}} = 5.02$ TeV. The results are presented as a function of collision centrality and transverse momentum down to $p_{\mathrm{T}} = 0.15$ GeV/c. Low p_{T} J/ψ production at midrapidity studied uniquely at the LHC by ALICE is especially interesting, since (re)generation is expected to have the most significant effect on the J/ψ production in this kinematic region. The J/ψ invariant mass distribution is build from electron candidates selected such that background contamination is reduced while preserving as much efficiency as possible. The extracted J/ψ yields are corrected on the efficiency of electron candidate selections. The efficiency of the particle identification selections is newly data driven, which allows to obtain it with a higher precision compared to previous J/ψ production measurements in Pb–Pb collisions at midrapidity performed by ALICE. The new method underwent various tests. Systematic uncertainty of the J/ψ production yield is carefully studied using state-of-the-art techniques.

The measurement of the J/ψ production at $\sqrt{s_{\mathrm{NN}}} = 5.02$ TeV has been already published in [152]. However, the results in the publication are obtained only using part of the nowadays available data sample. The full data sample used in this work allows to study the J/ψ production yields as a function of centrality and p_{T} in finer intervals. Thus, the centrality and p_{T} dependences are better revealed compared to the measurement in the publication. The inclusive J/ψ production yield and nuclear modification factor R_{AA} presented in this theses are internally reviewed and approved for publication by the ALICE Collaboration. The publication is in preparation.

The measured J/ψ R_{AA} as a function of centrality shows a hint of an increasing trend from the semi-central to the most central collisions. On the other hand, the J/ψ R_{AA} at the lower RHIC energy decreasing towards central collisions is in a clear contrast to this finding. Comparisons of the p_{T}-differential and centrality dependent R_{AA} at midrapidity to the measurement at forward rapidity suggests larger (re)generation at low p_{T} at midrapidity compared to forward rapidity due to a larger charm quark density. The J/ψ R_{AA} at midrapidity in the most central collisions hints at increase of (re)generation component compared to the semi-central collisions at low p_{T}. A similar conclusion could not be made in [152] when comparing p_{T}-differential results in different centrality classes. At large p_{T}, J/ψ is suppressed due to color screening and/or energy loss of charm quarks in the deconfined medium. The J/ψ R_{AA} can be reasonably well described for all centrality classes and at low p_{T} by two approaches considering (re)generation–transport and statistical hadronization models. Large uncertainties of the model calculations, sizable differences between important common model inputs and the uncertainty of the measurement leave the question of the exact J/ψ production phenomenology open. Steps forward on the theory side could be pursued already now by unifying important model input values. In summary, the presented measurement strongly supports picture of (re)generation as an important J/ψ production mechanism at low p_{T} at the LHC energy especially

significant at midrapidity. Charm quarks are created almost exclusively during hard scatterings at the beginning of a heavy-ion collision due to their large masses. Subsequently, they interact with the deconfined medium surrounding them and can be bound in J/ψ mesons already during the QGP phase and/or at the phase boundary. Whether J/ψ mesons are formed already during the QGP evolution or solely at the phase boundary is not clear yet.

A major upgrade of the ALICE detector opens an opportunity to improve the precision of presented measurements and study probes of the QGP not accessible yet. The upgrade of the TPC detector will allow continuous readout. Thus, the full future collision rate of 50 kHz will be employed leading to the collection of a 50–100 larger data sample of Pb–Pb collisions in comparison to Run 2. Tracking performance will be improved by the upgraded ITS detector due to an increased granularity and a reduction of the material budged. Reconstruction of secondary vertices will be newly possible also at forward rapidity due to the new Forward Muon Spectrometer placed in front of the muon absorber. These improvements will allow to study the non-prompt and prompt J/ψ production components with a better precision at midrapidity and newly also at forward rapidity. The measurement of the non-prompt J/ψ production enables studies of beauty quark physics. The measurements of higher charmonium states will be accessible. For example, the production of higher charmonium state ψ(2S) will be measured at midrapidity and forward rapidity. It is expected that the comparisons of the ratios of ψ(2S) and J/ψ production yields will lead to distinguishing between models including (re)generation at the phase boundary and during the QGP phase [186, 187].

The data-driven PID efficiency helps to reduce systematic uncertainty on the measurement presented in this thesis and will be important as well for the J/ψ analysis using Run 3 data samples. Increased abundance of collected data should be accompanied also by further improvements of the analysis methods. Statistical and systematic uncertainties are currently similar for p_{T}-differential measurement and the granularity of p_{T} intervals already reveals relatively well the shape of the J/ψ production yield distribution. Thus, in order to fully profit from great abundance of the data in the Run 3, it will be needed to reduce as well currently dominant source of systematic uncertainty—the uncertainty on the ITS-TPC matching efficiency. The difference between MC simulation and the data should be used to correct the data points itself instead of assigning systematic uncertainty. This will require careful studies of systematic uncertainties on such correction.

In conclusion, an exciting data taking of abundant Pb–Pb collision data samples lies ahead of the ALICE collaboration. New analysis methods help to improve precision of the J/ψ production already now. Further developments should follow. The underlying mechanisms of the charmonium (re)generation in Pb–Pb collisions at the LHC energy could be revealed soon.

Publications and other contributions

The measurement presented in this work is part of the first publication listed below. The physics analysis is internally reviewed in the ALICE Collaboration. The publication is currently in preparation. The preliminary results of the measurement have been presented as a posted at the Quark Matter Conference 2019. The second publication listed below are conference proceedings from the LHCP2020 conference. Besides of the two publications, a contribution has been made to the ALICE TPC upgrade. I have participated in testing of the Gas Electron Multiplier foils after their arrival at GSI Helmholtzzentrum für Schwerionenforschung in Darmstadt, their framing, the assembling onto the readout chamber bodies, and testing of the chambers.

1) ALICE collaboration, "Measurement of inclusive J/ψ production at mid- and forward rapidity in Pb–Pb collisions at $\sqrt{s_{\mathrm{NN}}} = 5.02$ TeV", publication in preparation.

2) Alena Gromada, "Recent results on hard and rare probes from ALICE", In: *PoS* LHCP2020 (2021). Ed. by Bruno Mansoulie, et al., p. 032. DOI: 10.22323/1.382.0032, arXiv:2010.04692 [nucl-ex].

Bibliography

[1] D. Boyanovsky, H. J. de Vega, and D. J. Schwarz. "Phase transitions in the early and the present universe". In: *Ann. Rev. Nucl. Part. Sci.* 56 (2006), pp. 441–500. DOI: `10.1146/annurev.nucl.56.080805.140539`. arXiv: `hep-ph/0602002`.

[2] C. Burgard and D. Galbraith. "A standard diagram of the current standard model of physics". 2021. URL: `https://texample.net/tikz/examples/model-physics/`.

[3] P. A. Zyla et al. "Particle listings". 2020. URL: `https://pdg.lbl.gov/2021/listings/contents_listings.html`.

[4] Y. Fukuda et al. "Evidence for oscillation of atmospheric neutrinos". In: *Phys. Rev. Lett.* 81 (1998), pp. 1562–1567. DOI: `10.1103/PhysRevLett.81.1562`. arXiv: `hep-ex/9807003`.

[5] Q. R. Ahmad et al. "Direct evidence for neutrino flavor transformation from neutral current interactions in the Sudbury Neutrino Observatory". In: *Phys. Rev. Lett.* 89 (2002), p. 011301. DOI: `10.1103/PhysRevLett.89.011301`. arXiv: `nucl-ex/0204008`.

[6] H. David Politzer. "Reliable Perturbative Results for Strong Interactions?" In: *Phys. Rev. Lett.* 30 (1973). Ed. by J. C. Taylor, pp. 1346–1349. DOI: `10.1103/PhysRevLett.30.1346`.

[7] D. J. Gross and F. Wilczek. "Ultraviolet Behavior of Nonabelian Gauge Theories". In: *Phys. Rev. Lett.* 30 (1973). Ed. by J. C. Taylor, pp. 1343–1346. DOI: `10.1103/PhysRevLett.30.1343`.

[8] D. J. Gross. "Twenty five years of asymptotic freedom". In: *Nucl. Phys. B Proc. Suppl.* 74 (1999). Ed. by Stephan Narison, pp. 426–446. DOI: `10.1016/S0920-5632(99)00208-X`. arXiv: `hep-th/9809060`.

[9] M. Tanabashi et al. "Review of Particle Physics". In: *Phys. Rev. D* 98 (3 2018), p. 030001. DOI: `10.1103/PhysRevD.98.030001`. URL: `https://link.aps.org/doi/10.1103/PhysRevD.98.030001`.

[10] Y. Aoki et al. "The order of the quantum chromodynamics transition predicted by the standard model of particle physics". In: *Nature* 443 (2006), pp. 675–678. DOI: `10.1038/nature05120`. arXiv: `hep-lat/0611014`.

[11] Y. Aoki et al. "The QCD transition temperature: Results with physical masses in the continuum limit". In: *Phys. Lett. B* 643 (2006), pp. 46–54. DOI: `10.1016/j.physletb.2006.10.021`. arXiv: `hep-lat/0609068`.

[12] J. N. Guenther. "Overview of the QCD phase diagram: Recent progress from the lattice". In: *Eur. Phys. J. A* 57.4 (2021), p. 136. DOI: `10.1140/epja/s10050-021-00354-6`. arXiv: `2010.15503 [hep-lat]`.

[13] T. K. Nayak. "Probing the QCD phase structure using event-by-event fluctuations". In: *J. Phys. Conf. Ser.* 1602.1 (2020). Ed. by Rene Bellwied et al., p. 012003. DOI: `10.1088/1742-6596/1602/1/012003`. arXiv: `2008.04643 [nucl-ex]`.

[14] P. de Forcrand, S. Kim, and O. Philipsen. "A QCD chiral critical point at small chemical potential: is it there or not?". 2008. arXiv: `0711.0262 [hep-lat]`.

[15] G. Baym et al. "From hadrons to quarks in neutron stars: a review". In: *Rept. Prog. Phys.* 81.5 (2018), p. 056902. DOI: `10.1088/1361-6633/aaae14`. arXiv: `1707.04966 [astro-ph.HE]`.

[16] W. Florkowski. "Phenomenology of ultra-relativistic heavy-ion collisions". Technical Design Report ALICE. Geneva: World Scientific, 2010.

[17] R. Stock. "Relativistic Nucleus-Nucleus Collisions and the QCD Matter Phase Diagram". In: (July 2008). DOI: 10.1007/978-3-540-74203-6_7. arXiv: 0807.1610 [nucl-ex].

[18] K. Aamodt et al. "Two-pion Bose-Einstein correlations in central Pb–Pb collisions at $\sqrt{s_{NN}} = 2.76$ TeV". In: *Phys. Lett. B* 696 (2011), pp. 328–337. DOI: 10.1016/j.physletb.2010.12.053. arXiv: 1012.4035 [nucl-ex].

[19] Raimond Snellings. "Collective Expansion at the LHC: selected ALICE anisotropic flow measurements". In: *J. Phys. G* 41.12 (2014), p. 124007. DOI: 10.1088/0954-3899/41/12/124007. arXiv: 1408.2532 [nucl-ex].

[20] ALICE Collaboration. "Centrality determination in heavy ion collisions". In: (2018). URL: https://cds.cern.ch/record/2636623.

[21] P. Braun-Munzinger and J. Stachel. "The quest for the quark-gluon plasma". In: *Nature* 448 (2007), pp. 302–309.

[22] A. Andronic, P. Braun-Munzinger, and J. Stachel. "Thermal hadron production in relativistic nuclear collisions: The Hadron mass spectrum, the horn, and the QCD phase transition". In: *Phys. Lett. B* 673 (2009). [Erratum: Phys.Lett.B 678, 516 (2009)], pp. 142–145. DOI: 10.1016/j.physletb.2009.06.021. arXiv: 0812.1186 [nucl-th].

[23] J. Stachel et al. "Confronting LHC data with the statistical hadronization model". In: *Journal of Physics: Conference Series* 509 (2014), p. 012019. DOI: 10.1088/1742-6596/509/1/012019. URL: https://doi.org/10.1088/1742-6596/509/1/012019.

[24] A. Andronic et al. "Decoding the phase structure of QCD via particle production at high energy". In: *Nature* 561.7723 (2018), pp. 321–330. DOI: 10.1038/s41586-018-0491-6. arXiv: 1710.09425 [nucl-th].

[25] R. Snellings. "Elliptic Flow: A Brief Review". In: *New J. Phys.* 13 (2011), p. 055008. DOI: 10.1088/1367-2630/13/5/055008. arXiv: 1102.3010 [nucl-ex].

[26] R. S. Bhalerao and J.-Y. Ollitrault. "Eccentricity fluctuations and elliptic flow at RHIC". In: *Phys. Lett. B* 641 (2006), pp. 260–264. DOI: 10.1016/j.physletb.2006.08.055. arXiv: nucl-th/0607009.

[27] S. Acharya et al. "Anisotropic flow of identified particles in Pb–Pb collisions at $\sqrt{s_{NN}} = 5.02$ TeV". In: *JHEP* 09 (2018), p. 006. DOI: 10.1007/JHEP09(2018)006. arXiv: 1805.04390 [nucl-ex].

[28] R. Baier et al. "Induced gluon radiation in a QCD medium". In: *Phys. Lett. B* 345 (1995), pp. 277–286. DOI: 10.1016/0370-2693(94)01617-L. arXiv: hep-ph/9411409.

[29] M. Gyulassy and M. Plümer. "Jet quenching in dense matter". In: *Physics Letters B* 243.4 (1990), pp. 432–438. ISSN: 0370-2693. DOI: https://doi.org/10.1016/0370-2693(90)91409-5. URL: https://www.sciencedirect.com/science/article/pii/0370269390914095.

[30] H. Song and U. W. Heinz. "Suppression of elliptic flow in a minimally viscous quark-gluon plasma". In: *Phys. Lett. B* 658 (2008), pp. 279–283. DOI: 10.1016/j.physletb.2007.11.019. arXiv: 0709.0742 [nucl-th].

[31] M. Djordjevic. "Heavy flavor puzzle at LHC: a serendipitous interplay of jet suppression and fragmentation". In: *Phys. Rev. Lett.* 112.4 (2014), p. 042302. DOI: 10.1103/PhysRevLett.112.042302. arXiv: 1307.4702 [nucl-th].

[32] B. Abelev et al. "Centrality Dependence of Charged Particle Production at Large Transverse Momentum in Pb–Pb Collisions at $\sqrt{s_{NN}} = 2.76$ TeV". In: *Phys. Lett. B* 720 (2013), pp. 52–62. DOI: 10.1016/j.physletb.2013.01.051. arXiv: 1208.2711 [hep-ex].

[33] S. Chatrchyan et al. "Study of high-p_T charged particle suppression in Pb–Pb compared to pp collisions at $\sqrt{s_{NN}} = 2.76$ TeV". In: *Eur. Phys. J. C* 72 (2012), p. 1945. DOI: 10.1140/epjc/s10052-012-1945-x. arXiv: 1202.2554 [nucl-ex].

[34] B. Abelev et al. "Transverse momentum dependence of inclusive primary charged-particle production in p–Pb collisions at $\sqrt{s_{\mathrm{NN}}} = 5.02$ TeV". In: *Eur. Phys. J. C* 74.9 (2014), p. 3054. DOI: 10.1140/epjc/s10052-014-3054-5. arXiv: 1405.2737 [nucl-ex].

[35] S. Chatrchyan et al. "Measurement of isolated photon production in pp and Pb–Pb collisions at $\sqrt{s_{\mathrm{NN}}} = 2.76$ TeV". In: *Phys. Lett. B* 710 (2012), pp. 256–277. DOI: 10.1016/j.physletb.2012.02.077. arXiv: 1201.3093 [nucl-ex].

[36] S. Chatrchyan et al. "Study of W boson production in Pb–Pb and pp collisions at $\sqrt{s_{\mathrm{NN}}} = 2.76$ TeV". In: *Phys. Lett. B* 715 (2012), pp. 66–87. DOI: 10.1016/j.physletb.2012.07.025. arXiv: 1205.6334 [nucl-ex].

[37] S. Chatrchyan et al. "Study of Z boson production in Pb–Pb collisions at $\sqrt{s_{\mathrm{NN}}} = 2.76$ TeV". In: *Phys. Rev. Lett.* 106 (2011), p. 212301. DOI: 10.1103/PhysRevLett.106.212301. arXiv: 1102.5435 [nucl-ex].

[38] S. Acharya et al. "Transverse momentum spectra and nuclear modification factors of charged particles in pp, p–Pb and Pb–Pb collisions at the LHC". In: *JHEP* 11 (2018), p. 013. DOI: 10.1007/JHEP11(2018)013. arXiv: 1802.09145 [nucl-ex].

[39] S. Acharya et al. "Measurement of D^0, D^+, D^{*+} and D_s^+ production in Pb–Pb collisions at $\sqrt{s_{\mathrm{NN}}} = 5.02$ TeV". In: *JHEP* 10 (2018), p. 174. DOI: 10.1007/JHEP10(2018)174. arXiv: 1804.09083 [nucl-ex].

[40] S. Acharya et al. "Direct observation of the dead-cone effect in QCD". In: (June 2021). arXiv: 2106.05713 [nucl-ex].

[41] A. Beraudo et al. "Extraction of Heavy-Flavor Transport Coefficients in QCD Matter". In: *Nucl. Phys. A* 979 (2018). Ed. by R. Rapp et al., pp. 21–86. DOI: 10.1016/j.nuclphysa.2018.09.002. arXiv: 1803.03824 [nucl-th].

[42] J. J. Aubert et al. "Experimental Observation of a Heavy Particle J". In: *Phys. Rev. Lett.* 33 (23 1974), pp. 1404–1406. DOI: 10.1103/PhysRevLett.33.1404. URL: https://link.aps.org/doi/10.1103/PhysRevLett.33.1404.

[43] J. E. Augustin et al. "Discovery of a Narrow Resonance in e^+e^- Annihilation". In: *Phys. Rev. Lett.* 33 (23 1974), pp. 1406–1408. DOI: 10.1103/PhysRevLett.33.1406. URL: https://link.aps.org/doi/10.1103/PhysRevLett.33.1406.

[44] T. Appelquist and H. D. Politzer. "Heavy Quarks and e^+e^- Annihilation". In: *Phys. Rev. Lett.* 34 (1 1975), pp. 43–45. DOI: 10.1103/PhysRevLett.34.43. URL: https://link.aps.org/doi/10.1103/PhysRevLett.34.43.

[45] A. De Rújula and S. L. Glashow. "Is Bound Charm Found?" In: *Phys. Rev. Lett.* 34 (1 1975), pp. 46–49. DOI: 10.1103/PhysRevLett.34.46. URL: https://link.aps.org/doi/10.1103/PhysRevLett.34.46.

[46] S. Chatrchyan et al. "Performance of CMS Muon Reconstruction in pp Collision Events at $\sqrt{s} = 7$ TeV". In: *JINST* 7 (2012), P10002. DOI: 10.1088/1748-0221/7/10/P10002. arXiv: 1206.4071 [physics.ins-det].

[47] S. Okubo. "ϕ-meson and unitary symmetry model". In: *Physics Letters* 5.2 (1963), pp. 165–168. ISSN: 0031-9163. DOI: https://doi.org/10.1016/S0375-9601(63)92548-9. URL: https://www.sciencedirect.com/science/article/pii/S0375960163925489.

[48] G. Zweig. "An SU_3 model for strong interaction symmetry and its breaking; Version 2". In: (1964), 80 p. URL: https://cds.cern.ch/record/570209.

[49] J. Iizuka. "A Systematics and Phenomenology of Meson Family". In: *Progress of Theoretical Physics Supplement* 37-38 (Mar. 1966), pp. 21–34. ISSN: 0375-9687. DOI: 10.1143/PTPS.37.21. eprint: https://academic.oup.com/ptps/article-pdf/doi/10.1143/PTPS.37.21/5215468/37-38-21.pdf. URL: https://doi.org/10.1143/PTPS.37.21.

[50] H. Satz. "Colour deconfinement and quarkonium binding". In: *Journal of Physics G: Nuclear and Particle Physics* 32.3 (2006), R25–R69. ISSN: 1361-6471. DOI: 10.1088/0954-3899/32/3/r01. URL: http://dx.doi.org/10.1088/0954-3899/32/3/R01.

[51] E. Eichten et al. "Spectrum of Charmed Quark-Antiquark Bound States". In: *Phys. Rev. Lett.* 34 (6 1975), pp. 369–372. DOI: 10.1103/PhysRevLett.34.369. URL: https://link.aps.org/doi/10.1103/PhysRevLett.34.369.

[52] C. Ayala, P. González, and V. Vento. "Heavy quark potential from QCD-related effective coupling". In: *Journal of Physics G: Nuclear and Particle Physics* 43.12 (2016), p. 125002. ISSN: 1361-6471. DOI: 10.1088/0954-3899/43/12/125002. URL: http://dx.doi.org/10.1088/0954-3899/43/12/125002.

[53] R. Aaij et al. "Measurement of the ratio of prompt χ_c to J/ψ production in pp collisions at $\sqrt{s} = 7$ TeV". In: *Phys. Lett. B* 718 (2012), pp. 431–440. DOI: 10.1016/j.physletb.2012.10.068. arXiv: 1204.1462 [hep-ex].

[54] F. Abe et al. "Production of J/ψ Mesons from χ_c Meson Decays in $p\overline{p}$ Collisions at $\sqrt{s} = 1.8$ TeV". In: *Phys. Rev. Lett.* 79 (4 1997), pp. 578–583. DOI: 10.1103/PhysRevLett.79.578. URL: https://link.aps.org/doi/10.1103/PhysRevLett.79.578.

[55] S. Acharya et al. "Energy dependence of forward-rapidity J/ψ and ψ(2S) production in pp collisions at the LHC". In: *Eur. Phys. J. C* 77.6 (2017), p. 392. DOI: 10.1140/epjc/s10052-017-4940-4. arXiv: 1702.00557 [hep-ex].

[56] S. Acharya et al. "Inclusive, prompt and non-prompt J/ψ production at midrapidity in p–Pb collisions at $\sqrt{s_{\mathrm{NN}}} = 5.02$ TeV". In: (May 2021). arXiv: 2105.04957 [nucl-ex].

[57] J. Adam et al. "Inclusive, prompt and non-prompt J/ψ production at mid-rapidity in Pb–Pb collisions at $\sqrt{s_{\mathrm{NN}}} = 2.76$ TeV". In: *Journal of High Energy Physics* 2015.7 (2015). ISSN: 1029-8479. DOI: 10.1007/jhep07(2015)051. URL: http://dx.doi.org/10.1007/JHEP07(2015)051.

[58] A. Andronic et al. "Heavy-flavour and quarkonium production in the LHC era: from proton-proton to heavy-ion collisions". In: *The European Physical Journal C* 76.3 (2016). ISSN: 1434-6052. DOI: 10.1140/epjc/s10052-015-3819-5. URL: http://dx.doi.org/10.1140/epjc/s10052-015-3819-5.

[59] H1 Collaboration. "Inclusive Deep Inelastic Scattering at High Q2 with Longitudinally Polarised Lepton Beams at HERA". 2012. arXiv: 1206.7007 [hep-ex].

[60] K. A. Olive et al. "Review of Particle Physics". In: *Chin. Phys. C* 38 (2014), p. 090001. DOI: 10.1088/1674-1137/38/9/090001.

[61] H. Fritzsch. "Producing heavy quark flavors in hadronic collisions - A test of quantum chromodynamics". In: *Physics Letters B* 67.2 (1977), pp. 217–221. ISSN: 0370-2693. DOI: https://doi.org/10.1016/0370-2693(77)90108-3. URL: https://www.sciencedirect.com/science/article/pii/0370269377901083.

[62] F. Halzen. "CVC for gluons and hadroproduction of quark flavours". In: *Physics Letters B* 69.1 (1977), pp. 105–108. ISSN: 0370-2693. DOI: https://doi.org/10.1016/0370-2693(77)90144-7. URL: https://www.sciencedirect.com/science/article/pii/0370269377901447.

[63] Y.-Q. Ma and R. Vogt. "Quarkonium production in an improved color evaporation model". In: *Phys. Rev. D* 94 (11 2016), p. 114029. DOI: 10.1103/PhysRevD.94.114029. URL: https://link.aps.org/doi/10.1103/PhysRevD.94.114029.

[64] Chang C.-H. "Hadronic production of J/ψ associated with a gluon". In: *Nuclear Physics B* 172 (1980), pp. 425–434. ISSN: 0550-3213. DOI: https://doi.org/10.1016/0550-3213(80)90175-3. URL: https://www.sciencedirect.com/science/article/pii/0550321380901753.

[65] E. Braaten G. T. Bodwin and G. P. Lepage. "Rigorous QCD analysis of inclusive annihilation and production of heavy quarkonium". In: *Physics Letters B* (1995), pp. 1125–1171. DOI: https://doi.org/10.1103/PhysRevD.51.112510.1103/PhysRevD.55.5853.

[66] S. Acharya et al. "Inclusive J/ψ production at mid-rapidity in pp collisions at $\sqrt{s} = 5.02$ TeV". In: *JHEP* 10 (2019), p. 084. DOI: 10.1007/JHEP10(2019)084. arXiv: 1905.07211 [nucl-ex].

[67] M. Aaboud et al. "Measurement of quarkonium production in proton-lead and proton-proton collisions at 5.02 TeV with the ATLAS detector". In: *The European Physical Journal C* 78.3 (2018). ISSN: 1434-6052. DOI: 10.1140/epjc/s10052-018-5624-4. URL: http://dx.doi.org/10.1140/epjc/s10052-018-5624-4.

[68] A. M. Sirunyan et al. "Measurement of prompt and nonprompt J/ψ production in pp and pPb collisions at $\sqrt{s_{\mathrm{NN}}} = 5.02$TeV". In: *The European Physical Journal C* 77.4 (2017). ISSN: 1434-6052. DOI: 10.1140/epjc/s10052-017-4828-3. URL: http://dx.doi.org/10.1140/epjc/s10052-017-4828-3.

[69] Y.-Q. Ma, K. Wang, and K.-T. Chao. "J/$\psi(\psi')$ production at the Tevatron and LHC at O($\alpha_s^4 v^4$) in nonrelativistic QCD". In: *Physical Review Letters* 106.4 (2011). ISSN: 1079-7114. DOI: 10.1103/physrevlett.106.042002. URL: http://dx.doi.org/10.1103/PhysRevLett.106.042002.

[70] M. Butenschön and B. A. Kniehl. "Reconciling J/ψ production at HERA, RHIC, Tevatron, and LHC with nonrelativistic QCD factorization at Next-to-Leading Order". In: *Physical Review Letters* 106.2 (2011). ISSN: 1079-7114. DOI: 10.1103/physrevlett.106.022003. URL: http://dx.doi.org/10.1103/PhysRevLett.106.022003.

[71] Y.-Q. Ma and R. Venugopalan. "Comprehensive description of J/ψ production in proton-proton collisions at collider energies". In: *Physical Review Letters* 113.19 (2014). ISSN: 1079-7114. DOI: 10.1103/physrevlett.113.192301. URL: http://dx.doi.org/10.1103/PhysRevLett.113.192301.

[72] M. Cacciari et al. "Theoretical predictions for charm and bottom production at the LHC". In: *Journal of High Energy Physics* 2012.10 (2012). ISSN: 1029-8479. DOI: 10.1007/jhep10(2012)137. URL: http://dx.doi.org/10.1007/JHEP10(2012)137.

[73] Y.-Q. Ma and R. Venugopalan. "Comprehensive Description of J/ψ Production in Proton-Proton Collisions at Collider Energies". In: *Phys. Rev. Lett.* 113 (19 2014), p. 192301. DOI: 10.1103/PhysRevLett.113.192301. URL: https://link.aps.org/doi/10.1103/PhysRevLett.113.192301.

[74] S. Acharya et al. "Energy dependence of forward-rapidity J/ψ and $\psi(2S)$ production in pp collisions at the LHC". In: *The European Physical Journal C* 77.6 (2017). ISSN: 1434-6052. DOI: 10.1140/epjc/s10052-017-4940-4. URL: http://dx.doi.org/10.1140/epjc/s10052-017-4940-4.

[75] S. Acharya et al. "Measurement of the inclusive J/ψ polarization at forward rapidity in pp collisions at $\sqrt{s} = 8$ TeV". In: *The European Physical Journal C* 78.7 (2018). ISSN: 1434-6052. DOI: 10.1140/epjc/s10052-018-6027-2. URL: http://dx.doi.org/10.1140/epjc/s10052-018-6027-2.

[76] B. Abelev et al. "Inclusive J/ψ production in pp collisions at $\sqrt{s} = 2.76$ TeV". In: *Phys. Lett. B* 718 (2012). [Erratum: Phys.Lett.B 748, 472–473 (2015)], pp. 295–306. DOI: 10.1016/j.physletb.2012.10.078. arXiv: 1203.3641 [hep-ex].

[77] K. Aamodt et al. "Rapidity and transverse momentum dependence of inclusive J/ψ production in pp collisions at $\sqrt{s} = 7$ TeV". In: *Phys. Lett. B* 704 (2011). [Erratum: Phys.Lett.B 718, 692–698 (2012)], pp. 442–455. DOI: 10.1016/j.physletb.2011.09.054. arXiv: 1105.0380 [hep-ex].

[78] D. Acosta et al. "Measurement of the J/ψ meson and $b-$hadron production cross sections in p$\bar{\mathrm{p}}$ collisions at $\sqrt{s} = 1960$ GeV". In: *Phys. Rev. D* 71 (2005), p. 032001. DOI: 10.1103/PhysRevD.71.032001. arXiv: hep-ex/0412071.

[79] A. Adare et al. "Ground and excited charmonium state production in $p + p$ collisions at $\sqrt{s} = 200$ GeV". In: *Phys. Rev. D* 85 (2012), p. 092004. DOI: 10.1103/PhysRevD.85.092004. arXiv: 1105.1966 [hep-ex].

[80] J. Adam et al. "J/ψ production cross section and its dependence on charged-particle multiplicity in $p + p$ collisions at $\sqrt{s} = 200$ GeV". In: *Phys. Lett. B* 786 (2018), pp. 87–93. DOI: 10.1016/j.physletb.2018.09.029. arXiv: 1805.03745 [hep-ex].

[81] K. J. Eskola et al. "EPPS16: nuclear parton distributions with LHC data". In: *The European Physical Journal C* 77.3 (2017). ISSN: 1434-6052. DOI: 10.1140/epjc/s10052-017-4725-9. URL: http://dx.doi.org/10.1140/epjc/s10052-017-4725-9.

[82] L. McLerran. "The Color Glass Condensate and Small x Physics: 4 Lectures". In: (2001). arXiv: 0104285 [hep-ph].

[83] CLAS Collaboration. "Modified structure of protons and neutrons in correlated pairs". In: *Nature* 566.7744 (2019), pp. 354–358. ISSN: 1476-4687. DOI: 10.1038/s41586-019-0925-9. URL: http://dx.doi.org/10.1038/s41586-019-0925-9.

[84] F. Arleo et al. "Centrality and $p_{\rm T}$ dependence of J/ψ suppression in proton-nucleus collisions from parton energy loss". In: *JHEP* 05 (2013), p. 155. DOI: 10.1007/JHEP05(2013)155. arXiv: 1304.0901 [hep-ph].

[85] C. Lourenco, R. Vogt, and H. K. Woehri. "Energy dependence of J/ψ absorption in proton-nucleus collisions". In: *JHEP* 02 (2009), p. 014. DOI: 10.1088/1126-6708/2009/02/014. arXiv: 0901.3054 [hep-ph].

[86] M. Aaboud et al. "Measurement of quarkonium production in proton–lead and proton–proton collisions at 5.02 TeV with the ATLAS detector". In: *The European Physical Journal C* 78.3 (2018). ISSN: 1434-6052. DOI: 10.1140/epjc/s10052-018-5624-4. URL: http://dx.doi.org/10.1140/epjc/s10052-018-5624-4.

[87] J.-P. Lansberg and H.-S. Shao. "Towards an automated tool to evaluate the impact of the nuclear modification of the gluon density on quarkonium, D and B meson production in proton-nucleus collisions". In: *The European Physical Journal C* 77.1 (2016). ISSN: 1434-6052. DOI: 10.1140/epjc/s10052-016-4575-x. URL: http://dx.doi.org/10.1140/epjc/s10052-016-4575-x.

[88] K. Kovařík et al. "nCTEQ15: Global analysis of nuclear parton distributions with uncertainties in the CTEQ framework". In: *Physical Review D* 93.8 (2016). ISSN: 2470-0029. DOI: 10.1103/physrevd.93.085037. URL: http://dx.doi.org/10.1103/PhysRevD.93.085037.

[89] S. Acharya et al. "Coherent J/ψ and ψ′ photoproduction at midrapidity in ultra-peripheral Pb–Pb collisions at $\sqrt{s_{\rm NN}} = 5.02$ TeV". In: (Jan. 2021). arXiv: 2101.04577 [nucl-ex].

[90] J. Nystrand. "Photonuclear vector meson production in ultra-peripheral Pb–Pb collisions studied by the ALICE experiment at the LHC". In: *PoS* ConfinementX (2012). Ed. by Matthias Berwein, Nora Brambilla, and Stephan Paul, p. 199. DOI: 10.22323/1.171.0199. arXiv: 1303.2009 [nucl-ex].

[91] S. Klein and J. Nystrand. "Exclusive vector meson production in relativistic heavy ion collisions". In: *Phys. Rev. C* 60 (1999), p. 014903. DOI: 10.1103/PhysRevC.60.014903. arXiv: hep-ph/9902259.

[92] S. Acharya et al. "Coherent J/ψ photoproduction at forward rapidity in ultra-peripheral Pb–Pb collisions at $\sqrt{s_{\rm NN}} = 5.02$ TeV". In: *Phys. Lett. B* 798 (2019), p. 134926. DOI: 10.1016/j.physletb.2019.134926. arXiv: 1904.06272 [nucl-ex].

[93] T. Matsui and H. Satz. "J/ψ suppression by quark-gluon plasma formation". In: *Physics Letters B* 178.4 (1986), pp. 416–422. ISSN: 0370-2693. DOI: https://doi.org/10.1016/0370-2693(86)91404-8. URL: https://www.sciencedirect.com/science/article/pii/0370269386914048.

[94] A. Mocsy. "Potential Models for Quarkonia". In: *Eur. Phys. J. C* 61 (2009). Ed. by N. Armesto et al., pp. 705–710. DOI: 10.1140/epjc/s10052-008-0847-4. arXiv: 0811.0337 [hep-ph].

[95] G. Borges et al. "Charmonia production at the CERN/SPS". In: *J. Phys. G* 32 (2006), S381–S390. DOI: 10.1088/0954-3899/32/12/S47. arXiv: hep-ex/0505065.

[96]   A. Adare et al. "J/ψ suppression at forward rapidity in Au+Au collisions at $\sqrt{s_{\mathrm{NN}}} = 200$ GeV". In: *Physical Review C* 84.5 (2011). ISSN: 1089-490X. DOI: 10.1103/physrevc.84.054912. URL: http://dx.doi.org/10.1103/PhysRevC.84.054912.

[97]   A. Adare et al. "J/ψ Production vs Centrality, Transverse Momentum, and Rapidity in Au+Au Collisions at $\sqrt{s_{\mathrm{NN}}} = 200$ GeV". In: *Phys. Rev. Lett.* 98 (2007), p. 232301. DOI: 10.1103/PhysRevLett.98.232301. arXiv: nucl-ex/0611020.

[98]   L. Kluberg and H. Satz. "Color Deconfinement and Charmonium Production in Nuclear Collisions". In: *Landolt-Börnstein - Group I Elementary Particles, Nuclei and Atoms* (2010), pp. 373–423. ISSN: 1616-9522. DOI: 10.1007/978-3-642-01539-7_13. URL: http://dx.doi.org/10.1007/978-3-642-01539-7_13.

[99]   A. Andronic et al. "Statistical hadronization of heavy quarks in ultra-relativistic nucleus-nucleus collisions". In: *Nuclear Physics A* 789.1 (2007), pp. 334–356. ISSN: 0375-9474. DOI: https://doi.org/10.1016/j.nuclphysa.2007.02.013. URL: https://www.sciencedirect.com/science/article/pii/S0375947407002126.

[100] A. Andronic et al. "The thermal model on the verge of the ultimate test: particle production in Pb–Pb collisions at the LHC". In: *Journal of Physics G: Nuclear and Particle Physics* 38.12 (2011), p. 124081. ISSN: 1361-6471. DOI: 10.1088/0954-3899/38/12/124081. URL: http://dx.doi.org/10.1088/0954-3899/38/12/124081.

[101] A. Andronic et al. "Transverse momentum distributions of charmonium states with the statistical hadronization model". In: *Phys. Lett. B* 797 (2019), p. 134836. DOI: 10.1016/j.physletb.2019.134836. arXiv: 1901.09200 [nucl-th].

[102] R. Rapp and X. Du. "Theoretical Perspective on Quarkonia from SPS via RHIC to LHC". In: *Nucl. Phys. A* 967 (2017). Ed. by Ulrich Heinz, Olga Evdokimov, and Peter Jacobs, pp. 216–224. DOI: 10.1016/j.nuclphysa.2017.05.097. arXiv: 1704.07923 [hep-ph].

[103] X. Zhao and R. Rapp. "Transverse Momentum Spectra of J/ψ in Heavy-Ion Collisions". In: *Phys. Lett. B* 664 (2008), pp. 253–257. DOI: 10.1016/j.physletb.2008.03.068. arXiv: 0712.2407 [hep-ph].

[104] X. Zhao and R. Rapp. "Medium Modifications and Production of Charmonia at LHC". In: *Nucl. Phys. A* 859 (2011), pp. 114–125. DOI: 10.1016/j.nuclphysa.2011.05.001. arXiv: 1102.2194 [hep-ph].

[105] X. Du and R. Rapp. "Sequential Regeneration of Charmonia in Heavy-Ion Collisions". In: *Nucl. Phys.* A943 (2015), pp. 147–158. DOI: 10.1016/j.nuclphysa.2015.09.006. arXiv: 1504.00670 [hep-ph].

[106] K. Zhou et al. "Medium effects on charmonium production at ultrarelativistic energies available at the CERN Large Hadron Collider". In: *Phys. Rev. C* 89.5 (2014), p. 054911. DOI: 10.1103/PhysRevC.89.054911. arXiv: 1401.5845 [nucl-th].

[107] Z. Tang et al. "Charmonium Transverse Momentum Distribution in High Energy Nuclear Collisions". In: *J. Phys. G* 41.12 (2014), p. 124006. DOI: 10.1088/0954-3899/41/12/124006. arXiv: 1409.5559 [nucl-th].

[108] E. G. Ferreiro. "Charmonium dissociation and recombination at LHC: Revisiting comovers". In: *Phys. Lett. B* 731 (2014), pp. 57–63. DOI: 10.1016/j.physletb.2014.02.011. arXiv: 1210.3209 [hep-ph].

[109] B. Abelev et al. "J/ψ suppression at forward rapidity in Pb–Pb collisions at $\sqrt{s_{\mathrm{NN}}} = 2.76$ TeV". In: *Phys. Rev. Lett.* 109 (2012), p. 072301. DOI: 10.1103/PhysRevLett.109.072301. arXiv: 1202.1383 [hep-ex].

[110] J. Adam et al. "Inclusive, prompt and non-prompt J/ψ production at mid-rapidity in Pb–Pb collisions at $\sqrt{s_{\mathrm{NN}}} = 2.76$ TeV". In: *JHEP* 07 (2015), p. 051. DOI: 10.1007/JHEP07(2015)051. arXiv: 1504.07151 [nucl-ex].

[111] A. Adare et al. "J/ψ Production vs Centrality, Transverse Momentum, and Rapidity in Au+Au Collisions at $\sqrt{s_{NN}}$ = 200 GeV". In: *Phys. Rev. Lett.* 98 (2007), p. 232301. DOI: 10.1103/PhysRevLett.98.232301. arXiv: nucl-ex/0611020.

[112] S. Chatrchyan et al. "Suppression of non-prompt J/ψ, prompt J/ψ, and Υ(1S) in Pb–Pb collisions at $\sqrt{s_{NN}}$ = 2.76 TeV". In: *JHEP* 05 (2012), p. 063. DOI: 10.1007/JHEP05(2012)063. arXiv: 1201.5069 [nucl-ex].

[113] X. Zhao and R. Rapp. "Charmonium in Medium: From Correlators to Experiment". In: *Phys. Rev. C* 82 (2010), p. 064905. DOI: 10.1103/PhysRevC.82.064905. arXiv: 1008.5328 [hep-ph].

[114] S. Acharya et al. "J/ψ elliptic and triangular flow in Pb–Pb collisions at $\sqrt{s_{NN}}$ = 5.02 TeV". In: *JHEP* 10 (2020), p. 141. DOI: 10.1007/JHEP10(2020)141. arXiv: 2005.14518 [nucl-ex].

[115] Science and Technology Facilities Council. "CERN Accelerator Complex". 2020. URL: https://stfc.ukri.org/research/particle-physics-and-particle-astrophysics/large-hadron-collider/cern-accelerator-complex/.

[116] G. Aad et al. "The ATLAS Experiment at the CERN Large Hadron Collider". In: *Journal of Instrumentation* 3.08 (2008), S08003–S08003. DOI: 10.1088/1748-0221/3/08/s08003. URL: https://doi.org/10.1088/1748-0221/3/08/s08003.

[117] S. Chatrchyan et al. "The CMS experiment at the CERN LHC". In: *Journal of Instrumentation* 3.08 (2008), S08004–S08004. DOI: 10.1088/1748-0221/3/08/s08004. URL: https://doi.org/10.1088/1748-0221/3/08/s08004.

[118] S. Amato et al. "LHCb technical proposal: A Large Hadron Collider Beauty Experiment for Precision Measurements of CP Violation and Rare Decays". In: (Feb. 1998).

[119] S. Amato et al. "LHCb technical design report: Reoptimized detector design and performance". In: (Sept. 2003).

[120] K. Aamodt et al. "The ALICE experiment at the CERN LHC". In: *JINST* 3 (2008), S08002. DOI: 10.1088/1748-0221/3/08/S08002.

[121] L. Evans and P. Bryant. "LHC Machine". In: *JINST* 3 (2008), S08001. DOI: 10.1088/1748-0221/3/08/S08001.

[122] G. Aad et al. "Observation of a new particle in the search for the Standard Model Higgs boson with the ATLAS detector at the LHC". In: *Physics Letters B* 716.1 (2012), pp. 1–29. ISSN: 0370-2693. DOI: 10.1016/j.physletb.2012.08.020. URL: http://dx.doi.org/10.1016/j.physletb.2012.08.020.

[123] S. Chatrchyan et al. "Observation of a new boson at a mass of 125 GeV with the CMS experiment at the LHC". In: *Physics Letters B* 716.1 (2012), pp. 30–61. ISSN: 0370-2693. DOI: 10.1016/j.physletb.2012.08.021. URL: http://dx.doi.org/10.1016/j.physletb.2012.08.021.

[124] R. Aaij et al. "Observation of J/ψp Resonances Consistent with Pentaquark States in $\Lambda_b^0 \rightarrow$ J/ψK⁻p Decays". In: *Physical Review Letters* 115.7 (2015). ISSN: 1079-7114. DOI: 10.1103/physrevlett.115.072001. URL: http://dx.doi.org/10.1103/PhysRevLett.115.072001.

[125] ALICE collaboration. "Definition of the ALICE Coordinate System and Basic Rules for Sub-detector Components Numbering". 2003. URL: http://personalpages.to.infn.it/~tosello/EngMeet/NamingConventions/ALICE-INT-2003-038.pdf.

[126] Jens Weichula. "Commissioning and Calibration of ALICE-TPC, PhD. thesis". 2008. URL: https://cds.cern.ch/record/1295506?ln=en.

[127] ALICE collaboration. "The ALICE Detector". 2017. URL: https://alice-figure.web.cern.ch/node/11218.

[128] G. Dellacasa et al. "ALICE technical design report of the Inner Tracking System (ITS)". In: (June 1999).

[129] The ALICE Collaboration. "The ALICE TPC, a large 3-dimensional tracking device with fast readout for ultra-high multiplicity events". In: *Nuclear Instruments and Methods in Physics Research Section A: Accelerators, Spectrometers, Detectors and Associated Equipment* 622.1 (2010), pp. 316 –367. ISSN: 0168-9002. DOI: `https://doi.org/10.1016/j.nima.2010.04.042`. URL: `http://www.sciencedirect.com/science/article/pii/S0168900210008910`.

[130] ALICE Collaboration. "The ALICE Time Projection Chamber (TPC)". 2008. URL: `http://aliceinfo.cern.ch/Public/en/Chapter2/Chap2_TPC.html`.

[131] P. Cortese. "ALICE transition-radiation detector: Technical Design Report". Technical Design Report ALICE. Geneva: CERN, 2001. URL: `https://cds.cern.ch/record/519145`.

[132] ALICE Collaboration. "ALICE Time-Of-Flight system (TOF): Technical Design Report". Technical Design Report ALICE. Geneva: CERN, 2000. URL: `https://cds.cern.ch/record/430132`.

[133] M. Bondila et al. "ALICE T0 detector". In: *Nuclear Science, IEEE Transactions on* 52 (Nov. 2005), pp. 1705 –1711. DOI: `10.1109/TNS.2005.856900`.

[134] ALICE Collaboration. "Performance of the ALICE experiment at the CERN LHC". In: *International Journal of Modern Physics A* 29.24 (2014), p. 1430044. ISSN: 1793-656X. DOI: `10.1142/s0217751x14300440`. URL: `http://dx.doi.org/10.1142/S0217751X14300440`.

[135] N. Jacazio. "PID performance of the ALICE-TOF detector in Run 2". 2018. arXiv: `1809.00574 [physics.ins-det]`.

[136] R. E. Kalman. "A New Approach to Linear Filtering and Prediction Problems". In: *Transactions of the ASME–Journal of Basic Engineering* 82.Series D (1960), pp. 35–45.

[137] A. Kalweit. "Production of light flavor hadrons and anti-nuclei at the LHC, PhD. thesis". 2012. URL: `https://cds.cern.ch/record/2119440`.

[138] O. Schmidt. "Space Point Calibration of the ALICE TPC with Track Residuals, PhD. thesis". 2020. URL: `https://http://cds.cern.ch/record/2724259`.

[139] E. Hellbär. "The ALICE TPC: Optimization of the Performance in Run 2 and Developments for the Future". 2019. arXiv: `1909.03746 [physics.ins-det]`.

[140] ALICE Collaboration. "TPC space-charge distortions studies in RUN 2". 2018. URL: `https://alice-figure.web.cern.ch/node/15000`.

[141] C. Patrignani et al. "Review of Particle Physics". In: *Chin. Phys. C* 40.10 (2016), p. 100001. DOI: `10.1088/1674-1137/40/10/100001`.

[142] M. Arslandok. "Space Point Calibration of the ALICE TPC with Track Residuals, PhD. thesis". 2017. URL: `https://cds.cern.ch/record/2308311`.

[143] B. Hess. "Space Point Calibration of the ALICE TPC with Track Residuals, PhD. thesis". 2017. URL: `https://cds.cern.ch/record/2058633`.

[144] B. Abelev et al. "Centrality determination of Pb–Pb collisions at $\sqrt{s_{NN}} = 2.76$ TeV with ALICE". In: *Phys. Rev.* C88.4 (2013), p. 044909. DOI: `10.1103/PhysRevC.88.044909`. arXiv: `1301.4361 [nucl-ex]`.

[145] M. L. Miller et al. "Glauber modeling in high energy nuclear collisions". In: *Ann. Rev. Nucl. Part. Sci.* 57 (2007), pp. 205–243. DOI: `10.1146/annurev.nucl.57.090506.123020`. arXiv: `nucl-ex/0701025`.

[146] H. De Vries, C. W. De Jager, and C. De Vries. "Nuclear charge and magnetization density distribution parameters from elastic electron scattering". In: *Atom. Data Nucl. Data Tabl.* 36 (1987), pp. 495–536. DOI: `10.1016/0092-640X(87)90013-1`.

[147] C. Loizides, J. Kamin, and D. d'Enterria. "Improved Monte Carlo Glauber predictions at present and future nuclear colliders". In: *Phys. Rev.* C97.5 (2018), p. 054910. DOI: `10.1103/PhysRevC.97.054910,10.1103/PhysRevC.99.019901`. arXiv: `1710.07098 [nucl-ex]`.

[148] K. Aamodt et al. "Charged-particle multiplicity measurement in proton-proton collisions at $\sqrt{s} = 0.9$ and 2.36 TeV with ALICE at LHC". In: *European Physical Journal C* 68 (Apr. 2010), pp. 89–108. DOI: `10.1140/epjc/s10052-010-1339-x`.

[149] B. Abelev et al. "Technical Design Report for the Upgrade of the ALICE Inner Tracking System". In: *J. Phys. G* 41 (2014), p. 087002. DOI: `10.1088/0954-3899/41/8/087002`.

[150] ALICE Collaboration. "Upgrade of the ALICE Time Projection Chamber". Tech. rep. CERN-LHCC-2013-020. ALICE-TDR-016. 2013. URL: `https://cds.cern.ch/record/1622286`.

[151] F. V. Böhmer et al. "Space-Charge Effects in an Ungated GEM-based TPC". 2012. arXiv: `1209.0482 [physics.ins-det]`.

[152] S. Acharya et al. "Centrality and transverse momentum dependence of inclusive J/ψ production at midrapidity in Pb–Pb collisions at $\sqrt{s_{\mathrm{NN}}} = 5.02$ TeV". In: (2019). arXiv: `1910.14404 [nucl-ex]`.

[153] W.-T. Deng, X.-N. Wang, and R. Xu. "Hadron production in p+p,p+Pb, and Pb+Pb collisions with the hijing 2.0 model at energies available at the CERN Large Hadron Collider". In: *Physical Review C* 83.1 (2011). ISSN: 1089-490X. DOI: `10.1103/physrevc.83.014915`. URL: `http://dx.doi.org/10.1103/PhysRevC.83.014915`.

[154] T. Sjöstrand, S. Mrenna, and P. Skands. "PYTHIA 6.4 physics and manual". In: *Journal of High Energy Physics* 2006.05 (2006), pp. 026–026. ISSN: 1029-8479. DOI: `10.1088/1126-6708/2006/05/026`. URL: `http://dx.doi.org/10.1088/1126-6708/2006/05/026`.

[155] F. Bossu et al. "Phenomenological interpolation of the inclusive J/psi cross section to proton-proton collisions at 2.76 TeV and 5.5 TeV". 2012. arXiv: `1103.2394 [nucl-ex]`.

[156] D. J. Lange. "The EvtGen particle decay simulation package". In: *Nuclear Instruments and Methods in Physics Research Section A: Accelerators, Spectrometers, Detectors and Associated Equipment* 462.1 (2001). BEAUTY2000, Proceedings of the 7th Int. Conf. on B-Physics at Hadron Machines, pp. 152–155. ISSN: 0168-9002. DOI: `https://doi.org/10.1016/S0168-9002(01)00089-4`. URL: `https://www.sciencedirect.com/science/article/pii/S0168900201000894`.

[157] E. Barberio and Z. Wąs. "PHOTOS - a universal Monte Carlo for QED radiative corrections: version 2.0". In: *Computer Physics Communications* 79.2 (1994), pp. 291–308. ISSN: 0010-4655. DOI: `https://doi.org/10.1016/0010-4655(94)90074-4`. URL: `https://www.sciencedirect.com/science/article/pii/0010465594900744`.

[158] R. Brun et al. "GEANT: Detector Description and Simulation Tool; Oct 1994". CERN Program Library. Long Writeup W5013. Geneva: CERN, 1993. DOI: `10.17181/CERN.MUHF.DMJ1`. URL: `https://cds.cern.ch/record/1082634`.

[159] D. Weiser. "Inclusive J/ψ production at mid-rapidity in pp and Pb–Pb collisions with ALICE, PhD. thesis". 2019. URL: `https://www.physi.uni-heidelberg.de/Publications/Dissertation_Dennis_Weiser.pdf`.

[160] S. Acharya et al. "Centrality and transverse momentum dependence of inclusive J/ψ production at midrapidity in Pb–Pb collisions at $\sqrt{s_{\mathrm{NN}}} = 5.02$ TeV". In: *Physics Letters B* 805 (2020), p. 135434. ISSN: 0370-2693. DOI: `10.1016/j.physletb.2020.135434`. URL: `http://dx.doi.org/10.1016/j.physletb.2020.135434`.

[161] J. Book. "J/ψ production in Pb–Pb collisions with ALICE at the LHC, PhD. thesis". 2014. URL: `http://publikationen.ub.uni-frankfurt.de/frontdoor/index/index/year/2015/docId/36595`.

[162] T. Bustamante. "Inclusive J/ψ production at midrapidity in Pb–Pb collisions at 5 TeV, PhD. thesis". 2018. URL: `http://cds.cern.ch/record/2634915`.

[163] S. Acharya et al. "Inclusive J/ψ production at midrapidity in pp collisions at $\sqrt{s} = 13$ TeV". In: (Aug. 2021). arXiv: `2108.01906 [nucl-ex]`.

[164] B. B. Abelev et al. "Measurement of quarkonium production at forward rapidity in pp collisions at $\sqrt{s} = 7$ TeV". In: *Eur. Phys. J. C* 74.8 (2014), p. 2974. DOI: 10.1140/epjc/s10052-014-2974-4. arXiv: 1403.3648 [nucl-ex].

[165] J. Adam et al. "Inclusive quarkonium production at forward rapidity in pp collisions at $\sqrt{s} = 8$ TeV". In: *Eur. Phys. J. C* 76.4 (2016), p. 184. DOI: 10.1140/epjc/s10052-016-3987-y. arXiv: 1509.08258 [hep-ex].

[166] S. Acharya et al. "Energy dependence of forward-rapidity J/ψ and ψ(2S) production in pp collisions at the LHC". In: *Eur. Phys. J. C* 77.6 (2017), p. 392. DOI: 10.1140/epjc/s10052-017-4940-4. arXiv: 1702.00557 [hep-ex].

[167] D. Acosta et al. "Measurement of the J/ψ meson and b-hadron production cross sections in p$\bar{\text{p}}$ collisions at $\sqrt{s} = 1960$ GeV". In: *Phys. Rev. D* 71 (2005), p. 032001. DOI: 10.1103/PhysRevD.71.032001. arXiv: hep-ex/0412071.

[168] R. Aaij et al. "Measurement of J/ψ production in pp collisions at $\sqrt{s} = 7$ TeV". In: *Eur. Phys. J. C* 71 (2011), p. 1645. DOI: 10.1140/epjc/s10052-011-1645-y. arXiv: 1103.0423 [hep-ex].

[169] R. Aaij et al. "Production of J/ψ and Υ mesons in pp collisions at $\sqrt{s} = 8$ TeV". In: *JHEP* 06 (2013), p. 064. DOI: 10.1007/JHEP06(2013)064. arXiv: 1304.6977 [hep-ex].

[170] R. Aaij et al. "Measurement of forward J/ψ production cross-sections in pp collisions at $\sqrt{s} = 13$ TeV". In: *JHEP* 10 (2015). [Erratum: JHEP 05, 063 (2017)], p. 172. DOI: 10.1007/JHEP10(2015)172. arXiv: 1509.00771 [hep-ex].

[171] G. Aad et al. "Measurement of the differential cross-sections of prompt and non-prompt production of J/ψ and ψ(2S) in pp collisions at $\sqrt{s} = 7$ and 8 TeV with the ATLAS detector". In: *Eur. Phys. J. C* 76.5 (2016), p. 283. DOI: 10.1140/epjc/s10052-016-4050-8. arXiv: 1512.03657 [hep-ex].

[172] V. Khachatryan et al. "Prompt and Non-Prompt J/ψ Production in pp Collisions at $\sqrt{s} = 7$ TeV". In: *Eur. Phys. J. C* 71 (2011), p. 1575. DOI: 10.1140/epjc/s10052-011-1575-8. arXiv: 1011.4193 [hep-ex].

[173] S. Acharya et al. "Studies of J/ψ production at forward rapidity in Pb–Pb collisions at $\sqrt{s_{\text{NN}}} = 5.02$ TeV". In: *JHEP* 02 (2020), p. 041. DOI: 10.1007/JHEP02(2020)041. arXiv: 1909.03158 [nucl-ex].

[174] B. Abelev et al. "Centrality, rapidity and transverse momentum dependence of J/ψ suppression in Pb–Pb collisions at $\sqrt{s_{\text{NN}}}$=2.76 TeV". In: *Phys. Lett. B* 734 (2014), pp. 314–327. DOI: 10.1016/j.physletb.2014.05.064. arXiv: 1311.0214 [nucl-ex].

[175] J. Adam et al. "Centrality dependence of the charged-particle multiplicity density at midrapidity in Pb–Pb collisions at $\sqrt{s_{\text{NN}}} = 5.02$ TeV". In: *Phys. Rev. Lett.* 116.22 (2016), p. 222302. DOI: 10.1103/PhysRevLett.116.222302. arXiv: 1512.06104 [nucl-ex].

[176] K. Aamodt et al. "Centrality dependence of the charged-particle multiplicity density at midrapidity in Pb–Pb collisions at $\sqrt{s_{\text{NN}}} = 2.76$ TeV". In: *Phys. Rev. Lett.* 106 (2011), p. 032301. DOI: 10.1103/PhysRevLett.106.032301. arXiv: 1012.1657 [nucl-ex].

[177] K. Adcox et al. "Centrality dependence of charged particle multiplicity in Au - Au collisions at S(NN)**(1/2) = 130-GeV". In: *Phys. Rev. Lett.* 86 (2001), pp. 3500–3505. DOI: 10.1103/PhysRevLett.86.3500. arXiv: nucl-ex/0012008.

[178] R. Aaij et al. "Study of prompt D^0 meson production in p–Pb collisions at $\sqrt{s_{\text{NN}}} = 5$ TeV". In: *JHEP* 10 (2017), p. 090. DOI: 10.1007/JHEP10(2017)090. arXiv: 1707.02750 [hep-ex].

[179] K. J. Eskola, H. Paukkunen, and C. A. Salgado. "EPS09: A New Generation of NLO and LO Nuclear Parton Distribution Functions". In: *JHEP* 04 (2009), p. 065. DOI: 10.1088/1126-6708/2009/04/065. arXiv: 0902.4154 [hep-ph].

[180] K. Kovarik et al. "nCTEQ15 - Global analysis of nuclear parton distributions with uncertainties in the CTEQ framework". In: *Phys. Rev. D* 93.8 (2016), p. 085037. DOI: 10.1103/PhysRevD.93.085037. arXiv: 1509.00792 [hep-ph].

[181] A. Kusina et al. "Gluon Shadowing in Heavy-Flavor Production at the LHC". In: *Phys. Rev. Lett.* 121.5 (2018), p. 052004. DOI: `10.1103/PhysRevLett.121.052004`. arXiv: `1712.07024` `[hep-ph]`.

[182] K. J. Eskola, H. Paukkunen, and C. A. Salgado. "An Improved global analysis of nuclear parton distribution functions including RHIC data". In: *JHEP* 07 (2008), p. 102. DOI: `10.1088/1126-6708/2008/07/102`. arXiv: `0802.0139` `[hep-ph]`.

[183] S. Acharya et al. "Charm-quark fragmentation fractions and production cross section at midrapidity in pp collisions at the LHC". In: (May 2021). arXiv: `2105.06335` `[nucl-ex]`.

[184] A. Andronic et al. "The multiple-charm hierarchy in the statistical hadronization model". In: *JHEP* 07 (2021), p. 035. DOI: `10.1007/JHEP07(2021)035`. arXiv: `2104.12754` `[hep-ph]`.

[185] M. Cacciari et al. "Theoretical predictions for charm and bottom production at the LHC". In: *JHEP* 10 (2012), p. 137. DOI: `10.1007/JHEP10(2012)137`. arXiv: `1205.6344` `[hep-ph]`.

[186] B. Abelev et al. "Upgrade of the ALICE Experiment: Letter Of Intent". In: *J. Phys. G* 41 (2014), p. 087001. DOI: `10.1088/0954-3899/41/8/087001`.

[187] "ALICE upgrade physics performance studies for 2018 Report on HL/HE-LHC physics". In: (2019). URL: `https://cds.cern.ch/record/2661798`.

Acknowledgements